学位論文

Stepwise Construction of Metal Complex Wires on Hydrogen-Terminated Silicon Surface and Their Electrochemical Evaluations

（水素終端化シリコン表面における金属錯体ワイヤの

逐次的構築と電気化学的評価）

平成 26 年 12 月　博士（理学）申請

東京大学大学院理学系研究科

化学専攻

前田　啓明

Abstract

This thesis describes the sequential construction of bis(terpyridine)iron (Fe(tpy)$_2$) complex wires on hydrogen-terminated silicon electrodes and the evaluation of their electrochemical properties.

In Chapter 1, general introductions about molecular devices, fabrication methods for nano-size structures, typical combinations of substrate and molecule for self-assembled monolayer formation, and multilayer formation using coordination reaction are described. In addition, the description of the electrochemical properties for bis(terpyridine)metal complex systems which have been investigated in our laboratory is included.

In Chapter 2, the stepwise construction of Fe(tpy)$_2$ complexes on hydrogen-terminated silicon electrodes via the four types of anchor ligands, the quantitative evaluation of their electron transfer rate constant (k_{ET}) values between silicon electrodes and the formed complexes are described. The results of cyclic voltammetry, X-ray photoelectron spectroscopy, and atomic force microscope confirm the fabrication of bis(terpyridine)iron complex. The k_{ET} values estimated from chronoamperograms reveal that the anchor ligands including phenylene unit give the greater k_{ET} values in spite of their longer distances. This phenomenon is elucidated by the molecular orbitals and energy levels estimated by the DFT calculation.

In Chapter 3, a hydrogen-terminated silicon surface is modified by Pd-catalyzed reaction developed in our laboratory, and the anchor ligand is immobilized via the covalent silicon-arene bond. The Fe(tpy)$_2$ complex is formed by the stepwise complexation, and the k_{ET} value is estimated by chronoamperometry. The result exhibits that the direct silicon-arene junction gives the superior charge transport than that of silicon-vinylene junction formed by the hydrosilylation reaction.

In Chapter 4, the stepwise construction of Fe(tpy)$_2$ multilayer wires terminated by ferrocene moiety or triarylamine moiety, their redox behavior and the elucidation of electron transport mechanism are described. The increase of estimated coverage of Fe(tpy)$_2$ with the number of coordination cycles confirms the stepwise elongation of Fe(tpy)$_2$ wires. The cyclic voltammetry measurements for terminal redox units show the slow electron transport between the ferrocene unit and the electrode while the superior electron transport is observed for triarylamine moiety. From the energy level relationship among silicon band structure, Fe(tpy)$_2$ unit and terminal redox species, the different electron transfer behavior are elucidated.

In Chapter 5, concluding remarks of this thesis are described.

Table of Contents

Chapter 1

General introduction

1-1 Molecular electronic devices

In the past decades, the shrink of electronic device size has been progressed and its performance has been improved. For example, although the world fastest supercomputer in 1993, CM-5/1024, had the 131 GFLOPS theoretical calculation performance and recorded the 59.7 GFLOPS in LINPAC performance, the CPU for desktop computer released in 2011 from Intel, Core i7 3930K, has the 153.6 GFLOPS theoretical calculation performance. However, in order to achieve its high performance and low energy consumption, the increase of the transistor density and the shrink of the smallest circuit size have still been continued. It is expected that the smallest circuit size will reach several nano meter in a near future. This size is close to the limit of microfabrication, and the appearance of a new fabrication technique for nano-scaled electric systems is desired.

A molecular electronic device is one of the next generation electronic device candidates. In 1974, the molecule which is expected to work as a rectifier was propounded by Aviram and Ratner [1] (Figure 1-1-1). In 1980s, Carter made a proposal the basic idea of the molecular device design and fabrication [2]. Based on their proposal, various molecules which can work as a switch [3], a memory [4], and a rectifier [5] have been propounded, synthesized, and evaluated their conductive property and electric performance (Figure 1-1-2).

The important feature of molecular electronic devices is not only the shrink of device size but also the expression of the additional property derived from a component molecule. This feature will allow us to construct a multi-functional device in a small space.
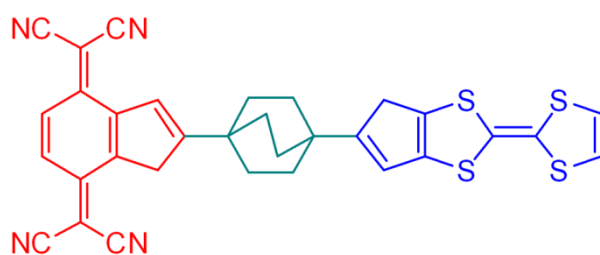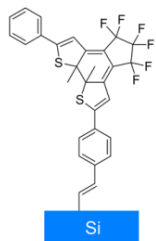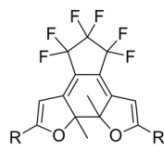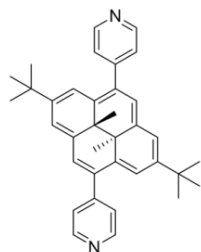

Figure 1-1-1. Molecule working as a rectifier propounded by Aviram and Ratner [1].
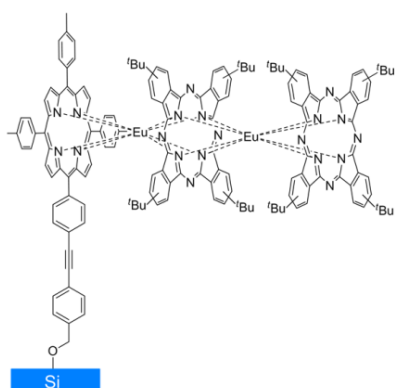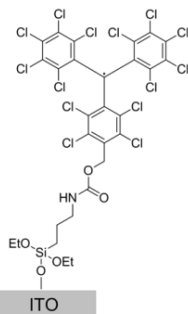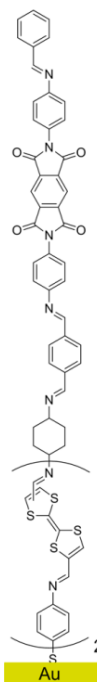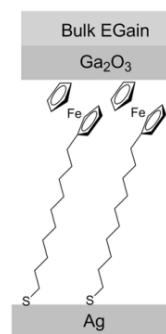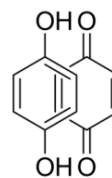
Figure 1-1-2. Molecules working as electric components [3a, 3c, 3d, 4a, 4d, 5a, 5c, 5d].

1-2 Top-down method and bottom-up method

In order to fabricate nano-size structures, a number of preparing methods have been developed. These methods are classified into top-down method and bottom-up method (Figure 1-2-1). In the top down method, a nano- or micro-scaled structure is produced by the etching or lithography processes. Photolithography is the most established method, and used in the present manufacturing process. However, the limitation of processable size is approaching because this method requires the photo irradiation for the patterning process, and a short wavelength light is needed in order to construct a small size pattern. Electron beam (EB) lithography is a powerful technique to make a nanometer scale pattern. However, it is not suitable for the volume production because of its long process time. In addition, these lithography techniques require special facilities such as an isolated clean room and vacuum chambers.

In the bottom-up method, a structure is constructed from tiny components such as atoms, molecules and nanoparticles. Self-assembly (or self-organization) is the typical strategy in the bottom-up method. In this method, a target structure is constructed automatically by the interactions among components and environments. And, assemble processes can progress not only in the vacuum state but also in solutions. It allows us to progress the preparation in simple equipment. Hence, it is suitable for the large-scale production. Although the self-assembly approach has not yet had established theories and techniques, a lot of researchers are putting great effort into the realization of structure construction with self-assembly. Scanning probe microscope (SPM) can operate both of the top-down process and the bottom-up process. For example, it can make a patterned structure by the scratching a soft material on a substrate with SPM probe [6]. This is included in the top-down approach. As the bottom-up process, we can manipulate the position of molecules or atoms on a substrate by STM tip [7]. However, the large-scale production is difficult with these methods because they require a long process time. Among these methods, self-assembly is a candidate of the next generation production technique for nano-scale structure construction.

Figure 1-2-1. Typical top-down and bottom-up methods for nano-scale structures.

1-3 Surface modification with self-assembled monolayer (SAM)
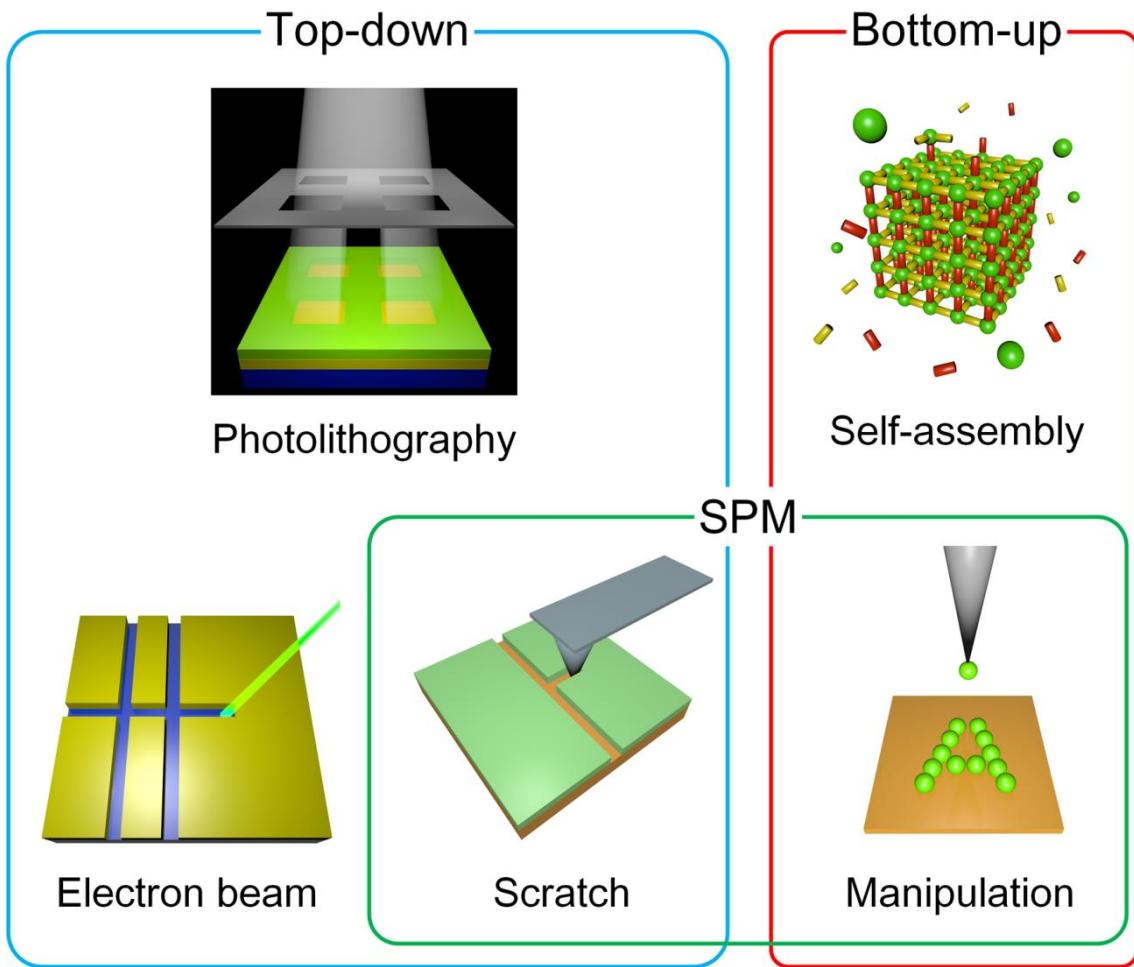
One of the approaches for the realization of molecular-based electronic devices is the electrode surface modification with functional molecules. In the past decades, the preparation of micro- and nano-scale patterned electrodes has been established. These kinds of electrodes can be used as a substrate of molecular devices. In addition, the molecules attached on the surface can communicate with electrode by the electron transfer. It means that the input and output signals can be transported rapidly. Because of above reasons, the surface modification is attractive to create molecular electronic systems.

Various surface modification methods have been developed and reported, such as Langmuir-Blodgett (LB) film [8], chemical vapor deposition (CVD) [9], spin coating [10], electropolymerization [11] and self-assembled monolayer (SAM). Among them, SAM is one of the most important methods for surface modification. It forms a uniform structure via a chemical bond between a molecule and an electrode by a simple process. These features are suitable for the large-scale production, the durability of devices, and the rapid signal transmission.

The typical preparation method of SAMs is composed of two processes. At first, a substrate surface is cleaned and activated. And then, it is immersed in a solution of molecules including the functional group which can react with substrate surface. The molecules are fixed on a surface via a chemical bond. The SAMs can be formed on various substrates such as metals (Au, Ag, and Pt), semiconductors (Si, Ge, GaAs, InP, and SiC), oxide compounds (indium tin oxide (ITO), TiO_2) and carbons (highly oriented pyrolytic graphite (HOPG), grassy carbon (GC), diamond and graphene) (Table 1-3-1). The fabricated SAMs are usually densely packed, and have the functions such as redox activity, photoluminescence, pH activity, photoisomerization, chemical reactivity, and hydrophobicity/hydrophilicity. Therefore, it is expected that SAM-modified substrates can work as molecular-based systems including field effect transistors (FETs), memories and sensors.

The SAMs on gold electrode are the most reported systems. Because gold has high conductivity and high chemical stability, it is suitable for the evaluation of redox behavior and conductivity of SAMs. The SAMs on an Au surface is commonly fabricated via Au-S bond. Therefore, thiols [12], disulufides [13], R-SAc (Ac: acetyl) [14], R-Thio (Thio: thiophenyl) [15] and R-SCN [16] can be used for the SAM formation. Additionally, an R-Py (Py: pyridinyl) [17] can be applied to the modification. These compounds can also form SAMs on noble metals such as Ag [20] and Pt [21]. In recent days, the SAM fabrication via Au-C bond [18, 19] has been attracted to produce a chemically stable and highly conductive system.

Indium tin oxide (ITO) is indium oxide doped a small amount of tin oxide. The important

properties of ITO are the electron conductivity and the high transparency of the visible light derived from the band gap of 3.7 eV. Therefore, ITO is used as a transparent electrode for a liquid crystal display, an organic light-emitting diode and a photovoltaic cell. In the field of SAM formation, ITO has often been chosen as an electrode for the research of a photocurrent generation or photoisomerization of SAMs. ITO can be modified with R-SiX$_3$ (X = OMe, OEt, Cl) [22], phosphoric acid [23], and carboxylic acid [24]. These regents can be used for modification of oxidized surface including TiO$_2$ [25] and SiO$_2$ [26].

Silicon is the most popular semiconductor in the electronics field due to the established industrial processes for the ultra-high-purity wafer production, the suitable band gap (1.12 eV) for the electric devices working at room temperature, and the controllable electric properties by the species and concentration of the doping agents. As the substrates of SAMs, the three types of silicon surface are often used. The first is oxidized silicon (SiO$_2$). The modification of SiO$_2$ is achieved by R-SiX$_3$ (X = OMe, OEt, Cl) reagents [26]. However, these SAMs include an insulating layer between silicon and molecules which will prevent electron transport between them. In order to connect silicon surface and molecules directly, the first modification method for the second type of surface, hydrogen-terminated silicon was reported by Linford and Chidsey [27]. Until the present day, the various modification methods for H-terminated silicon have been developed. Among them, the hydrosilyration reaction with alkenes and alkynes by thermal- or photo-activation attracts a great deal of attention because it forms the direct covalent Si-C bond between silicon and the confined molecules exclude the insulating layer [28]. This connection is stable due to its large binding energy, and it is expected that this junction is suitable for the electron transport evaluation. Other SAMs via Si-C bond was prepared by using organometallic compounds such as Grignard reagents and R-Li compounds [29]. These reagents are important to form SAMs which are difficult to be prepared by hydrosilylation reaction such as methyl or aryl groups directly bonded on silicon surface. Recently, our group developed the new surface modification method which allows us to fabricate the SAMs immobilized by the direct Si-aryl bond [30] in the presence of Pd catalyst and base. As other reagents which can form SAMs on hydrogen-terminated silicon, R-OH, R-CHO and R-SH are known [31]. These SAMs are confined via Si-O-C bond or Si-S-C bond. The last well-known surface is halogen-terminated silicon. These kinds of surface can be achieved by the exposure of H-terminated silicon to a halogen source such as PCl$_5$, Cl$_2$, Br$_2$ and NBS [32]. The surface is often used for the modification by organometallic reagents (Grignard reagent, and R-Li) [33], amines and alcohols [34].

The modification method of other semiconductors including Ge [35], GaAs [36], InP [37], and SiC [38] have been developed in recent years. Ge has the higher electron mobility than Si. This feature is useful to provide high-speed electric circuit systems. In addition, the band gap of Ge

is smaller than Si. Therefore, it is expected that the electric devices composed of Ge can run at the lower voltage and decrease energy consumption. The surface modification of Ge can be achieved by the similar reagents for Si modification. $R-SiX_3$ can modify oxidized surface, alkenes and thiols can modify hydrogen-terminated Ge surface, and Grignard reagents and thiols can be used for halide-terminated surface. On the other hand, SiC has the large band gap, and the high durability at severe operating environments. Recently, the SiC transistor which is available at 20,000 V was reported [39]. The HF etching of SiC gives an OH-terminated surface while an H-terminated surface is produced in the case of Si and Ge. The surface modification of these materials with alkenes and alkynes can be achieved. However, the structure of confined molecule on an OH-terminated SiC is different from that on H-terminated Si and Ge. In the case of alkenes, the reaction progresses according to Markovnikov's rule on SiC surface while an anti-Markovnikov structure is given on Si and Ge surface. Alkynes also show the similar trend, but a mixed structure is given on SiC (Figure 1-3-1).

Carbon is often used as an electrode because of its high chemical durability. In addition, a diamond electrode having the wide potential window and the small electric double layer current, and new carbon materials including graphene and carbon nanotube which are expected to exhibit novel phenomena have attracted a great deal of attentions. Thus, the development of the modification methods for carbon surface has been continued. As the typical techniques, hydrogen-terminated or halogen-terminated carbon surface can be modified by the compounds known as the regents for the SAM preparation on Si and Ge, such as alkenes, thiols and Grignard regents [40, 42]. Other regents, R-I and R-N=N-R are also utilizable [41]. As a particular case, the modification of the sp^2-conjugated carbon surface such as graphene and carbon nanotube can be achieved by π-conjugated carbon structure compounds (i.e. pyrene) [43] (Figure 1-3-2).

Diazonium salts are important compounds because they can form an organic film immobilized via a covalent bond on the various substrates[44]. The most popular method is the electrografting method, which fabricates a molecular film on a substrate by the reduction of diazonium compound on substrate surface. For this process, not only diazonium salts but also $Ar-NH_2$ compounds are available using the *in-situ* conversion to diazounium salt in the present of $NaNO_2$. Usually, the surface modified with diazonium salts has a multi-layered organic film because the polymerization via radical reaction occurs on the surface.

Table 1-3-1. Examples of molecule-substrate combinations for SAM formation

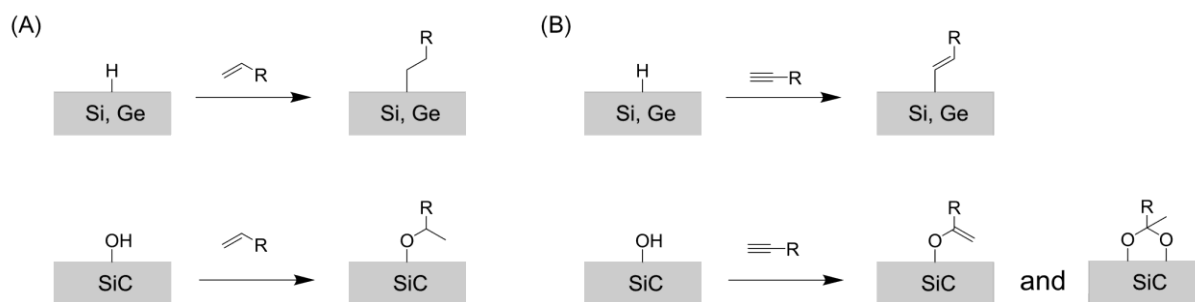| Substrate	Molecule	Ref.	Substrate	Molecule	Ref.
Au	R-SH	12	Halogen-Si	Grignard	33(a, b)
	R-S-S-R	13		R-Li	33(c, d)
	R-SAc	14		R-NH$_2$	34(a, b)
	R-Thio	15		R-OH	34(c)
	R-SCN	16	Oxidized Ge	R-SiX$_3$	35(a, b)
	R-Py	17	H-Ge	Alkenes	35(c, d)
	Alkynes	18		R-SH	35(e)
	NHC	19	Halogen-Ge	Grignard	35(f, g)
Ag	R-SH	20		R-SH	35(h, i)
Pt	R-SH	21(a)	GaAs	R-SH	36
	R-NC	21(b)	InP	R-SH	37
	R-Py	21(c)	SiC	Alkenes	38(a, b)
ITO	R-SiX$_3$	22		Alkynes	38(c)
	R-PO(OH)$_2$	23		R-Si(OMe)$_3$	38(d, e)
	R-CO$_2$H	24	H-C	Alkenes	40
TiO$_2$	Alkenes	25(a)		R-I	41(a)
	R-PO(OH)$_2$	25(b)		R-N=N-R	41(b)
	R-CO$_2$H	25(c)	Halogen-C	Alkenes	42(a)
Oxidized Si	R-SiX$_3$	26		Grignard	42(b)
H-Si	Alkenes	28		R-SH	42(c)
	Alkynes	28	X = Cl, OMe, or OEt		
	Grignard	29(a, b)	Ac = Acetate		
	R-Li	29(c, d)	NHC = *N*-heterocyclic carbene		
	R-I	30	Py = Pyridinyl group		
	R-OH	31(a, b)	Thio = Thiophenyl group		
	R-CHO	31(c, d)	Grignard = Grignard reagent, R-MgCl or R-MgBr		
	R-SH	31(e, f)			

Figure 1-3-1. Surface modification of H-terminated silicon and germanium and OH-terminated SiC with (A) alkenes and (B) alkenes [38a, c].
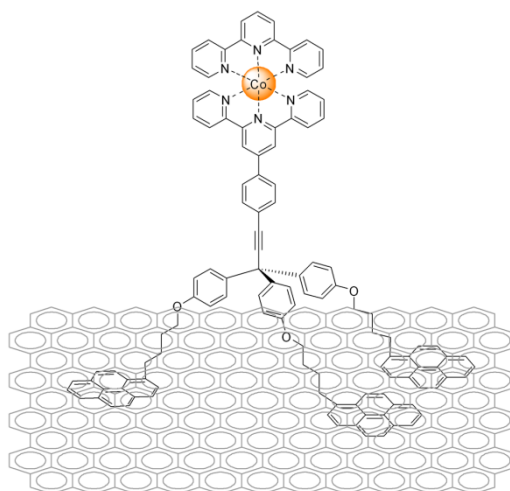

Figure 1-3-2. Modification of sp^2-conjugated carbon surface with a molecule including π-conjugated anchor [43b].

1-4 Multilayer construction

In order to construct a higher-level functionalized molecular system, a molecule which has multiple functions is required. However, synthesis of such kinds of molecules requires complicated processes and thus high cost. One of the resolutions is the multilayer fabrication on SAMs using molecules having a simple structure and function. We can introduce various functional molecular components in a molecular structure. Additionally, it is expected that molecules connected in series in a multilayer structure will exhibit multiple functions even if a molecular component only has one function.

For the realization of tailor-made molecular systems, the multilayer construction method which can produce the desired structure is required. The layer-by-layer method is one of the answers. In this method, a substrate modified by a SAM or a polymer are used as a foundation. The substrate is immersed in solutions containing component molecules sequentially until a desired structure is constructed. It allows us to control the number of the layers and array of components by the repeated or consecutive immersion process. The typical examples are click chemistry between an azide and a triple bond [45], the imine bond formation [46], electrostatic interaction [47], and also coordination reaction are often used (Figures 1-4-1, 1-5-1). The stepwise construction of multilayer structure using the coordination reaction is the attractive method because we can add the high-functionality to a structure by the electronic, magnetic and photophysical properties derived from the formed metal complex and introduction of functional ligands.
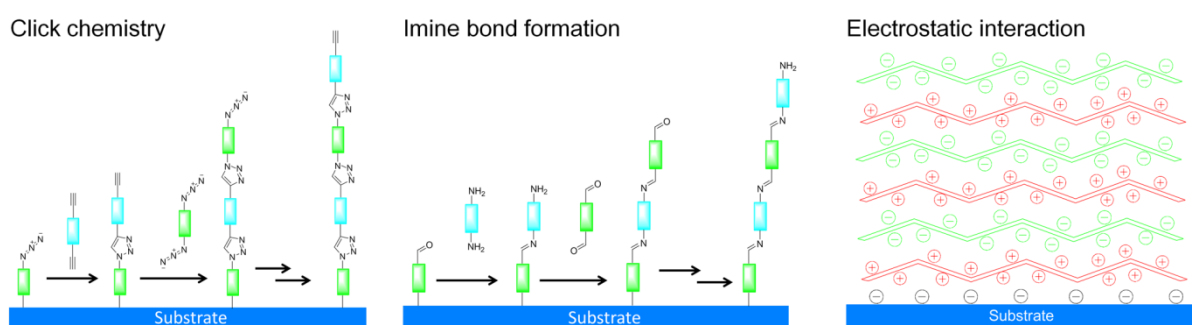

Figure 1-4-1. Layer-by-layer fabrication of multilayer on a substrate by the click chemistry, the imine bond formation and the electrostatic interaction.

1-5 Stepwise coordination method for multilayer construction

The stepwise fabrication of metal complex multilayer structure is achieved by the sequential immersion into solutions of a metal ion and a bridging ligand (Figure 1-5-1). Various combinations of metal ions and ligands can be used for the stepwise coordination method. For example, Zr(IV) or Ti(IV)/phosphoric acid, carboxylic acid and hydroxamic acid [48], M(II) or M(III)/2,2':6',2''-terpyridine (tpy) [49], Pd(II), Ag(I) or Cu(II)/pyridine [50] and other combinations [51] have been reported. Usually, metal salts are chosen as a component of metal complex multilayers; however, metal complexes and metal clusters can also participate in the layer-by-layer formation because they can also provide coordination sites. For instance, the researches which utilized trinuclear ruthenium cluster [52], binuclear complex [53], and ruthenium-coordinated phthalocyanine [54] have been reported. Most of researches have focused on the construction of multilayer systems. However, some of recent researches have evaluated the function and property of metal complex multilayers.

Lambert and McGimpsey's group evaluated the effect of metal ion on the photocurrent [55]. They prepared the pyrene-containing multilayer using Cu(II), Co(II), and Fe(III), and measured their photocurrent generation behavior in the coexistence of methylviologen for cathodic current and in the coexistence of triethanolamine for the anodic current. The largest cathodic photocurrent was observed in the Cu(II) complex system while the Fe(III) complex system exhibits the largest anodic photocurrent (Figure 1-5-2(A)).

The effect of the number of layers on the generated photocurrent has been evaluated by Dong and coworkers [49c, 52b, 54]. Usually, the photocurrent increases in accordance with the number of layers. However, the thicker layer shows the smaller photocurrent than that of thin layer due to the internal resistance of multilayer structure (Figure 1-5-2(B)).

Thompson and coworkers succeeded to improve the photocurrent by the construction of hetero porphyrin system [56]. They prepared three types of multilayer systems, POR_3/PV_3, ZOR_3/PV_3 and ZOR_2POR/PV_3, and evaluated their photocurrent generation ability in the presence of methyl viologen. Their quantum yields were estimated at 2.4 % for POR_3/PV_3, 2.3 % for ZOR_3/PV_3 and 3.5 % for ZOR_2POR/PV_3. The reason of higher quantum yield for the hetero porphyrin structure, ZOR_2POR/PV_3, was considered that the photo-induced charge separation was improved because the effective array of ZOR and POR having different redox potentials and the suitable optical energy gaps of wire components (Figure 1-5-2(C)).

Lin and Kagan connected the 60-80 nm gold electrode gap with the Rh cluster wire prepared by the layer-by-layer fashion, and measured its $I - V$ curve [57]. In the collected curve, the only first scan exhibits the negative differential resistance. The authors speculated that this phenomenon derived from the oxidation of Rh cluster units (Figure 1-5-3(A)).

The charge trapping behavior was reported in the hetero metal complex systems by van der Boom and his coworkers [58]. When they introduced an Os complex layer on the 8.0 nm Ru complex layer, the Os complex showed the sharp catalytic oxidation peak without the reduction wave while the Ru complex gave the reversible redox wave. On the other hand, the Ru complex layer on the thick Os complex layer exhibited the sharp reduction peak and the deformed oxidation wave derived from the Ru complex while the reversible redox couple of the Os complex was shown. These phenomena were expressed by the electron transport via the lower layer (Figure 1-5-3(B)).

As just described, we can find that the layer thickness and the array of metal complexes and ligands have the significant effect on the function and property.

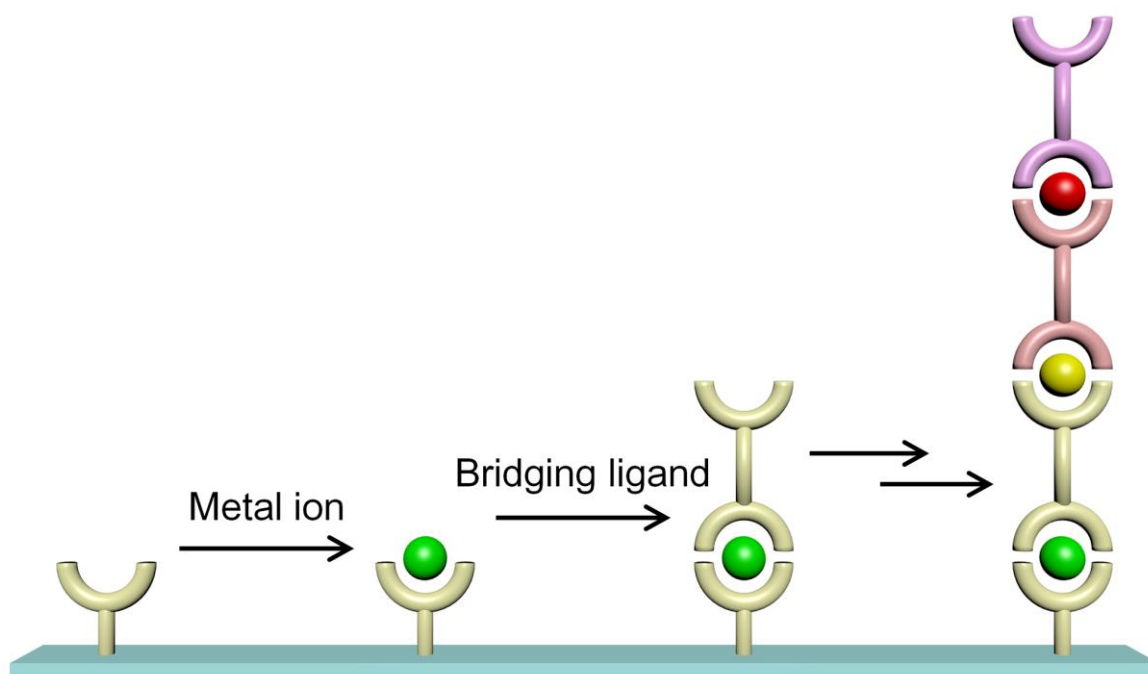**Figure 1-5-1.** Stepwise coordination process on a substrate.
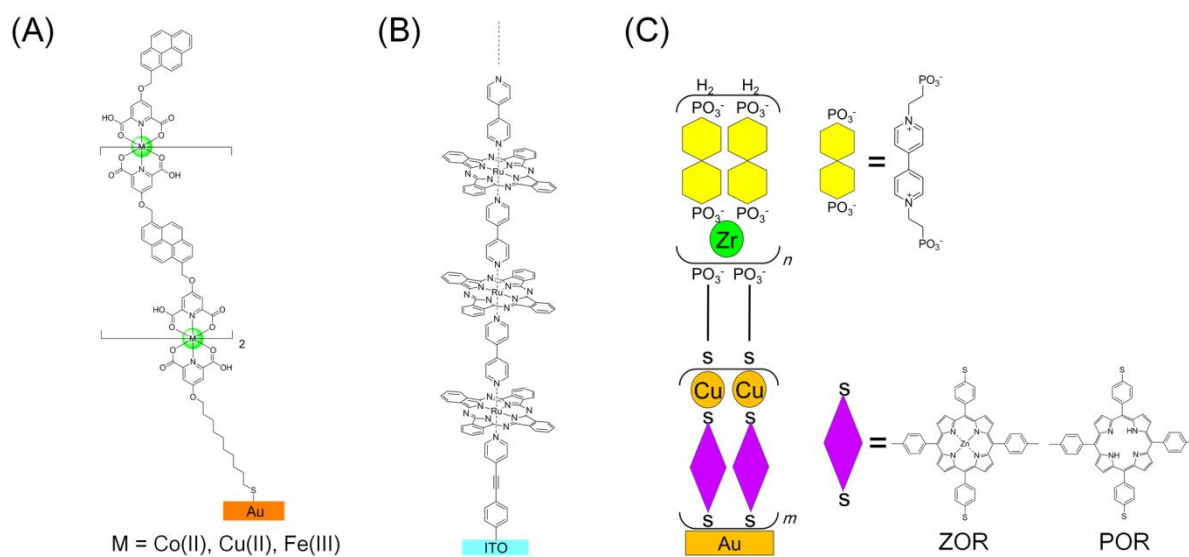
Figure 1-5-2. Examples of metal complex multilayer systems for photocurrent generation [55, 54b 56].
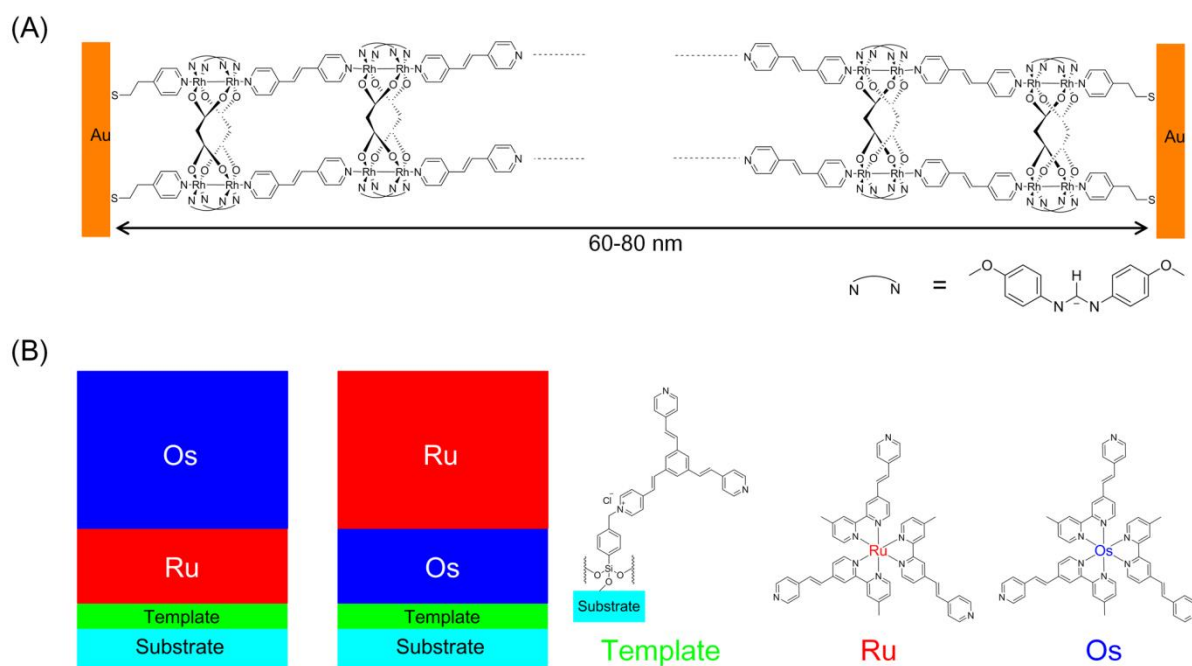

Figure 1-5-3. (A) Multilayer structure for $I – V$ curve measurement by Lin and Kagan [57], and (B) pattern diagrams of hetero metal complex multilayer systems for electrochemical measurement by van der Boom and coworkers [58].

1-6 Bis(terpyridine)metal complex wire

Our group has constructed bis(terpyridine)metal complex ($M(tpy)_2$) oligomer wires on gold [59], ITO [60] and silicon [61] electrodes, and evaluated their electrochemical properties and electron transport ability.

In the $M(tpy)_2$ wires on gold electrodes, we have focused on the electron transfer mechanism and their long-range electron transport ability. We can separate $M(tpy)_2$ wires to three components; anchor unit, bridging unit, and terminal unit. The effect of each component on the electron transport ability has been evaluated based on the equation 1.

$$k_{ET} = k_{ET}^0 \exp(-\beta^d d) \qquad (1)$$

Where, k_{ET} is the electron transfer rate constant, k_{ET}^0 is the k_{ET} at $d = 0$, β^d is the attenuation factor, and d is the distance between donor and accepter. In the case of our systems, d means the wire length from gold electrode to a terminal redox active species. Small β^d means the distance dependency of k_{ET} is weak. In other words, a molecular wire having small β^d can transport electrons effectively. The $M(tpy)_2$ wires evaluated in our laboratory have $\beta^d = 0.008 - 0.07$ $Å^{-1}$ for $Fe(tpy)_2$ and $\beta^d = 0.002 - 0.004$ $Å^{-1}$ for $Co(tpy)_2$ (Table 1-6-1). These values are smaller than the usual molecular wires such as alkyl chain, oligo(phenylene ethynylene) wire, oligophenyene, peptide chain and other molecular wires (Table 1-6-2). Therefore, $M(tpy)_2$ wire systems have the superior long-range electron transportability (Figure 1-6-1(A)). On the other hand, the anchor unit and the terminal unit play an important role in the k_{ET}^0 values while their effect on the β^d value is small.

The electron transfer mechanism in $M(tpy)_2$ wires was elucidated by the current decays in chronoamperograms and the numerical simulation of branched $Fe(tpy)_2$ wires. The sequential hopping mechanism, which the electron hops between the closest iron complex units, was assumed, and the theoretical current decay was predicted. The calculated decay curve consisted with the experimental current decay. Hence, the electron transport mechanism was considered as the sequential hopping (Figure 1-6-1(B)).

In the research of $M(tpy)_2$ wires on ITO electrodes, the effect of metal ions on the photocurrent generation behavior was investigated. The $M(tpy)_2$ wires were prepared using Fe(II), Co(II) and Zn(II), and porphrin moiety was introduced at the termini of the wires. Their photocurrent measurement was performed in a Na_2SO_4 aqueous solution in the presence of triethanolamine, and the $Co(tpy)_2$ wire exhibited the largest quantum efficiency because the $Co^{2+/+}$ level between the ground state and S_1 state of porphyrin worked as the effective photo-electron transfer pathway (Figure 1-6-2).

In my master course, I constructed Fe(tpy)$_2$ wires on hydrogen-terminated silicon(111) electrodes and investigated their electrochemical behaviors. On the highly-doped n-type silicon surface, Fe(tpy)$_2$ wires exhibited the reversible redox couple in the dark and under illuminated condition. When the wires were prepared on the moderately-doped n-type silicon, they showed the irreversible redox wave in the dark while the reversible redox wave accompanying the negative redox potential shift appeared under Xe-lamp irradiation. This photoresponsive redox behavior has not been observed in the M(tpy)$_2$ wire systems on gold electrode. Therefore, it is considered that the band structure of silicon contributes to this characteristic electrochemical phenomenon (Figure 1-6-3).

Table 1-6-1. Attenuation factor (β^d) values of M(tpy)$_2$ complex wires [59e]
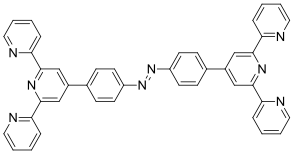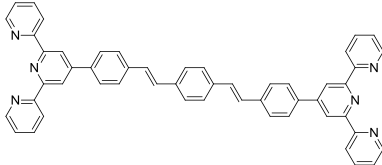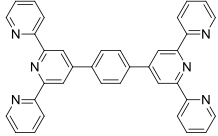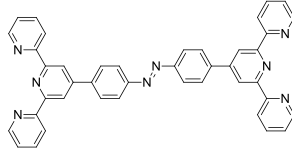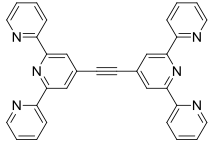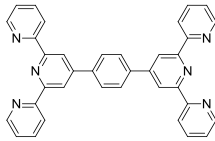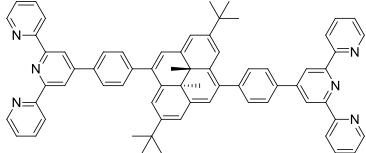
M	Bridging ligand	β^d / Å^{-1}	M	Bridging ligand	β^d / Å^{-1}
Fe		0.012	Fe		0.031
Fe		0.015	Co		0.002
Fe		0.07	Co		0.004
Fe		0.008			

Table 1-6-2. Examples of attenuation factor (β^d) values for molecular wires [62]

Molecular wire	β^d / Å^{-1}	Molecular wire	β^d / Å^{-1}
Alkyl chain	≈ 1	Oligo(phenylene ethynylene)	0.2 – 0.34
DNA	0.2 – 1.8	π-stacked benzene	0.63
Peptide chain	0.32 – 0.46	Viologen wire	0.006
Oligophenylene	0.2 – 0.77	Porphyrin wire	0.034
Acenes	0.2 – 0.5	Oligosilane	0.27
Olefin	≥ 0.2	Ru complex	0.012 – 0.021
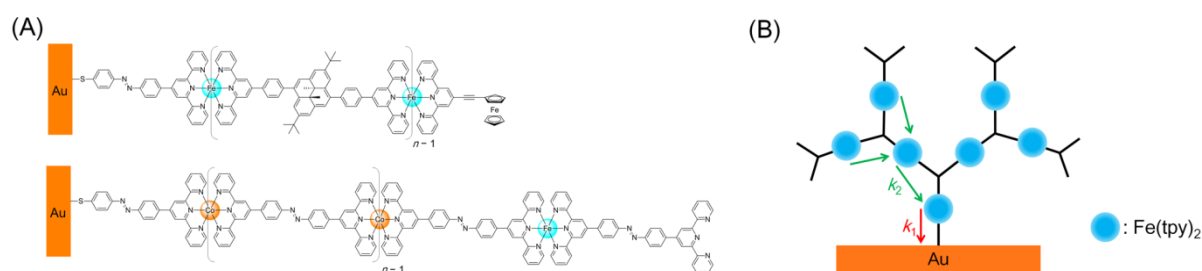
Figure 1-6-1. (A) Bis(terpyridine)metal complex wires which have the smallest β^d value on gold electrode, Fe(tpy)$_2$: 0.008 Å^{-1}, Co(tpy)$_2$: 0.002 Å^{-1} [59e], (B) pattern diagram of branched Fe(tpy)$_2$ wire on gold electrode and its electron transfer model [59c].
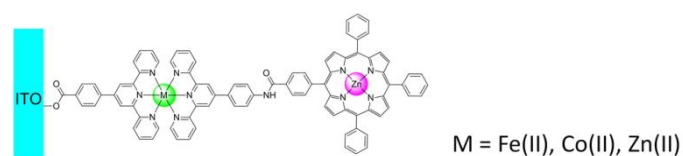
Figure 1-6-2. Porphyrin-terminated M(tpy)$_2$ wire on ITO electrode [60].
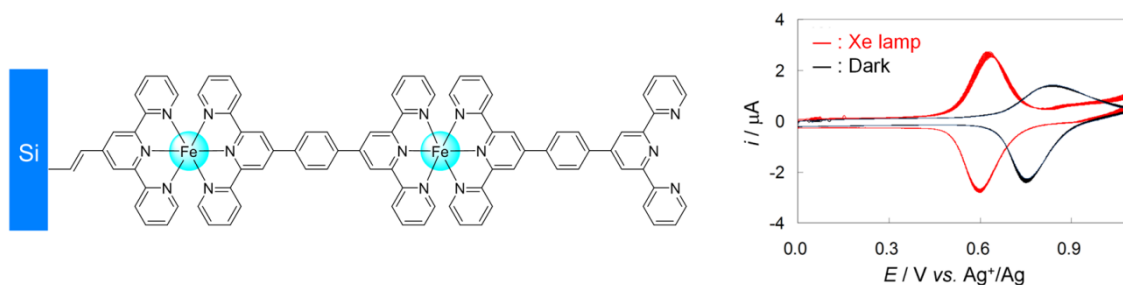
Figure 1-6-3. Structure of Fe(tpy)$_2$ wire on hydrogen-terminated silicon electrode and its photoresponsive electrochemical behavior, cyclic voltammograms measured under Xe light irradiation (red solid line) and in the dark (black solid line). Adapted from Ref. 61 with permission from The Royal Society of Chemistry.

1-7 Aim of the thesis

The realization of molecular electric devices has been attracted as one of the candidate methods for the next generation nano-scale electric device construction. Among of the various fabrication methods, the SAM formation and multilayer construction on electrode classed in the bottom-up method are significant because it allows us to produce higher-level functionalized molecular systems and manipulate their property by the control of molecular array and the introduction of functional molecules.

Gold has been often chosen as a substrate for SAM formation because its high conductivity and chemical stability is suitable for the electric and electrochemical evaluation of SAMs. However, most of present electric devices are composed of semiconductors. Among them, silicon is the most popular material due to the suitable band gap for the electric devices working at room temperature, the controllable electric property of silicon by the dopant density and species, the large amount of reserve, and the established purification procedure for silicon ingot production. Therefore, the electrochemical evaluation of SAMs and multilayers on silicon substrate is important to realize molecular electronic systems.

Therefore, I employed silicon as an electrode for SAM formation and performed the construction of $Fe(tpy)_2$ wire and their electrochemical measurement in order to unveil their electrochemical phenomena on a semiconductor. According to my previous research, the $Fe(tpy)_2$ wires constructed on hydrogen-terminated silicon exhibit the different electrochemical behavior including the photoresponsive redox reaction and the dependency on the dopant density which have not been observed in the $M(tpy)_2$ systems on gold electrode. Hence, silicon, especially its band gap, will affect the electrochemical properties including the redox behavior and electron transport phenomenon. In this thesis, the electron transfer rate constant between $Fe(tpy)_2$ complex and silicon was evaluated quantitatively, and the effect of anchor ligands was investigated. In addition, the investigation of the electron transport behavior for $Fe(tpy)_2$ multilayer wires and the elucidation of their electron transport mechanisms were performed.

1-8 References

1. Aviram A.; Ratner, M. A. *Chem. Phys. Lett.* **1974**, *29*, 277-283.

2. a) Carter, F. L. *Physica D* **1984**, *10*, 175-194. b) Carter, F. L. *Microelectron. Eng.* **1985**, *2*, 11-24. c) Carter, F. L. *Superlattice. Microst.* **1986**, *2*, 113-128.

3. a) Roldan, D.; Kaliginedi, V.; Cobo, S.; Kolivoska, V.; Bucher, C.; Hong, W.; Royal G.; Wandlowski, T. *J. Am. Chem. Soc.* **2013**, *135*, 5974-5977. b) Staykov, A.; Watanabe, M.; Ishihara, T.; Yoshizawa, K. *J. Phys. Chem. C* **2014**, *118*, 27539-27548. c) Kim, Y.; Hellmuth, T. J.; Sysoiev, D.; Pauly, F.; Pietsch T.; Wolf, J.; Erbe, A.; Huhn, T.; Groth, U.; Steiner, U. E.; Scheer, E. *Nano Lett.* **2012**, *12*, 3736-3742. d) Uchida, K.; Yamanoi, Y.; Yonezawa, T.; Nishihara, H. *J. Am. Chem. Soc.* **2011**, *133*, 9239-9241.

4. a) Simão C.; Mas-Torrent, M.; Crivillers, N.; Lloveras, V.; Artés J. M.; Gorostiza, P.; Veciana, J.; Rovira C. *Nat. Chem.* **2011**, *3*, 359-364. b) Green, J. E.; Choi, J. W.; Boukai, A.; Bunimovich, Y.; Johnston-Halperin, E.; DeIonno, E.; Luo, Y.; Sheriff, B. A.; Xu, K.; Shin, Y. S.; Tseng, H.-R.; Stoddart, J. F.; Heath, J. R. *Nature*, **2007**, *445*, 414-417. c) Jurow, M.; Schuckman, A. E.; Batteas, J. D.; Drain, C. M. *Coord. Chem. Rev.* **2010**, *254*, 2297-2310. d) Liu, Z.; Yasseri, A. A.; Lindsey, J. S.; Bocian, D. F. *Science* **2003**, *302*, 1543-1545.

5. a) Majumder, C.; Mizuseki, H.; Kawazoe, Y. *J. Phys. Chem. A* **2001**, *105*, 9454-9459. b) Tsuji, Y.; Staykov, A.; Yoshizawa, K. *J. Phys. Chem. C* **2012**, *116*, 2575-2580. c) Nijhuis, C. A.; Reus, W. F.; Siegel, A. C.; Whitesides, G. M. *J. Am. Chem. Soc.* **2011**, *133*, 15397-15411. d) Luo, L.; Balhorn, L.; Vlaisavljevich, B.; Ma, D.; Gagliardi, L. Frisbie, C. D. *J. Phys. Chem. C* **2014**, *118*, 26485-26497.

6. a) Shi, J.; Chen, J.; Cremer, P. S. *J. Am. Chem. Soc.* **2008**, *130*, 2718-2719. b) Drexler, C. I.; Moore, III, K. B.; Causey, C. P.; Mullen, T. J. *Langmuir* **2014**, *30*, 7447-7455. c) Kaholek, M.; Lee, W.-K.; LaMattina, B.; Caster, K. C.; Zauscher, S. *Nano Lett.* **2004**, *4*, 373-376.

7. a) Eigler, D. M.; Schweizer, E. K. *Nature* **1990**, *344*, 524-526. b) Swart, I.; Sonnleitner, T.; Niedenführ, J.; Repp, J. *Nano Lett.* **2012**, *12*, 1070-1074. c) Hla, S. W. *Rep. Prog. Phys.* **2014**, *77*, 056502.

8. a) Blodgett, K. B. *J. Am Chem. Soc.* **1935**, *57*, 1007-1022. b) Peterson, I. R. *J. Phys. D Appl. Phys.* **1990**, *23*,379-395.

9. Xu, M.; Liang, T.; Shi, M.; Chen, H. *Chem. Rev.* **2013**, *113*, 3766-3798.

10. a) Ramuz, M. P.; Vosgueritchian M.; Wei, P.; Wang, C.; Gao, Y.; Wu, Y.; Chen, Y.; Bao, Z. *ACS Nano* **2012**, *6*, 10384-10395. b) Weiss, E. A.; Porter, V. J.; Chiechi, R. C.; Geyer, S. M.; Bell, D. C.; Bawendi, M. G.; Whitesides, G. M. *J. Am. Chem. Soc.* **2008**, *130*, 83-92.

11. a) Nie, H.-J.; Shao, J. Y.; Wu, J.; Yao, J.; Zhong, Y. W. *Organometallics*, **2012**, *31*, 6952-6959. b) Nalin de Silva, K. M.; Hwang, E.; Serem, W. K.; Fronczek, F. R.; Garno, J. C.; Nesterov, E. E.; *ACS Appl. Mater. Interfaces* **2012**, *4*, 5430-5441. c) Wu, K.-H.; Maeda, H.; Kambe, T.; Hoshiko, K.; Phua, E. J. H.; Sakamoto, R.; Nishihara, H. *Dalton Trans.* **2013**, *42*, 15877-15880.

12. a) Kitagawa, T.; Matsubra, H.; Komatsu, K.; Hirai, K.; Okazaki, T.; Hase, T. *Langmuir* **2013**, *29*, 4275-4282. b) Singhana, B.; Rittikulsittichai, S.; Lee, T. R. *Langmuir* **2013**, *29*, 561-569. c) Matei, D. G.; Muzik, H.; Gölzhäuser, A.; Turchanin, A. *Langmuir* **2012**, *28*, 13905-13911. d) Breuer, R.; Schmittel, M. *Organometallics* **2012**, *31*, 6642-6651. e) Tian, H.; Xiang, D.; Shao, H.; Yu, H.-Z. *J. Phys. Chem. C* **2014**, *118*, 13733-13742.

13. a) Sahli, R.; Fave, C.; Raouafi, N.; Boujlel, K.; Schöllhorn, B.; Limoges, B. *Langmuir* **2013**, *29*, 5360-5368. b) Cormode, D. P.; Evans, A. J.; Davbis, J. J.; Beer, P. D. *Dalton Trans* **2010**, *39*, 6532-6541. c) Yamamoto, K.; Sugiura, H.; Amemiya, R.; Aikawa, H.; An, Z.; Yamaguchi, M.; Mizukami, M.; Kurihara, K. *Tetrahedron* **2011**, *67*, 5972-5978.

14. a) Chen, K.-Y.; Ivashenko, O.; Carroll, G. T.; Robertus, J.; Kistemaker, J. C. M.; London, G.; Browne, W. R.; Rudolf, P.; Feringa, B. L. *J. Am. Chem. Soc.* **2014**, *136*, 3219-3224. b) Vlkenier, H.; Huisman, E.H.; van Hal, P. A.; de Leeuw, D. M.; Chiechi, R. C.; Hummelen, J. C. *J. Am. Chem. Soc.* **2011**, *133*, 4930-4939.

15. a) Cho, H.-h.; Chang, H.-Y.; Kim, E.-H.; Park, Y. C.; Bae, Z.-U. *Bull. Korean Chem. Soc.* **2006**, *27*, 1701-1704. b) Halpin, Y.; Longtenberg, H.; Cleary, L.; Schenk, S.; Schulz, M.; Draksharapu, A.; Browne, W. R.; Vos, J. G. *Eur. J. Inorg. Chem.* **2013**, *2013*, 4291-4299.

16. Shen, C.; Buck, M.; Wilton-Ely, J. D. E. T.; Weidner, T.; Zharnikov, M. *Langmuir* **2008**, *24*, 6609-6615.

17. Zhou, X.-S.; Liu, L.; Fortgang, P.; Lefevre, A.-S. Serra-Muns, A.; Raouafi, N.; Amatore, C.; Mao, B.-W.; Maisonhaute, E.; Schöllhorn, B. *J. Am. Chem. Soc.* **2011**, *133*, 7509-7516.

18. Zaba, T.; Noworolska, A.; Bowers, C. M.; Breiten, B.; Whitesides, G. M.; Cyganik, P. *J. Am. Chem. Soc.* **2014**, *136*, 11918-11921.

19. Crudden, C. M.; Horton, J. H.; Ebralidze, I. I.; Zenkina, O. V.; McLean, A. B.; Drevniok, B.; She, Z.; Kraatz, H.-B.; Mosey, N. J.; Seki, T.; Keske, E. C.; Leake, J. D.; Rousina-Webb, A.; Wu, G. *Nat. Chem.* **2014**, *6*, 409-414.

20. a) Nijhuis, C. A.; Reus, W. F.; Whitesides, G. M. *J. Am. Chem. Soc.* **2009**, *131*, 17814-17827. b) Ma, C.; Harris, J. M. *Langmuir* **2012**, *28*, 2628-2636.

21. a) Petrovykh, D.Y.; Kimura-Suda, H.; Opdahl, A.; Richter, L.J.; Tarlov, M.J.; Whitman, L. J. *Langmuir* **2006**, *22*, 2578-2587. b) Bong, D.; Tam, I.; Breslow, R. *J. Am. Chem. Soc.* **2004**, *126*, 11796-11797. c) Mallon, C. T.; Forster, R. J.; McNally, A.; Campagnoli, E.;

Pikramenou, Z.; Keyes, T. E. *Langmuir* **2007**, *23*, 6997-7002.

22. a) Cho, Y.-J.; Ahn, T. K.; Song, H.; Kim, K. S.; Lee, C. Y.; Seo, W. S.; Lee, K.; Kim, S. K.; Kim, D.; Park, J. T. *J. Am. Chem. Soc.* **2005**, *127*, 2380-2381. b) Yamada, H.; Imahori, H.; Nishimura, Y.; Yamazaki, I.; Ahn, T. K.; Kim, S. K.; Kim, D.; Fukuzumi, S. *J. Am. Chem. Soc.* **2003**, *125*, 9129-9139.

23. a) Koh, S. E.; McDonald, K. D.; Holt, D. H.; Dulcey, C. S. Chaney, J. A.; Pehrsson, P. E. *Langmuir* **2006**, *22*, 6249-6255. b) Wang, H.; Gomez, E. D.; Guan, Z.; Jaye, C.; Toney, M. F.; Fischer, D. A.; Kahn, A.; Loo, Y.-L. *J. Phys. Chem. C* **2013**, *117*, 20474-20484.

24. a) Matsuo, Y.; Ichiki, T.; Nakamura, E. *J. Am. Chem. Soc.* **2011**, *133*, 9932-9937. b) Matsuo, Y.; Ichiki, T.; Radhakrishnan, S. G.; Guldi, D. M.; Nakamura, E. *J. Am. Chem. Soc.* **2010**, *132*, 6342-6348. c) Holman, M. W.; Liu, R.; Adams, D. M. *J. Am. Chem. Soc.* **2003**, *125*, 12649-12654.

25. a) Franking, R.; Hamers, R. J. *J. Phys. Chem. C* **2011**, *115*, 17102-17110. b) Wang, L.; Ashford, D. L.; Thompson, D. W.; Meyer, T. J.; Papanikolas, J. M. *J. Phys. Chem. C* **2013**, *117*, 24250-24258. c) Paoprasert, P.; Laaser, J. E.; Xiong, W.; Franking, R. A.; Hamers, R. J.; Zanni, M. T.; Schmidt, J. R.; Gopalan, P. *J. Phys. Chem. C* **2010**, *114*, 9898-9907.

26. a) Sugimura, H.; Hozumi, A.; Kameyama, T.; Takai, O. *Surf. Interface Anal.* **2002**, *34*, 550-554. b) Wu, K.; Bailey, T. C.; Willson, C. G.; Ekerdt, J. G. *Langmuir* **2005**, *21*, 11795-11801. c) Ardès-Guisot, N.; Durand, J.-O.; Granier, M.; Perzyna, A.; Coffinier, Y.; Grandidier, B.; Wallart, X.; Stievenard, D. *Langmuir* **2005**, *21*, 9406-9408. d) Park, J.; Jo, S. B.; Yu, Y.-J.; Kim, Y.; Yang, J. W.; Lee, W. H.; Kim, H. H.; Hong, B. H.; Kim, P.; Cho, K.; Kim, K. S. *Adv. Mater.* **2012**, *24*, 407-411.

27. Linford, M. R.; Chidsey, C. E. D. *J. Am. Chem. Soc.* **1993**, *115*, 12631-12632.

28. a) Buriak, J. M. *Chem. Commun.* **1999**, 1051-1060. b) Ciampi, S. Harper, J. B.; Gooding J. J. *Chem. Soc. Rev.* **2010**, *39*, 2158-2183.

29. a) Herrera, M. U.; Ichii, T.; Murase, K.; Sugimura, H. *Chem. Lett.* **2012**, *41*, 902-904. b) Yamada, T.; Shirasaka, K.; Noto, M.; Kato, H. M.; Kawai, M. *J. Phys. Chem. B* **2006**, *110*, 7375-7366. c) Song, J. H.; Sailor, M. J. *Inorg. Chem.* **1999**, *38*, 1498-1503. d) Song, J. H.; Sailor, M. J. *J. Am. Chem. Soc.* **1998**, *120*, 2376-2381.

30. Yamanoi, Y.; Sendo, J.; Kobayashi, T.; Maeda, H.; Yabusaki, Y.; Miyachi, M.; Sakamoto, R.; Nishihara, H. *J. Am. Chem. Soc.* **2012**, *134*, 20433-20439.

31. a)Bala, S.; Aithal, R. K.; Derosa, P.; Janes, D.; Kuila, D. *J. Phys. Chem. C* **2010**, *114*, 20877-20884. b) Sano, H.; Maeda, H.; Ichii, T.; Murase, K.; Noda, K.; Matsushige, K.; Sugimura, H. *Langmuir* **2009**, *25*, 5516-5525. c) Effenberger, F.; Götz, G.; Bidlingmaier, B.; Wezstein, M. *Angew. Chem. Int. Ed.* **1998**, *37*, 2462-2464. d) Tajimi, N.; Sano, H.; Murase, K.; Lee, K.-H.; Sugimura, H. *Langmuir* **2007**, *23*, 3193-3198. e) Lou, J. L.; Shiu,

H. W.; Chang, L. Y.; Wu, C. P.; Soo, Y.-L.; Chen, C.-H. *Langmuir*, **2011**, *27*, 3436-3441. f) Sano, H.; Ohno, K.; Ichii, T. Murase, K.; Sugimura, H. *Jpn. J. Appl. Phys.* **2010**, *49* 01AE09.

32. a) Wong, K. T.; Lewis, N. S. *Acc. Chem. Res.* **2014**, *47*, 3037-3044. b) Eves, B. J.; Lopinski, G. P. *Surf. Sci.* **2005**, *579*, 89-96. c) Xu, F. J.; Cai, Q. J.; Kang, E. T.; Neoh, K. G. *Langmuir* **2005**, *21*, 3221-3225.

33. a) Lattimer, J. R. C.; Brunschwig, B. S.; Lewis, N. S.; Gray, H. B. *J. Phys. Chem. C* **2013**, *117*, 27012-27022. b) Knapp, D.; Brunschwig, B. S.; Lewis, N. S. *J. Phys. Chem. C* **2010**, *114*, 12300-12307. c) Li, F.; Basile, V. M.; Pekarek, R. T.; Rose, M. J. *ACS Appl. Mater. Interfaces* **2014**, *6*, 20557-20568. d) O'Leary, L. E.; Rose, M. J.; Ding, T. X.; Johansson, E.; Brunschwig, B. S. Lewis, N. S. *J. Am. Chem. Soc.* **2013**, *135*, 10081-10090.

34. a) Tian, F.; Teplyakov, A. V. *Langmuir* **2013**, *29*, 13-28. b) Qi, H.; Gupta, A.; Noll, B. C.; Snider, G. L.; Lu, Y.; Lent, C.; Fehlner, T. P. *J. Am. Chem. Soc.* **2005**, *127*, 15218-15227. c) Zhu, X.-Y.; Boiadjiev, V.; Mulder, J. A.; Hsung, R. P.; Major, R. C. *Langmuir* **2000**, *16*, 6766-6772.

35. a) Zhang, S.; Koberstein, J. T. *Langmuir* **2012**, *28*, 486-493. b) Zhang, S.; Maidenberg, Y.; Luo, K.; Koberstein, J. T. *Langmuir* **2014**, *30*, 6071-6078. c) Xu, F. J.; Cai, Q. J.; Kang, E. T.; Neoh, K. G.; Zhu, C. X. *Organometallics* **2005**, *24*, 1768-1771. d) Holmberg, V. C.; Korgel, B. A. *Chem. Mater.* **2010**, *22*, 3698-3703. e) Han. S. M.; Ashurst, W. R.; Carraro, C.; Maboudian, R. *J. Am. Chem. Soc.* **2001**, *123*, 2422-2425. f) Morris, C. J.; Shestopalov, A. A.; Gold, B. H.; Clark, R. L.; Toone, E. J. *Langmuir* **2011**, *27*, 6486-6489. g) He, J.; Lu, Z.-H.; Mitchell, S. A.; Wayner, D. D. M. *J. Am. Chem. Soc.* **1998**, *120*, 2660-2661. h) Ardalan, P.; Musgrave, C. B.; Bent, S. F. *Langmuir* **2009**, *25*, 2013-2025. i) Ardalan, P.; Sun, Y.; Pianetta, P.; Musgrave, C. B.; Bent, S. F. *Langmuir* **2010**, *26*, 8419-8429.

36. a) McGuiness, C. L.; Diehl, G. A.; Blasini, D.; Smilgies, D.-M.; Zhu, M.; Samarth, N.; Weidner, T.; Ballav, N.; Zharnikov, M.; Allara, D. L. *ACS Nano* **2010**, *4*, 3447-3465. b) McGuiness, C. L.; Shaporenko, A.; Zharnikov, M.; Walker, A. V.; Allara, D. L. *J. Phys. Chem. C* **2007**, *111*, 4226-4234. c) Lu, H.; Kind, M.; Terfort, A.; Zharnikov, M. *J. Phys. Chem. C* **2013**, *117*, 26166-26178. d) Huang, X.; Liu, N.; Moumanis, K.; Dubowski, J. J. *J. Phys. Chem. C* **2013**, *117*, 15090-15097.

37. a) Yamamoto, H.; Butera, R. A.; Gu, Y.; Waldeck, D. H. *Langmuir* **1999**, *15*, 8640-8644. b) Alarcón, L. S.; Chen, L.; Esaulov, V. A.; Gayone, J. E.; Sánchez, E. A.; Grizzi, O. *J. Phys. Chem. C* **2010**, *114*, 19993-19999. c) Gu, Y.; Lin, Z.; Butera, R. A.; Smentkowski, V. S.; Waldeck, D. H. *Langmuir* **1995**, *11*, 1849-1851.

38. a) Rosso, M.; Arafat, A.; Schroën, K.; Giesbers, M.; Roper, C. S.; Maboudian, R.; Zuilhof, H. *Langmuir* **2008**, *24*, 4007-4012. b) Rosso, M.; Giesbers, M.; Arafat, A.; Schroën, K.;

Zuilhof, H. *Langmuir* **2009**, *25*, 2172-2180. c) Pujari, S. P.; Scheres, L.; Weidner, T.; Baio, J. E.; Stuart, M. A. C.; van Rijn, C. J. M.; Zuilhof, H. *Langmuir* **2013**, *29*, 4019-4031. d) Williams, E. H.; Davydov, A. V.; Motayed, A.; Sundaresan, S. G.; Bocchini, P.; Richter, L. J.; Stan, G.; Steffens, K.; Zangmeister, R.; Schreifels, J. A.; Rao, M. V. *Appl. Surf. Sci.* **2012**, *258*, 6056-6063. e) Schoell, S. J.; Hoeb, M.; Sharp, I. D.; Steins, W.; Eickhoff, M.; Stutzmann, M.; Brandt, M. S. *Appl. Phys. Lett.* **2008**, *92*, 153301.

39. Okuda, T.; Niwa H.; Kimoto, T; Suda, J. *Electron Device Letters, IEEE*, **2012**, *33*. 1598-1600.

40. a) Knickerbocker, T.; Strother, T.; Schwartz, M. P.; Russell, Jr. J. N.; Butler, J.; Smith, L. M.; Hamers, R. J. *Langmuir* **2003**, *19*, 1938-1942. b) Ruther, R. E.; Rigsby, M. L.; Gerken, J. B.; Hogendoorn, S. R.; Landis, E. C.; Stahl, S. S.; Hamers, R. J. *J. Am. Chem. Soc.* **2011**, *133*, 5692-5694.

41. a), Kim, C. S.; Mowrey, R. C.; Butler, J. E.; Russell Jr.; J. N. *J. Phys. Chem. B* **1998**, *102*, 9290-9296. b) Nakamura, T.; Suzuki, M.; Ishihara, M.; Ohana, T.; Tanaka, A.; Koga, Y. *Langmuir* **2004**, *20*, 5846-5849.

42. a) Lockett, M. R.; Smith, L. M. *Langmuir* **2010**, *26*, 16642-16646. b) Lockett, M. R.; Smith, L. M. *Langmuir* **2009**, *25*, 3340-3343. c) Lockett, M. R.; Smith, L. M. *J. Phys. Chem. C* **2010**, *114*, 12635-12641.

43. a) Mann, J. A.; Dichtel, W. R. *ACS Nano* **2013**, *7*, 7193-7199. b) Mann, J. A.; Rodríguez-López, J.; Abruña, H. D.; Dichtel, W. R. *J. Am. Chem. Soc.* **2011**, *133*, 17614-17617. c) Goff, A. L.; Reuillard, B.; Cosnier, S. *Langmuir* **2013**, *29*, 8736-8742. d) Zhao, Y.-L.; Stoddart, J. F. *Acc. Chem. Res.* **2009**, *42*, 1161-1171.

44. a) Bernard, M.-C.; Chaussé, A.; Cabet-Deliry, E.; Chehimi, M. M.; Pinson, J.; Podvorica, F.; Vautrin-Ul, C. *Chem. Mater.* **2003**, *15*, 3450-3462. b) Pinson, J.; Podvorica, F. *Chem. Soc. Rev.* **2005**, *34*, 429-439.

45. a) Palomaki, P. K. B.; Dinolfo, P. H. *Langmuir* **2010**, *26*, 9677-9685. b) Upadhyay, A. P.; Behara, D. K.; Sharma, G. P.; Bajpai, A.; Sharac, N.; Ragan, R.; Pala, R. G. S.; Sivakumar, S. *ACS Appl. Mater. Interface* **2013**, *5*, 9554-9562. c) Luo, L.; Frisbie, C. D. *J. Am. Chem. Soc.* **2010**, *132*, 8854-8855.

46. a) Choi, S. H.; Kim, B.; Frisbie, C. D. *Science* **2008**, *320*, 1482-1486. b) Choi, S. H.; Risko, C.; Delgado, M. C. R.; Kim, B.; Brédas, J.-L.; Frisbie, C. D. *J. Am. Chem. Soc.* **2010**, *132*, 4358-4368.

47. a) Liu, J.; Chen, M.; Qian, D.-J. *Colloid. Surface. A* **2013**, *436*, 953-960. b) Lee, S. W.; Kim, B.-S.; Chen, S.; Shao-Horn, Y.; Hammond, P. T. *J. Am. Chem. Soc.* **2009**, *131*, 671-679. c) Decher, G. *Science* **1997**, *277*, 1232-1237.

48. a) Shida, A.; Sugimura, H.; Futsuhara, M.; Takai, O. *Surf. Coat. Tech.* **2003**, *169-170*,

686-690. b) Sugimura, H.; Yonezawa, H.; Asai, S.; Sun, Q.-W.; Ichii, T.; Lee, K.-H.; Murase, K.; Noda, K.; Matsushige, K. *Colloid Surface A* **2008**, *321*, 249-253. c) Chaikin, Y.; Leader, H.; Popovitz-Biro, R.; Vaskevich, A.; Rubinstein, I. *Langmuir* **2011**, *27*, 1298-1307. d) Wanunu, M.; Popovitz-Biro, R.; Cohen, H.; Vaskevich, A.; Rubinstein, I. *J. Am. Chem. Soc.* **2005**, *127*, 9207-9215. e) Wanunu, H.; Vaskevich, A.; Cohen, S. R.; Cohen, H.; Arad-Yellin, R.; Shanzer, A.; Rubinstein, I. *J. Am. Chem. Soc.* **2005**, *127*, 17877-17887. f) Oo, L.; Kitamura, F. *J. Electroanal. Chem.* **2008**, *619-620*, 187-192.

49. a) Tuccitto, N.; Delfanti, I.; Torrisi, V.; Scandola, F.; Chiorbolo, C.; Stepanenko, V.; Würthner, F.; Licciardello, A. *Phys. Chem. Chem. Phys.* **2009**, *11*, 4033-4038. b) Kosbar L.; Srinivasan, C.; Afzali, A.; Graham, T.; Copel, M.; Krusin-Elbaum, L. *Langmuir* **2006**, *22*, 7631-7638. c) Pan, Y. Tong, B.; Shi, J.; Zhao, W.; Shen, J.; Zhi, J.; Dong, Y. *J. Phys. Chem. C* **2010**, *114*, 8040-8047. d) Tuccitto, N.; Ferri, V.; Cavazzini, M.; Quici, S.; Zhavnerko, G.; Licciardello, A.; Rampi, M. A. *Nat. Mater.* **2009**, *8*, 41-46. e) Musumeci, C.; Zappalà, G.; Martsinovich, N.; Orgiu, E.; Schuster, S.; Quici, S.; Zharnikov, M.; Troisi, A.; Licciardello, A.; Samori, P. *Adv. Mater.* **2014**, *26*, 1688-1693. f) Poppenberg, J.; Richter, S.; Traulsen, C. H.-H.; Darlatt, E.; Baytekin, B.; Heinrich, T.; Deutinger, P. M.; Huth, K.; Unger, W. E. S.; Schalley, C. A. *Chem. Sci.* **2013**, *4*, 3131-3139.

50. a) Motiei, L.; Feller, M.; Evmenenko, G.; Dutta, P.; van der Boom, M. E. *Chem. Sci.* **2012**, *3*, 66-71. b) Mondal, P. C.; Lakshmanan, J. Y.; Hamoudi, H.; Zharnikov, M.; Gupta, P. C. *J. Phys. Chem. C* **2011**, *115*, 16398-16404. c) Cai, Y.-Q.; Ren, X.-B.; Wang, H.-L.; Huang, H.-X.; Chen, M.; Qian, D.-J. *Synthetic Met.* **2012**, *162*, 1871-1878. d) Chen, H.-T.; Liu, B.; Wang, H.-T.; Xiao, Z.-D.; Chen, M.; Qian, D.-J. *Mat. Sci. Eng. C* **2007**, *27*, 639-645. e) Gao, S.; Huang, Y.; Cao, M.; Liu, T.-f.; Cao, R. *J. Mater. Chem.* **2011**, *21*, 16467-16472. f) Altman, M.; Shukla, A. D.; Zubkov, T.; Evmenenko, G.; Dutta, P.; van der Boom, N. E. *J. Am. Chem. Soc.* **2006**, *128*, 7374-7382. g) Ren, X.-B.; Chen, M.; Qian, D.-J. *Langmuir* **2012**, *28*, 7711-7719. h) Mondal, P. C.; Chhatwal, M.; Lakshmanan, Y.; Jeyachandran, L. Zharnikov, M. *J. Phys. Chem. C* **2014**, *118*, 9578-9587. i) Tang, Y.; Chen, M.; Qian, D.-J.; Zhang, L.; Liu, M. *Colloid Surface A* **2014**, *457*, 41-48.

51. a) Shekhah, O.; Wang, H.; Strunskus, T.; Cyganik, P.; Zacher, D.; Fischer, R.; Wöll, C. *Langmuir* **2007**, *23*,7440-7442. b) Liu, J.; Chen. M.; Qian, D.-J. *Langmuir* **2012**, *28*, 9496-9505. c) Kanaizuka, K.; Haruki, R.; Sakata, O.; Yoshimoto, M.; Akita, Y.; Kitagawa, H. *J. Am. Chem. Soc.* **2008**, *130*, 15778-15779. d) Schrader, I.; Witting, L.; Richter, K.; Vieker, H.; Beyer, A.; Gölzhäuser, A.; Hartwig, A.; Swiderek. P. *Langmuir* **2014**, *30*, 11945-11954.

52. a) Abe, M.; Michi, T.; Sato, A.; Kondo, T.; Zhou, W.; Ye, S.; Uosaki, K.; Sasaki, Y. *Angew. Chem. Int. Ed.* **2003**, *42*, 2912-2915. b) Zhao, W.; Tong, B.; Pan, Y.; Shen, J.; Zhi, J.; Shi,

J.; Dong, Y. *Langmuir* **2009**, *25*, 11796-11801.

53. a) Altman, M.; Zenkina, O. V.; Ichiki, T.; Iron, M. A.; Evmenenko, G.; Dutta, P.; van der Boom, M. E. *Chem. Mater.* **2009**, *21*, 4676-4684. b) Lokesh, K. S.; Chardon-Noblat, S.; Lafolet, F.; Traoré, Y.; Gondran, C.; Guionneau, P.; Guérente, L.; Labbé, P.; Deronzier, A.; Létard, J.-F. *Langmuir* **2012**, *28*, 11779-11789.

54. a) Zhao, W.; Tong, B.; Shi, J.; Pan, Y.; Shen, J.; Zhi, J.; Chan, W. K.; Dong, Y. *Langmuir* **2010**, *26*, 16084-16089. b) Tong, B.; Yang, H.; Xiong, W.; Xie, F.; Shi, J.; Zhi, J.; Chan, W. K.; Dong, Y. *J. Phys. Chem. B* **2013**, *117*, 5338-5344.

55. Driscoll, P. F.; Douglass Jr., E. F.; Phewluangdee, M.; Soto, E. R.; Cooper, C. G. F.; MacDonald, J. C.; Lambert, C. R.; McGimpsey, W. G. *Langmuir* **2008**, *24*, 5140-5145.

56. Abdelrazzaq, F. B.; Kwong, R. C.; Thompson, M. E.; *J. Am. Chem. Soc.* **2002**, *124*, 4796-4803.

57. Lin, C.; Kagan, C. R. *J. Am. Chem. Soc.* **2003**, *125*, 336-337.

58. de Ruiter, G.; Lahav, M.; Keisar, H.; van der Boom, M. E. *Angew. Chem. Int. Ed.* **2013**, *52*, 704-709.

59. a) Kanaizuka, K.; Murata, M.; Nishimori, Y.; Mori, I.; Nishio, K.; Masuda, H.; Nishihara, H. *Chem. Lett.* **2005**, *34*, 534-535. b) Ohba, Y.; Kanaizuka, K.; Murata, M.; Nishihara, H. *Macromol. Symp.* **2006**, *235*, 31-38. c) Nishimori, Y.; Kanaizuka, K.; Murata, M.; Nishihara, H. *Chem. Asian J.* **2007**, *2*, 367-376. d) Utsuno, M.; Toshimitsu, F.; Kume, S.; Nishihara, H. *Macromol. Symp.* **2008**, *270*, 153-160. e) Nishimori, Y.; Kanaizuka, K.; Kurita, T.; Nagatsu, T.; Segawa, Y.; Toshimitsu, F.; Muratsugu, S.; Utsuno, M.; Kume, S.; Murata M.; Nishihara, H. *Chem. Asian J.* **2009**, *4*, 1361-1367. f) Kurita, T.; Nishimori, Y.; Toshimitsu, F.; Muratsugu, S.; Kume, S.; Nishihara H. *J. Am. Chem. Soc.* **2010**, *132*, 4524-4525. g) Nishimori, Y.; Maeda, H.; Katagiri, S.; Sendo, J.; Miyachi, M.; Sakamoto, R,; Yamanoi, Y.; Nishihara, H. *Macromol. Symp.* **2012**, *317-318*, 276-285. h) Katagiri, S.; Sakamoto, R.; Maeda, H.; Nishimori, Y.; Kurita, T.; Nishihara, H. *Chem. Eur. J.* **2013**, *19*, 5088-5096. i) Sakamoto, R.; Katagiri, S.; Maeda, H.; Nishihara, H. *Chem. Lett.* **2013**, *42*, 553-555. j) Sakamoto, R.; Ohirabaru, Y.; Matsuoka, R.; Maeda, H.; Katagiri, S.; Nishihara, H. *Chem. Commun.* **2013**, *49*, 7108-7110.

60. Miyachi, M.; Ohta, M.; Nakai, M.; Kubota, Y.; Yamanoi, Y.; Yonezawa, T.; Nishihara, H. *Chem. Lett.* **2008**, *37*, 404-405.

61. Maeda, H.; Sakamoto, R.; Nishimori, Y.; Sendo, J.; Toshimitsu, F.; Yamanoi Y.; Nishihara, H. *Chem. Commun.* **2011**, *47*, 8644-8646.

62. a) Maeda, H.; Sakamoto, R.; Nishihara, H. *Polymer* **2013**, *54*, 4383-4403. b) Klausen, R. S.; Widawsky, J. R.; Steigerwald, M. L.; Venkataraman, L.; Nuckolls, C. *J. Am. Chem. Soc.* **2012**, *134*, 4541-4544. c) Sachs, S. B.; Dudek, S. P.; Hsung, R. P.; Sita, L. R.; Smalley, J.

F.; Newton, M. D.; Feldberg, S. W.; Chidsey, C. E. D. *J. Am. Chem. Soc.* **1997**, *119*, 10563 -10564. d) Weber, K.; Hockett, L.; Creager, S. *J. Phys. Chem. B* **1997**, *101*, 8286-8291. e) Smalley, J. F.; Finklea, H. O.; Chidsey, C. E. D.; Linford, M. R.; Creager, S. E.; Ferraris, J. P.; Chalfant, K.; Zawodzinsk, T.; Feldberg, S. W.; Newton, M. D. *J. Am. Chem. Soc.* **2003**, *125*, 2004-2013. f) Carter, M. T.; Rowe, G. K.; Richardson, J. N.; Tender, L. M.; Terrill, R. H.; Murray, R. W. *J. Am. Chem. Soc.* **1995**, *117*, 2896-2899.

Chapter 2

Quantitative evaluation of anchor ligand effect on the electron transfer rate constant

2-1 Introduction

  In molecular devices, a junction between an electrode and a molecule has an important role in the electron transport property. The establishment of an effective junction is required to realize a high performance molecular system.

  One of the evaluation methods for electron transport ability is the conductivity measurement using the break junction technique [1], the electrode-molecule-electrode sandwiched devices [2], and the conductive AFM [3]. From these measurements, not only the conductivity of molecules but also $I - V$ properties and the effect of molecule-electrode junction can be obtained. The conductance difference between Au-S and Au-C bonds is one of the important examples. The Au-C bond shows the higher conductivity than that of Au-S bond while the Au-S bond has been often used to form SAMs on gold electrode [4]. Therefore, the recent development of SAM formation methods using Au-C bond (Chapter 1, Table 1-3-1) is significant to construct effective charge transport systems. However, the recent report shows that we can decrease the contact resistance between an electrode and a molecule confined via Au-S bond. The replacement from thiolate anchor to carbodithioate anchor improves the single molecular conductance [5]. The junction effect of anchor unit on the conductance for SAMs on silicon electrode was also reported recently. Harada and his coworkers prepared aromatic SAMs linked by three bond types (Si-O-Ph, Si-CH$_2$-CH$_2$-Ph, and Si-CH=CH-Ph), and found that Si-O-Ph showed the higher conductivity in $I - V$ curves measured by Hg-SAM-Si junction [6].

  Although the conductance measurement by metal-molecule-metal junction is a powerful tool, the obtained results are sometimes influenced by the measurement condition such as the bonding state between a molecule and STM tip [7], and the set point of SPM tip [8]. Another approach for the evaluation of electron transport property is electrochemical measurement of redox active SAMs. Usually, the measurement is performed in an electrolyte solution, and molecules in SAMs can take a relaxed structure in this situation. Therefore, it is expected that the collected result will show the electron transport property of molecule in a spontaneous state.

  Some articles about the electron transfer rate constant (k_{ET}) of SAMs on silicon have been reported. Ferrocene SAMs have often been used to estimate the electron transfer rate constant values [9], and their values were reported as $5.5 - 10^5$ s^{-1}. Yzambart and coworkers fabricated a tetrathiafulvalene (TTF) SAM and determined its k_{ET} values as 270 s^{-1} for the TTF/TTF$^{•+}$ and 400 s^{-1} for the TTF$^{•+}$/TTF^{2+} in the sample prepared at 45 °C [10]. The k_{ET} value of porphyrin SAMs and its dependency on the surface coverage was estimated as $(0.5 - 5) \times 10^5$ s^{-1} by AC voltammetry [11].

  Although the estimation of k_{ET} values for various redox active SAMs on silicon has been

reported as shown above, the measurement conditions, the evaluation methods, and the molecular structure connecting an electrode and a redox center were different from one report to another. In addition, the number of systematic researches for k_{ET} values is small. In order to estimate the anchor unit effect on the electron transport, the one redox moiety linked by various anchor molecules is required, and the measurement conditions and methods should be consistent. In this section, the Fe(tpy)$_2$ complex was confined via 4-type anchor ligands on hydrogen-terminated silicon(111) electrode, and their k_{ET} values were estimated by the potential-step chronoamperometry (PSCA) technique. As anchor molecules for the investigation of molecular structure, 4'-ethynyl-2,2':6',2"-terpyridine (A^1) without a phenylene bridge and 4'-(4-ethynylphenyl)-2,2':6',2"-terpyridine (A^2) including a phenylene bridge. They are confined on a hydrogen-terminated silicon surface via Si-C covalent bond by hydrosilylation. Along with these two anchor ligands, 4'-hydroxyl-2,2':6',2"-terpyridine (A^3) and 4-(2,2':6',2"-terpyridin)-4'-yl-phenol (A^4) immobilized via Si-O-C bond were used to evaluate the effect of the bonding type on the electron transfer.

2-2 Experimental section

General

4'-Ethynyl-2,2':6',2''-terpyridine (A^1) [12] was synthesized according to the literature in our laboratory. 4'-Hydroxyl-2,2':6',2''-terpyridine (A^3) was purchased from Wako Pure Chemical Industry. P-type silicon (111) wafer (B-doped, ≤ 0.005 Ωcm) was purchased from E&M Corporation. Toluene was purified by Ultra Solvent Purifier 6-S (Nikko Hansen) or distilled with CaH_2. 1,4-Dioxane was purchased from Kanto Chemical and distilled with CaH_2. A 40 % NH_4F solution was purchased from Stella Chemifa Corporation. 4,4''''-(1,4-Phenylene)bis(2,2':6',2''-terpyridine) (L) and $Fe(BF_4)_2 \cdot 6H_2O$ were purchased from ALDRICH. HPLC-grade solvents (ethanol, chloroform and dichloromethane) were purchased from Kanto Chemical and used as received. Milli-Q water was prepared by a Milli-Q purification system (Millipore). Tetra-n-buthylammonium perchloride ($^nBu_4NClO_4$, TBAP) was purchased from TCI, recrystallized from ethanol, and dried under vacuum.

Synthesis of A^2

4'-(4-Ethynylphenyl)-2,2':6',2''-terpyridine (A^2) was synthesized according to the literature [13]. The compound was obtained as a colorless powder. 597.2 mg (31 %). ^{1}H NMR (400 MHz, CDCl$_3$) δ (ppm): 8.74-8.73 (m, 4H), 8.68 (d, $J = 8.0$ Hz, 2H), 7.91-7.89 (m, 4H), 7.64 (d, $J = 8.3$ Hz, 2H), 7.36 (ddd, $J = 7.6, 4.9, 1.2$ Hz, 2H), 3.19 (s, 1H).

Synthesis of A^4

4-(2,2':6',2''-Terpyridin)-4'-yl-phenol (A^4) was synthesized according to the literature [14]. The compound was obtained as a colorless powder. 549.8 mg (84 %). ^{1}H NMR (400 MHz, DMSO-d$_6$) δ (ppm): 8.75 (ddd, $J = 4.9, 1.7, 1.0$ Hz, 2H), 8.66-8.64 (m, 4H), 8.02 (td, $J = 7.8, 2.0$ Hz, 2H), 7.78 (d, $J = 8.8$ Hz, 2H), 7.51 (ddd, $J = 7.3, 4.9, 1.0$ Hz), 6.96 (d, J = 8.5 Hz, 2H). FAB-MS $m/z = 326$ [M+H$^+$].

Stepwise fabrication of Fe(tpy)$_2$ complex on Si electrodes

A silicon wafer was immersed in Piranha solution (a mixed solution of conc. H_2SO_4 and H_2O_2 aq., the ratio was 3:1) for 10 minutes at 120 °C, and an oxidized surface was formed. (*Piranha solution should be handled very carefully with suitable protectors because of its very strong oxidizing ability.*) The oxidized Si wafer was stored in Milli-Q water. Just before use, the wafer was dried by Ar blow, and cut in ca. 1.5 cm × 1.5 cm pieces. The cut wafers were immersed in a 40 % NH_4F solution for 10 minutes at room temperature, and a hydrogen-terminated surface was prepared. The hydrogen-terminated Si was immersed in a 1

mM solution of an anchor ligand solution ($\mathbf{A^1}$ and $\mathbf{A^2}$: toluene, $\mathbf{A^3}$ and $\mathbf{A^4}$: 1,4-dioxane), and refluxed for 1 hour under an inert atmosphere. After the reaction, the wafers were rinsed ultrasonically with toluene or 1,4-dioxane (the same solvent used for the anchor ligand modification), ethanol and Milli-Q for 5 minutes each. The terpyridine-terminated substrates were dipped in a 0.1 M $Fe(BF_4)_2 \cdot 6H_2O$ ethanol solution for 1 hour at room temperature, rinsed with Milli-Q and ethanol, and dried by N_2 blow. Finally, in order to form $Fe(tpy)_2$ complex, the iron-terminated wafers were immersed in a 0.1 mM chloroform solution of $\mathbf{L}$ for overnight at room temperature, washed with chloroform and dried by N_2 flow (Figure 2-2-1).

Electrochemical measurement

Electrochemical measurements (cyclic voltammetry and chronoamperometry) were performed with an ALS 650DT electrochemical analyzer using an Ag^+/Ag (Ag wire immersed in an acetonitrile solution including 10 mM $AgClO_4$ and 0.1 M Bu_4BClO_4) reference electrode, a platinum wire as a counter electrode and a modified silicon substrate as a working electrode. All potential values written in this thesis refer to the potential of Ag^+/Ag reference electrode. The electrode area was defined by O-ring as 0.264 cm^2. In order to make an ohmic contact, In-Ga alloy was rubbed on a silicon substrate, and a copper plate was attached. All measurements were carried out in a 1 M Bu_4BClO_4-dichloromethane solution under dark at room temperature.

As for potential-step chronoamperometry (PSCA), the redox potential ($E^{0'}$) of $[Fe(tpy)_2]^{3+/2+}$ was calculated as the average of oxidation peak potential and reduction peak potential. At first, the applied potential was kept at $E^{0'}-\eta$ (η: overpotential), and then the potential was jumped to $E^{0'}+\eta$ in order to observe the oxidation current decay with time. Next, the potential $E^{0'}-\eta$ was applied to observe the reduction current decay with time. In order to obtain the average and standard deviation values of the electron transfer rate constant (k_{ET}), more than 5 samples were measured.

^{1}H NMR spectroscopy and FAB-MS

^{1}H NMR spectra were collected by a JNM-AL400 spectrometer (400 MHz) (JEOL). FAB-MS were recorded with JMS-700P (JEOL).

X-ray photoelectron spectroscopy

All XPS measurements were performed with PHI5000 VersaProbe (ULVAC‐PHI). A monochromatic Al Kα (100 W) was used as the X−ray source. A peak for the Si 2p of Si(0) at 99.2 eV was used as a reference for the peak position calibration.

Atomic force microscopy

   Agilent5500 equipped with PPP-NCL probe (Nanoworld) was used for AFM measurements. All images were recorded using AC-AFM measurement technique under ambient condition.

DFT calculation

   Gaussian 09 [15)] was used for DFT calculations at the B3LYP/TZVP level. In order to decrease the calculation cost, Si(111) surface was mimicked by tris(silyl)silyl (-Si(SiH$_3$)$_3$) group, and **L** was replaced to 2,2':6',2"-terpyridine in the model molecules, Si-**A^{x}Fetpy** (x = 1 − 4) (Figure 2-2-2). The analytical frequency calculation for all optimized structures except Si-**A^{2}Fetpy** were performed to confirm the completion of the optimize calculation. Due to the limitation of our calculation resource, the numerical frequency calculation was performed for Si-**A^{2}Fetpy**. In the estimation of the molecular orbital and energy, the solvation of dichloromethane was included by using the built-in package in Gaussian 09.
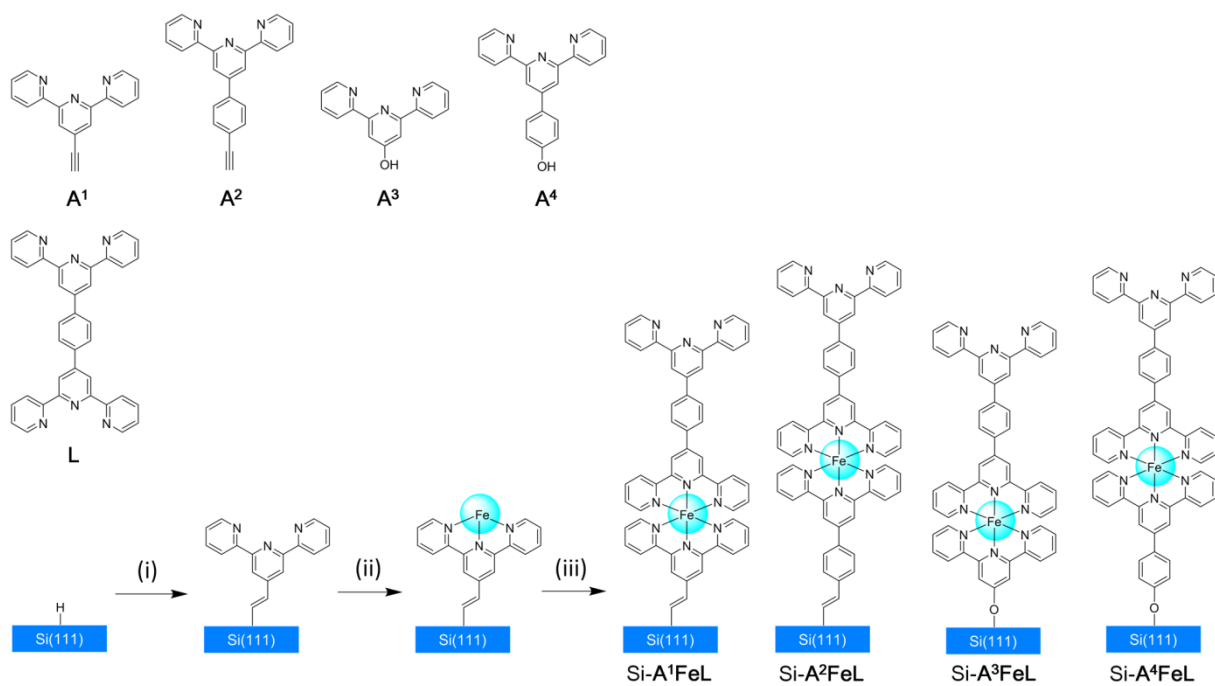
Figure 2-2-1. Structure of anchor ligands (A^x, x = 1- 4) and bridging ligand (**L**), and fabrication process of Si-A^x**FeL**; (i) modification of hydrogen-terminated silicon with A^x, (ii) coordination of Fe^{2+} ion, and (iii) coordination of **L**.
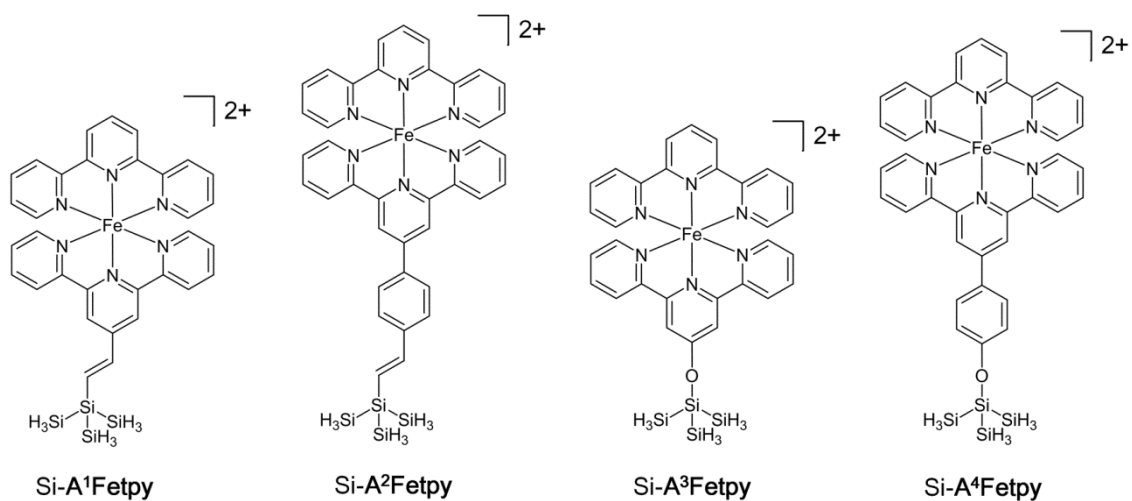

Figure 2-2-2. Structures of simplified molecules for the DFT calculation, Si-A^x**Fetpy** (x = 1 − 4).

2-3 Characterization of Fe(tpy)$_2$ complex on Hydrogen-terminated Si(111)

2-3-1 Cyclic voltammetry

Cyclic voltammetry was performed to estimate surface coverage values of Si-**A^{x}FeL** (x = 1 − 4). All samples showed a reversible redox waves at 0.830 ± 0.003 V for Si-**A^{1}FeL**, 0.812 ± 0.005 V for Si-**A^{2}FeL**, 0.825 ± 0.009 V for Si-**A^{3}FeL** and 0.820 ± 0.011 V for Si-**A^{4}FeL** (Figure 2-3-1 (A)-(D)). When this wave derives from the surface confined redox active moiety, the linear relation between the peak current (I_p) and the scan rate (v) is expressed in accordance with equation 1 [16],

$$I_\mathrm{p} = \frac{n^2 F^2 A \Gamma}{4RT} v \quad (1)$$

where n is the number of electrons involved in the reaction, F is Faraday constant, A is the surface area, Γ is the surface coverage value, R is the gas constant, and T is temperature.

The I_p − v plots for all samples exhibit the proportional relation. Therefore, these redox waves derive from the immobilized species (Figure 2-3-1 (E)-(H)). The surface coverage values were estimated from the integration of oxidation peak area as (4.7 ± 0.5) × 10^{-11} molcm^{-2} for Si-**A^{1}FeL**, (4.3 ± 0.6) × 10^{-11} molcm^{-2} for Si-**A^{2}FeL**, (4.4 ± 0.9) × 10^{-11} molcm^{-2} for Si-**A^{3}FeL** and (3.3 ± 0.7) × 10^{-11} molcm^{-2} for Si-**A^{4}FeL**. It is known that the k_ET value shows the dependency on Γ value when the coverage is small [11], while the k_ET value is constant in a redox active SAM having a high surface coverage value (> 10^{-11} molcm^{-2}) [11, 17]. The surface coverage values estimated in this research are almost constant, and included in the high coverage range. Therefore, the influence of surface packing level on k_ET values should be negligible in the discussion of anchor ligand effect on the electron transfer.
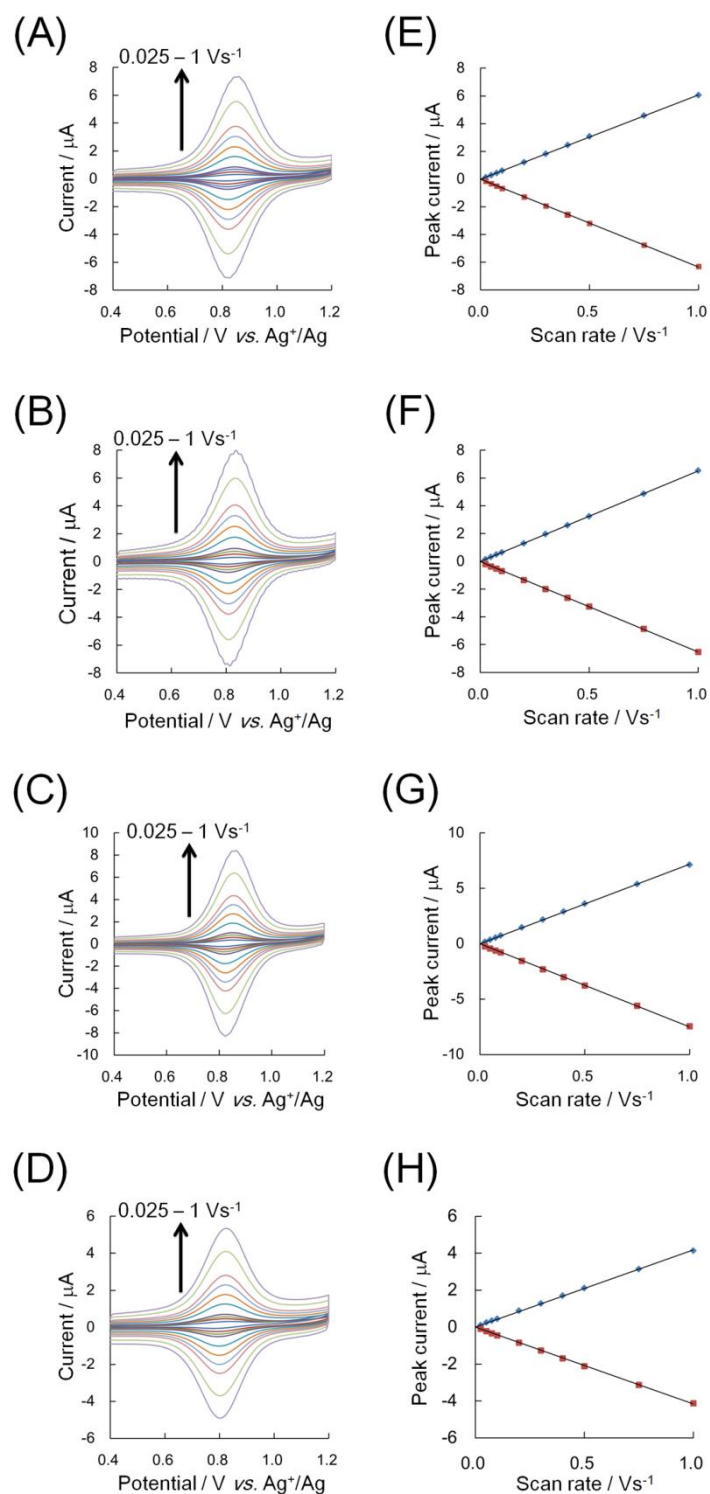
Figure 2-3-1. Cyclic voltammogrums for Si-A^1**FeL** (A), Si-A^2**FeL** (B), Si-A^3**FeL** (C) and Si-A^4**FeL** (D), and $I_p - v$ plot for for Si-A^1**FeL** (E), Si-A^2**FeL** (F), Si-A^3**FeL** (G) and Si-A^4**FeL** (H).

2-3-2 XPS measurement

In order to investigate the chemical components on the silicon surface, XPS measurements were performed. In the narrow range spectra of Si 2p, the large peak of Si $2p_{3/2}$ derived from silicon wafer was observed at 99.2 eV in each sample. The peak of Si $2p_{1/2}$ is overlapped with the Si $2p_{3/2}$ signal. The additional peak derived from oxidized silicon is also found around 103 eV. It is considered that this oxidation mainly processed during the deposition steps of Fe^{2+} ion and **L** in the ambient condition. In the high resolution spectra of Fe 2p, N 1s and F 1s regions, each sample showed the peaks at the same binding energy position (Fe: 709.6 ± 0.2 eV for $2p_{3/2}$, 722.2 ± 0.3 eV for $2p_{1/2}$, N 1s: 400.1 ± 0.1 eV, and F 1s: 686.6 ± 0.1 eV) (Figure 2-3-2). The ratio of nitrogen and iron (N/Fe) was estimated and shown in Table 2-3-1. The calculated values were slightly larger than the theoretical ratio (N/Fe = 9). The reason of these larger values can be explained by the existence of metal-free terpyridine units, and the photoelectron from iron was prevented because an iron exists at the internal of the molecular structure. These series of the results supported the existing of $Fe(tpy)_2$ moieties on the surfaces.

Table 2-3-1. Abundance ratio of N and Fe, and the N/Fe ratio.

	N / %	Fe / %	N/Fe
Si-**A^{1}FeL**	90.2	9.8	9.2
Si-**A^{2}FeL**	90.9	9.1	10
Si-**A^{3}FeL**	90.8	9.2	9.9
Si-**A^{4}FeL**	90.5	9.5	9.5
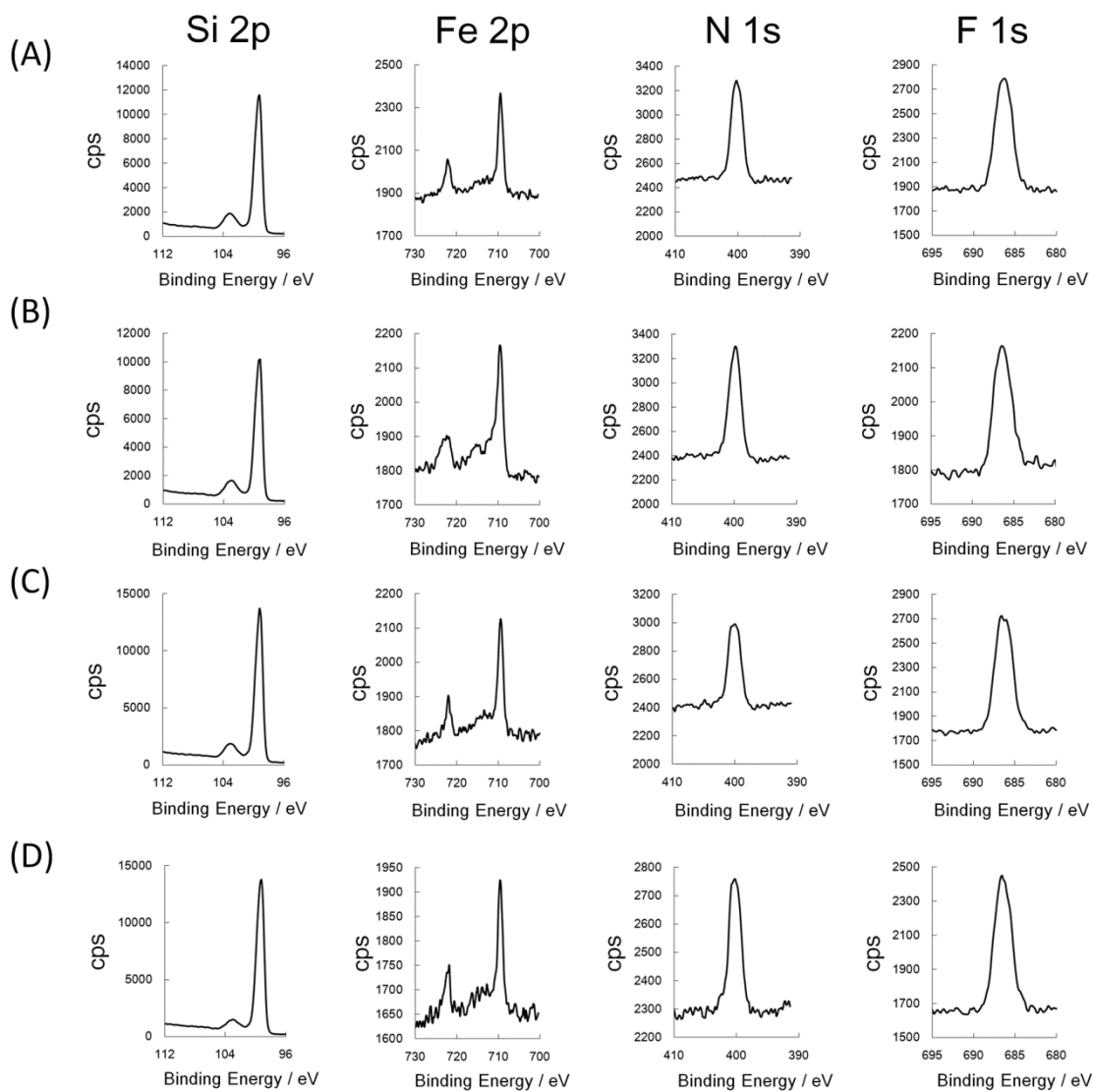
Figure 2-3-2. X-ray photoelectron spectra of Si 2p, Fe 2p, N 1s, and F 1s regions for Si-**A**[1]**FeL** (A), Si-**A**[2]**FeL** (B), Si-**A**[3]**FeL** (C) and Si-**A**[4]**FeL** (D).

2-3-3 AFM measurement

The AFM measurements were performed to obtain the topological information of silicon surface. Pristine hydrogen-terminated silicon showed a flat surface. However, a typical step-terrace structure was not obtained because its high doping density affected the hydrogen-termination process [18]. After the modification, the surface geometries were significantly changed. The unchanged flatness suggested that the $Fe(tpy)_2$ complexes were fabricated without aggregation, polymerization and oligomer formation of $Fe(tpy)_2$ in the horizontal direction (Figure 2-3-3).
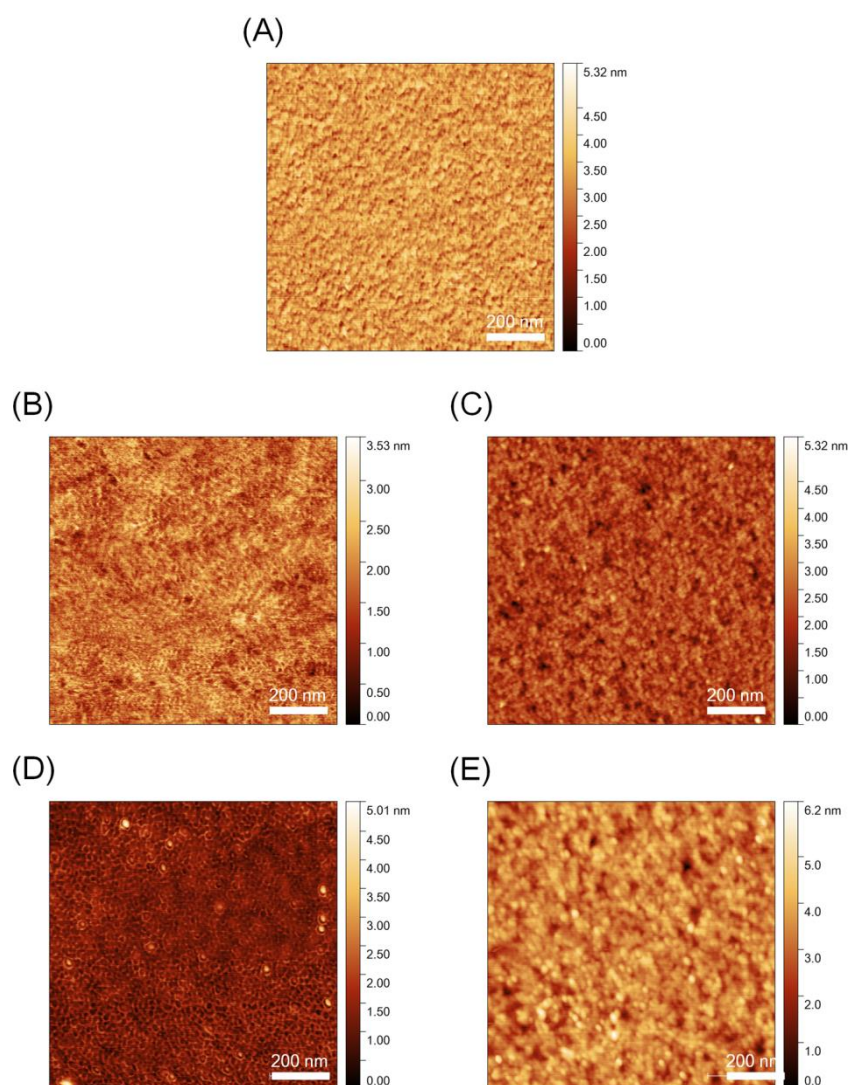

Figure 2-3-3. AFM topography images for hydrogen-terminated silicon (A), Si-**A^{1}FeL** (B), Si-**A^{2}FeL** (C), Si-**A^{3}FeL** (D) and Si-**A^{4}FeL** (E).

2-4 Estimation of electron transfer rate constant

The electron transfer rate constant (k_{ET}) values between $Fe(tpy)_2$ and silicon electrode were estimated by potential-step chronoamperometry (PSCA). The relation between the current decay derived from the Faradaic current (I) and k_{ET} was expressed by equation 2 [19].

$$I = I_0 \exp(-k_{ET}t) \quad (2)$$

Where, t is the time after applying potential, and I_0 is the current at $t = 0$. Based on this equation, k_{ET} values can be estimated from the linear slope in the $\ln I - t$ plot (Equation 3).

$$\ln I = -k_{ET}t + \ln I_0 \quad (3)$$

The k_{ET} has the dependency on the overpotential expressed by Marcus theory (Equation 4) [20].

$$k_{ET} = \upsilon \rho k_B T \int_{-\infty}^{\infty} \frac{exp\left\{-\left(\frac{k_B T}{4\lambda}\right)\left[x - \frac{\lambda \pm e\eta}{k_B T}\right]^2\right\}}{1 + \exp(x)} dx \quad (4)$$

Here, υ is the electronic coupling, ρ is the electronic state density of metallic electrode, λ is the reorganization energy, η is overpotential and k_B is Boltzmann constant. According to equations 3 and 4, the slope in $\ln I - t$ plot depends on the overpotential.

On the other hand, the current decay recorded in a chronoamperogram includes the current decay derived from the electric double layer (I_{DL}), and it can be approximated by equation 5.

$$I_{DL} = \frac{\Delta E}{R_{sol}} exp\left(-\frac{t}{R_{sol}C_{DL}}\right) \quad (5)$$

Here, ΔE is the potential difference, R_{sol} is the resistance of electrolyte solution, and C_{DL} is the capacitance of electric double layer. The natural logarithm of I_{DL} is expressed by the following equation.

$$\ln I_{DL} = -\frac{1}{R_{sol}C_{DL}}t + \ln \frac{\Delta E}{R_{sol}} \quad (6)$$

As shown in equation 6, the slope in $\ln I_{DL} - t$ does not exhibit the dependency on the overpotential. In addition, the current decay of the electric double layer is usually very rapid.

Therefore, we can obtain the k_{ET} value from the linear decay region which shows the overpotential dependency in the $\ln I - t$ plot.

The representative chronoamperograms and $\ln I - t$ plots for Si-$\mathbf{A}^x\mathbf{FeL}$ are shown in Figures 2-4-1 and 2-4-2. The current decays depending on the overpotential are observed in all chronoamperograms, and the linear decay regions are also observed in the $\ln I - t$ plots. From the slope in $\ln I - t$ plots, the k_{ET} values for Si-$\mathbf{A}^x\mathbf{FeL}$ were estimated.
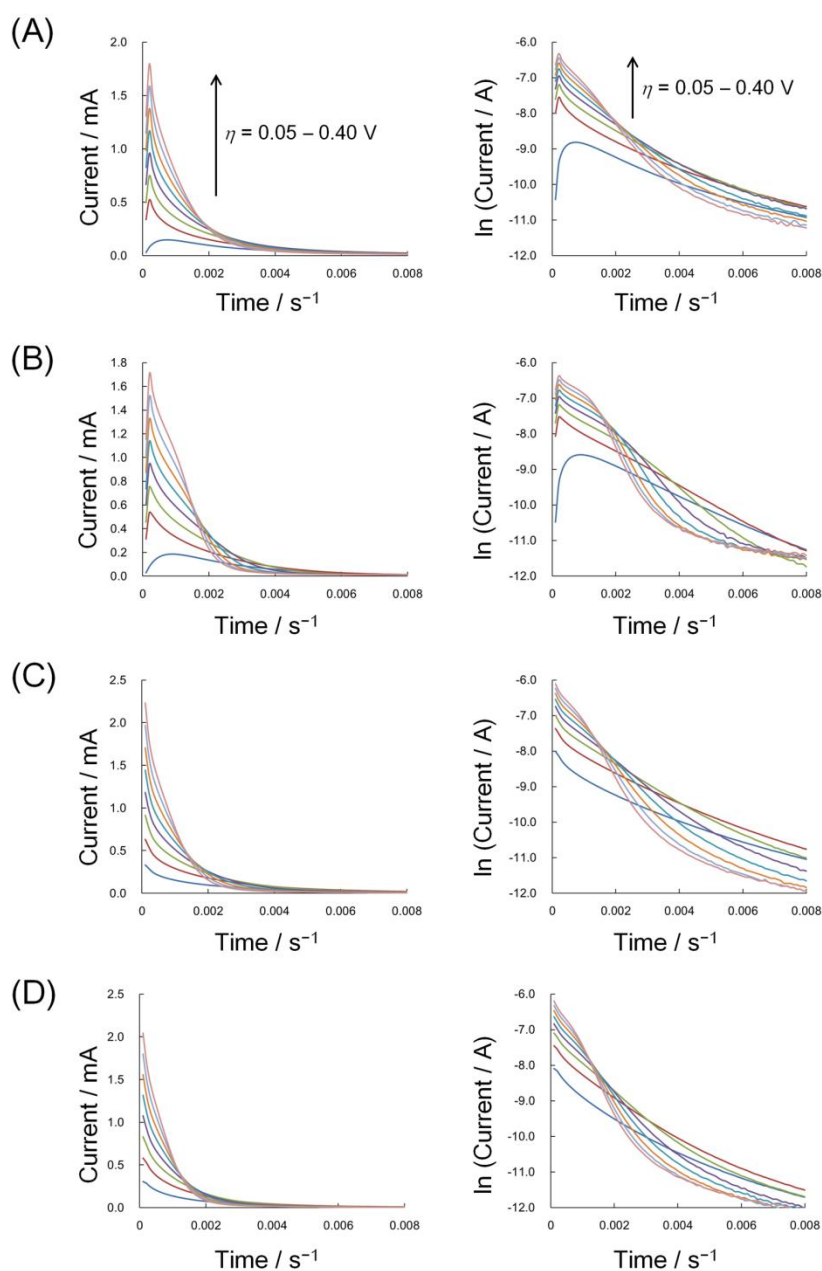

Figure 2-4-1. Representative chronoamperograms ($I - t$ plots) and $\ln I - t$ plots for oxidation current of Si-$\mathbf{A}^1\mathbf{FeL}$ (A), Si-$\mathbf{A}^2\mathbf{FeL}$ (B), Si-$\mathbf{A}^3\mathbf{FeL}$ (C) and Si-$\mathbf{A}^4\mathbf{FeL}$ (D).

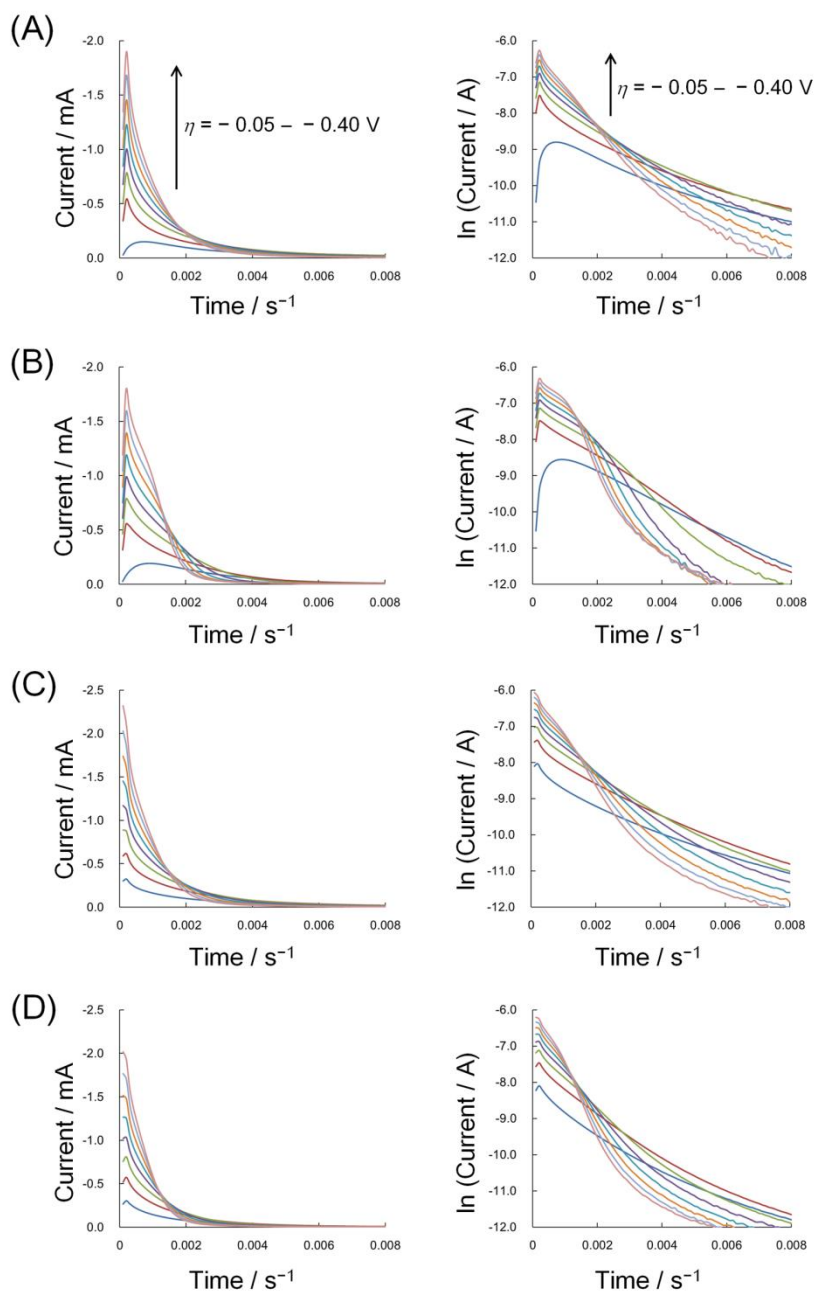**Figure 2-4-2.** Representative chronoamperograms ($I - t$ plots) and ln $I - t$ plots for reduction current of Si-**A**[1]**FeL** (A), Si-**A**[2]**FeL** (B), Si-**A**[3]**FeL** (C) and Si-**A**[4]**FeL** (D).

The obtained k_{ET} values were corrected as a Tafel plot (ln k_{ET} − η plot, Figure 2-4-3). Si-$\mathbf{A^2FeL}$ showed the larger k_{ET} values than those of Si-$\mathbf{A^1FeL}$ in the scanned overpotential range in spite of their greater distance between the redox active center and the electrode (13.3 Å for Si-$\mathbf{A^2FeL}$ and 8.97 Å for Si-$\mathbf{A^1FeL}$ from DFT calculation, Figure 2-4-4). Si-$\mathbf{A^4FeL}$ and Si-$\mathbf{A^3FeL}$ also exhibited similar trend (11.7 Å for Si-$\mathbf{A^4FeL}$ and 7.42 Å for Si-$\mathbf{A^3FeL}$ from DFT calculation, Figure 2-4-4). The former one had the larger k_{ET} values than those of the latter one. This means that the anchor ligands containing phenylene moiety ($\mathbf{A^2}$ and $\mathbf{A^4}$) gave the faster electron transport than that produced by non-phenylene anchor ligands ($\mathbf{A^1}$ and $\mathbf{A^3}$). The electron transfer rate constant for $\eta = 0$ V (k^0_{ET}) was estimated by the linear fitting of Tafel plot in $|\eta| \leq 0.25$ V region. The estimated ln k^0_{ET} values for Si-$\mathbf{A^2FeL}$ and Si-$\mathbf{A^4FeL}$ which have a phenylene-containing anchor are 5.74 ± 0.15 and 6.17 ± 0.29 respectively. On the other hand, the ln k^0_{ET} values for Si-$\mathbf{A^1FeL}$ and Si-$\mathbf{A^3FeL}$ are 5.45 ± 0.11 and 5.53 ± 0.15 respectively (Table 2-4-1). As a result, the longer-distance anchor ligands $\mathbf{A^2}$ and $\mathbf{A^4}$ gave the superior electron transport than the short anchor ligands $\mathbf{A^1}$ and $\mathbf{A^3}$.

From the comparison between Si-$\mathbf{A^1FeL}$ and Si-$\mathbf{A^3FeL}$, or Si-$\mathbf{A^2FeL}$ and Si-$\mathbf{A^4FeL}$, there is a trend that the Fe(tpy)$_2$ complexes immobilized via Si-O-C give slightly greater k_{ET} values than those of Si-C bonded complexes in spite of the disconnection of π-conjugation. The first possible reason of this phenomenon is the distance between the iron center and the electrode. $\mathbf{A^2}$ and $\mathbf{A^4}$ have shorter distance than $\mathbf{A^1}$ and $\mathbf{A^3}$ (Table 2-4-1). The second reason is the bond angle of Si-O-C bond. It is considered that Si-$\mathbf{A^1FeL}$ and Si-$\mathbf{A^2FeL}$ stand perpendicularly because a vinylene moiety substituted its *trans*-position forms a 180° dihedral angle. However, the bond angles of Si-O-C bond in the calculated structure (Si-$\mathbf{A^xFetpy}$ (x = 3, 4)) are 135.5° and 134.7° respectively. Therefore, it is expected that Si-$\mathbf{A^3FeL}$ and Si-$\mathbf{A^4FeL}$ are tilted about 45° from the vertical direction. In addition, the redox active site, Fe(tpy)$_2$ complex, exists at the middle of molecular layer. When the redox reaction occurs, the access of a counter anion from an electrolyte solution is required to keep the neutral charge of whole molecule. In the case of the tilted structures, Si-$\mathbf{A^3FeL}$ and Si-$\mathbf{A^4FeL}$, the redox center is exposed to an electrolyte solution and it makes the access of a counter anion to the metal complex easy. When the structure stands vertically, the bridging ligand ($\mathbf{L}$) prevents an counter anion approaching to the Fe(tpy)$_2$ moiety (Figure 2-4-5). Therefore, it is considered that the tilted structure formed by Si-O-C bond produces the slightly larger k_{ET} values in Si-$\mathbf{A^3FeL}$ and Si-$\mathbf{A^4FeL}$. However, the recent research by Harada and coworkers advocates that phenyl ring SAM linked via the Si-O-C bond stands almost perpendicularly [6]. Hence, there is a possibility that Si-$\mathbf{A^3FeL}$ and Si-$\mathbf{A^4FeL}$ might have the vertical structure. In addition, the SAM anchored by Si-O-C bond exhibits the higher conductance than that of Si-C bonded SAMs. According to the local density of states calculation and the Löwdin charge analysis by

Fagas and coworkers [21)], the oxygen linker shows the larger charge transfer to the surface silicon and the shift in conduction band states producing the high conductivity for Si-O-Ph SAM observed in Harada's report. The same effect might be able to apply to the Si-$\mathbf{A}^x\mathbf{FeL}$ systems.
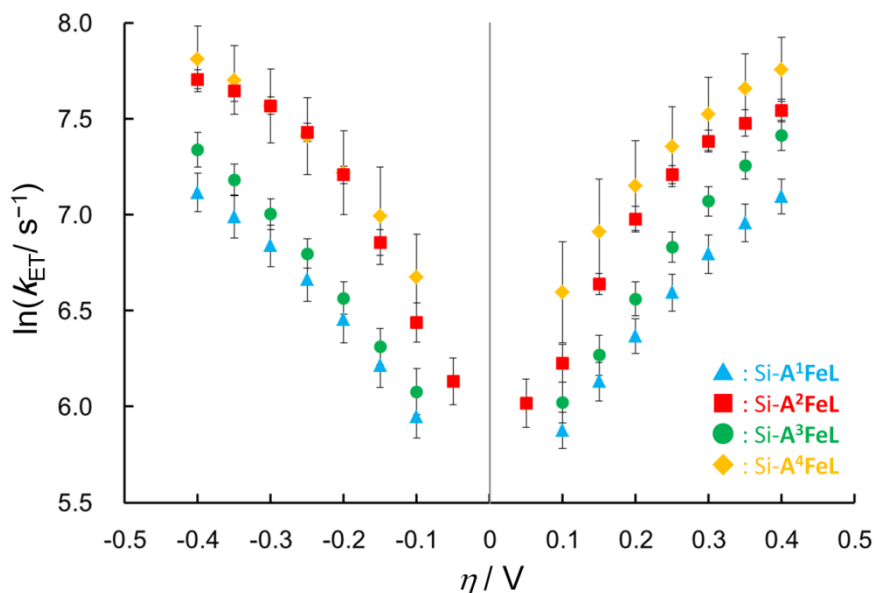

Figure 2-4-3. Tafel plots for Si-$\mathbf{A}^x\mathbf{FeL}$ ($x = 1 - 4$).

Table 2-4-1. ln k^0_{ET} values and distances between iron center and silicon surface for Si-$\mathbf{A}^x\mathbf{FeL}$ ($x = 1 - 4$). Distance was estimated from the optimized structure of Si-$\mathbf{A}^x\mathbf{Fetpy}$ ($x = 1 - 4$).

	ln (k^0_{ET} / s^{-1})	d / Å
Si-$\mathbf{A}^1\mathbf{FeL}$	5.45 ± 0.11	8.97
Si-$\mathbf{A}^2\mathbf{FeL}$	5.74 ± 0.25	13.3
Si-$\mathbf{A}^3\mathbf{FeL}$	5.53 ± 0.15	7.42
Si-$\mathbf{A}^4\mathbf{FeL}$	6.17 ± 0.29	11.7

(A) 8.97 Å

(B) 13.3 Å

(C) 7.42 Å

(D) 11.7 Å
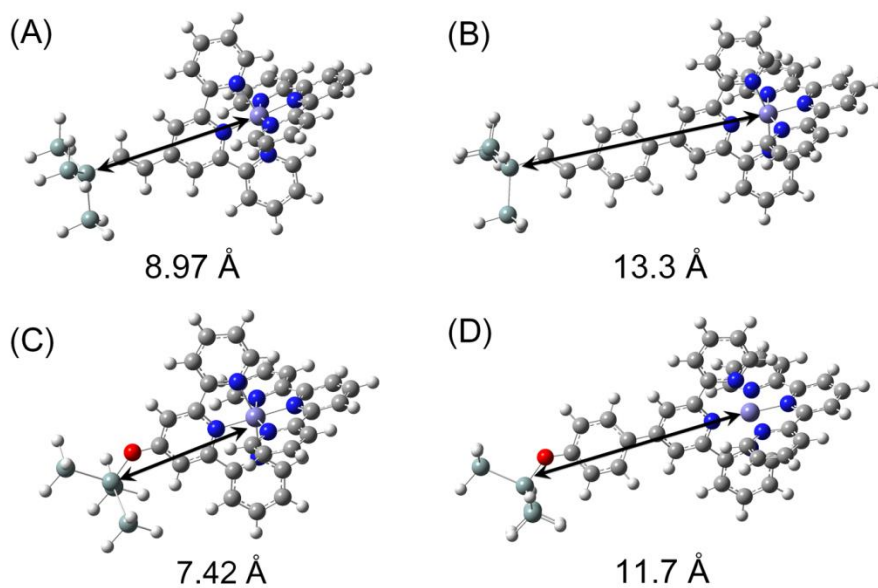
Figure 2-4-4. Optimized structures of Si-A^x**Fetpy** ($x = 1 - 4$).
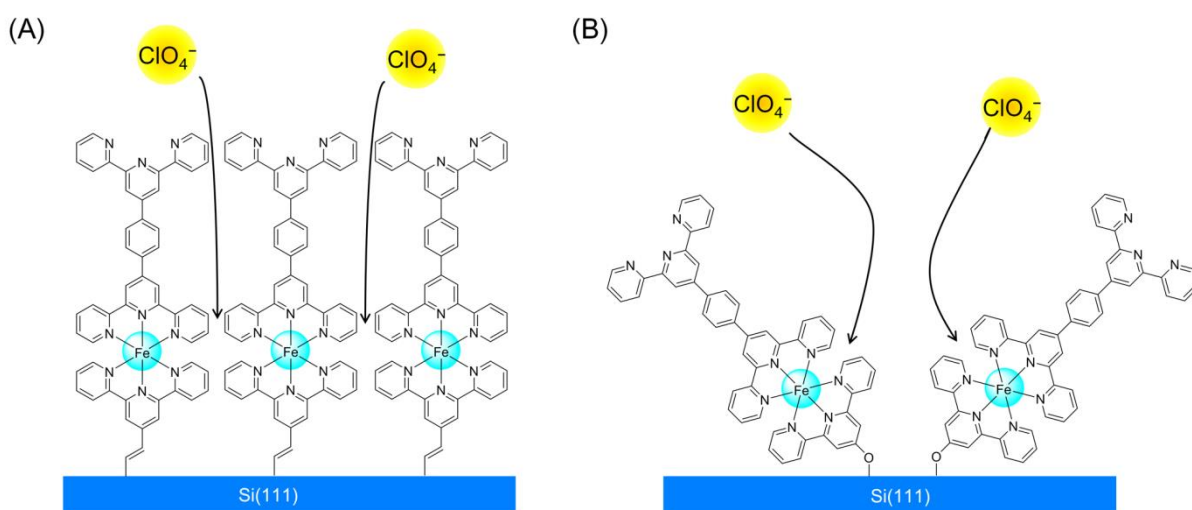

Figure 2-4-5. Estimated structures of Si-A^1**FeL** (A) and Si-A^3**FeL** (B) on silicon and counter anion approaching to them.

2-5 DFT calculation

 In order to elucidate the electron transfer phenomena observed in Si-A^xFeL, the DFT calculation was performed. In the superexchange charge transport mechanism, it is considered that the molecular orbital of bridging unit mixes to the orbitals of a donor and an accepter, and contribute to the electron transport [22]. Therefore, the information about the molecular orbital of bridging unit may help us to consider the electron transport kinetics for Si-A^xFeL.

 The structures of Si-A^xFetpy ($x = 1 - 4$) were optimized by the DFT calculation in the B3LYP/TZVP level (Figure 2-5-1). According to the estimated molecular orbitals, the HOMO, HOMO−1, HOMO−2 of Si-A^xFetpy are composed of the t_{2g} orbitals derived from Fe 3d orbitals. The HOMO−3 orbitals delocalize over the whole of anchor ligand, and connect iron center and silicon atom. Therefore, the HOMO−3 will mix to the HOMO orbital and the electronic state of electrode when the superexchange hole transport event occurs. In this scheme, a small energy gap between the HOMO and HOMO−3 ($\Delta E = E_{HOMO} - E_{HOMO-3}$) will make a strong coupling, and improve the hole superexchange transport because the mixed HOMO−3 will enhance the electronic interaction between the Fe(tpy)$_2$ moiety and the electrode. According to the calculation, Si-A^2Fetpy and Si-A^4Fetpy showed the smaller ΔE values than those of Si-A^1Fetpy and Si-A^3Fetpy (Table 2-5-1). Therefore, Si-A^2FeL and Si-A^4FeL realized the superior electron transport behavior. Although it seems to be difficult for HOMO−3 to interact with HOMO because its energy level is far from that of HOMO, the deep HOMO level contributing to the electronic communication between two redox active species is sometimes suggested in a mixed valence molecule [23]. Therefore, the electronic interaction between HOMO and HOMO−3 is possible.

 In addition, the LUMO orbitals of Si-A^1Fetpy and Si-A^2Fetpy are delocalized over the anchor ligands, and seem to be able to mediate the electron transport. However, in these molecular systems, the energy of LUMO is far from HOMO level, and the electric coupling should be very weak. Furthermore, the thermal or photo excitation from HOMO to LUMO or the valence band to the conduction band cannot occur because all measurements were performed at room temperature under dark condition. Hence, the effect of LUMO orbitals is negligible.
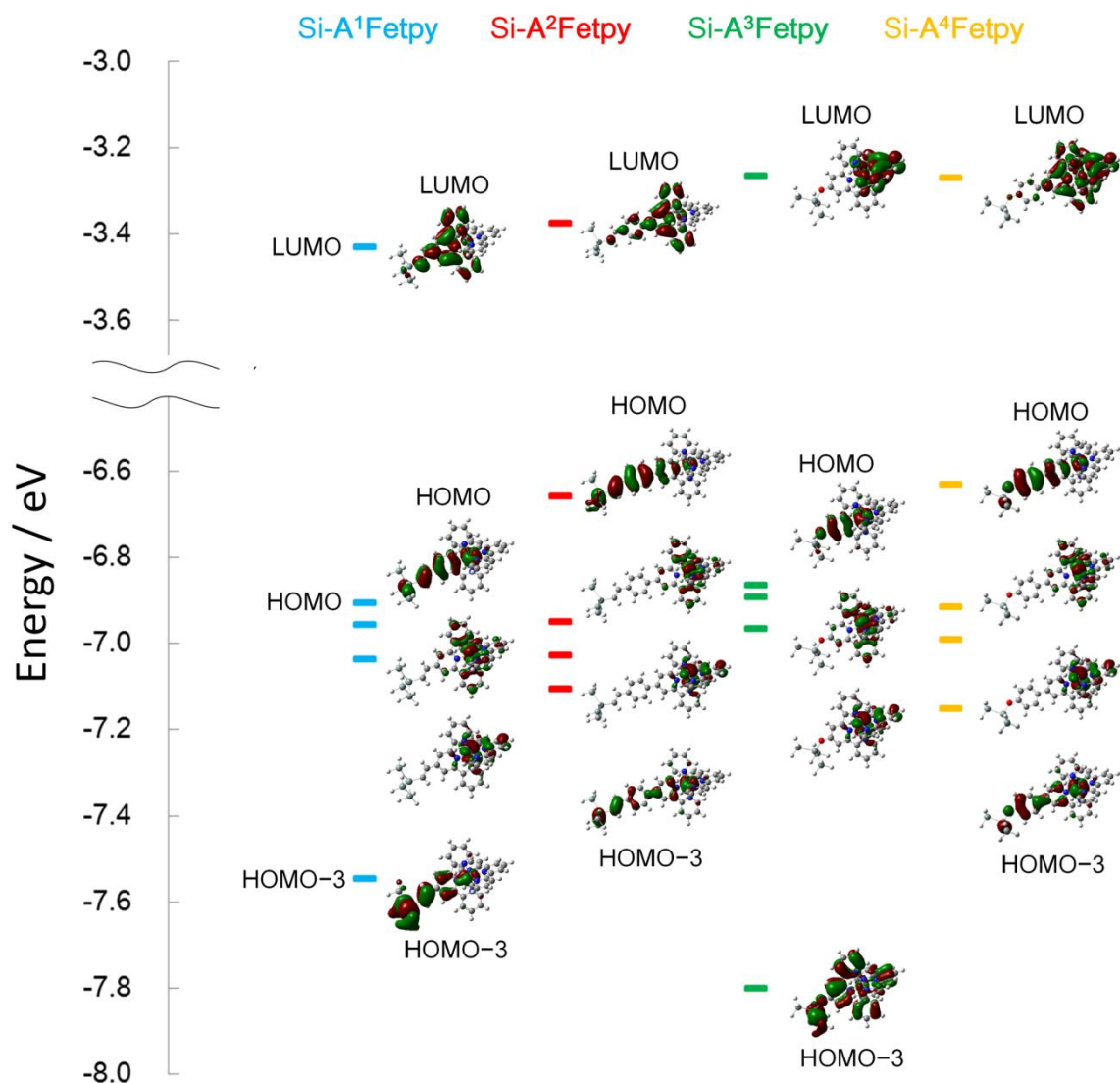
Figure 2-5-1. Molecular orbitals and energy levels for Si-A^x**Fetpy** ($x = 1 − 4$).

Table 2-5-1. Energy levels of E_{HOMO}, E_{HOMO-3} and $\varDelta E$ values for Si-A^x**Fetpy** ($x = 1 − 4$)

	E_{LUMO} / eV	E_{HOMO} / eV	E_{HOMO-3} / eV	$\varDelta E$ / eV
Si-A^1**Fetpy**	− 3.43	− 6.91	− 7.54	0.63
Si-A^2**Fetpy**	− 3.37	− 6.66	− 7.10	0.44
Si-A^3**Fetpy**	− 3.27	− 6.86	− 7.80	0.94
Si-A^4**Fetpy**	− 3.27	− 6.63	− 7.15	0.52

2-6 Conclusion [24)]

  In Chapter 2, the $Fe(tpy)_2$ complexes were fabricated on hydrogen-terminated silicon(111) substrates by the stepwise coordination technique. The preparation of the complexes was confirmed by cyclic voltammetry, X-ray photoelectron spectroscopy and atomic force microscopy. The quantitative evaluation of electron transfer rate constant was performed by potential-step chronoamperometry. The obtained result exhibits that the anchor ligands including phenylene bridge ($\mathbf{A^2}$ and $\mathbf{A^4}$) had the greater k_{ET} values in spite of their longer distance between the iron center and the silicon electrode. According to the DFT calculations, the small energy differences between HOMO and HOMO−3 levels were found in Si-$\mathbf{A^2Fetpy}$ and Si-$\mathbf{A^4Fetpy.}$ It is considered that they make the electron coupling between $Fe(tpy)_2$ and the electrode, and contribute to promote the electron transfer. The observed slightly greater k_{ET} values in the Si-O-C bridged systems (Si-$\mathbf{A^3FeL}$ and Si-$\mathbf{A^4FeL}$) might be derived from the shorter distance between the iron center and electrode, the tilted structure or the electronic state formed by the existence of an oxygen atom.

2-7 References

1. a) Chen, W.; Li, H.; Widawsky, J. R.; Appayee, C.; Venkataraman, L.; Breslow, R. *J. Am. Chem. Soc.* **2014**, *136*, 918-920. b) Moreno-García, P.; Gulcur, M.; Manrique, D. Z.; Pope, T.; Hong, W.; Kalginedi, V.; Huang, C.; Batsanov, A. S.; Bryce, M. R.; Lambert, C.; Wandlowski, T. *J. Am. Chem. Soc.* **2013**, *135*, 12228-12240. c) Hong, W.; Manrique, D. Z.; Moreno-García, P.; Gulcur, M.; Mishchenko, A.; Lambert, C. J.; Bryce, M. R.; Wandlowski, T. *J. Am. Chem. Soc.* **2012**, *134*, 2292-2304. d) Huber, R.; González, M. T.; Wu, S.; Langer, M.; Grunder, S.; Horhoiu, V.; Mayor, M.; Bryce, M. R.; Wang, C.; Jitchati, R.; Schönenberger, C.; Calame, M. *J. Am. Chem. Soc.* **2008**, *130*, 1080-1084.

2. a) Bala, S.; Aithal, R. K.; Derosa, P.; Janes, D.; Kuila, D. *J. Phys. Chem. C* **2010**, *114*, 20877-20884. b) Salomon, A.; Böcking, T.; Gooding, J. J.; Cahen, D. *Nano. Lett.* **2006**, *6*, 2873-2876. c) Querebillo, C. J.; Terfort, A.; Allara, D. L.; Zharnikov, M. *J. Phys. Chem. C* **2013**, *117*, 25556-25561.

3. a) Luo, L.; Frisbie, C. D. *J. Am. Chem. Soc.* **2010**, *132*, 8854-8855. b) Ditzler, L. R.; Karunatilaka, C.; Donuru, V. R.; Liu, H. Y.; Tivanski, A. V. *J. Phys. Chem. C* **2010**, *114*, 4429-4435. c) Engelkes, V. B.; Beebe, J. M.; Frisbie, C. D. *J. Am. Chem. Soc.* **2004**, *126*, 14287-14296.

4. (a) Schwarz, F.; Kastlunger, G.; Lissel F.; Riel, H.; Venkatesan, K.; Berke, H.; Stadler, R.; Lörtscher, E. *Nano Lett.* **2014**, *14*, 5932-5940. (b) Hong, W.; Li, H.; Liu, S.-X.; Fu, Y.; Li, J.; Kalihinedi, V.; Decurtins, S.; Wandlowski, T. *J. Am. Chem. Soc.* **2012**, *134*, 19425-19431.

5. Li, Z.; Smeu, M.; Park, T.-H.; Rawson, J.; Xing, Y.; Therien, M.-J.; Ratner, M. A.; Borguet, E. *Nano Lett.* **2014**, *14*, 5493-5499.

6. Harada, Y.; Koitaya, T; Mukai, K.; Yoshimoto, S.; Yoshinobu, J. *J. Phys. Chem. C* **2013**, *117*, 7497-7505.

7. (a) Hong, W.; Manrique, D. Z.; Moreno-García, P.; Gulcur, M.; Mishchenko, A; Lambert, C. J.; Bryce, M. R.; Wandlowski, T. *J. Am. Chem. Soc.* **2012**, *134*, 2292-2304. (b) Moreno- García, P.; Gulcur, M.; Manrique, D. Z.; Pope, T.; Hong, W.; Kaliginede, V.; Huang, C.; Batsanov, A. S.; Bryce, M. R.; Lambert, C.; Wandlowski, T. *J. Am. Chem. Soc.* **2013**, *135*, 12228-12240.

8. (a) Pawlowski, J.; Juhaniewicz, J.; Tymecka, D.; Sek, S. *Langmuir* **2012**, *28*, 17287-17294. (b) Smaali, K.; Clément, N.; Patriarche, G.; Vuillaume, D. *ACS Nano* **2012**, *6*, 4639-4647. (c) Qi, Y.; Ratera, I.; Park, J. Y.; Ashby, P. D.; Quek, S. Y.; Neaton, J. B.; Salmeron, M. *Langmuir*, **2008**, *24*, 2219-2223.

9. Fabre, B. *Acc. Chem. Res.* **2010**, *43*, 1509-1518.

10. Yzambart, G.; Fabre, B.; Camerel, F.; Roisnel, T.; Lorcy, D. *J. Phys. Chem. C* **2012**, *116*, 12093-12102.

11. Roth, K. M. Yasseri, A. A.; Liu, Z.; Dabke, R. B.; Malinovskii, V.; Schweikart, K. H.; Yu, L.; Tiznado, H.; Zaera, F.; Lindsey, J. S.; Kuhr, W. G.; Bocian, D. F. *J. Am. Chem. Soc.* **2003**, *125*, 505-517.

12. Grosshenny, V.; Romero, F. R., Ziessel, R. *J. Org. Chem.* **1997**, *62*, 1491-1500.

13. Constable, E. C.; Housecroft, C. E.; Kokotam, S. L.; Medlycott, E. A.; Zampese, J. A. *Inorg. Chem. Commun.* **2010**, *13*, 457-460.

14. Yoo, D.-W.; Yoo, S.-K. Kim, C.; Lee, J.-K. *J. Chem. Soc., Dalton Trans.* **2002**, 3931-3932.

15. Frisch, M. J.; Trucks, G. W.; Schlegel, H. B.; Scuseria, G. E.; Robb, M. A.; Cheeseman, J. R.; Scalmani, G.; Barone, V.; Mennucci, B.; Petersson, G. A.; Nakatsuji, H.; Caricato, M.; Li, X.; Hratchian, H. P.; Izmaylov, A. F.; Bloino, J.; Zheng, G.; Sonnenberg, J. L.; Hada, M.; Ehara, M.; Toyota, K.; Fukuda, R.; Hasegawa, J.; Ishida, M.; Nakajima, T.; Honda, Y.; Kitao, O.; Nakai, H.; Vreven, T.; Montgomery, J. A., Jr.; Peralta, J. E.; Ogliaro, F.; Bearpark, M.; Heyd, J. J.; Brothers, E.; Kudin, K. N.; Staroverov, V. N.; Kobayashi, R.; Normand, J.; Raghavachari, K.; Rendell, A.; Burant, J. C.; Iyengar, S. S.; Tomasi, J.; Cossi, M.; Rega, N.; Millam, M. J.; Klene, M.; Knox, J. E.; Cross, J. B.; Bakken, V.; Adamo, C.; Jaramillo, J.; Gomperts, R.; Stratmann, R. E.; Yazyev, O.; Austin, A. J.; Cammi, R.; Pomelli, C.; Ochterski, J. W.; Martin, R. L.; Morokuma, K.; Zakrzewski, V. G.; Voth, G. A.; Salvador, P.; Dannenberg, J. J.; Dapprich, S.; Daniels, A. D.; Farkas, Ö.; Foresman, J. B.; Ortiz, J. V.; Cioslowski, J.; Fox, D. J. Gaussian, Inc., Wallingford CT, 2009.

16. Eckermann, A. L.; Feld, D. J.; Shaw, J. A.; Meade, T. J. *Coord. Chem. Rev.* **2010**, *254*, 1769-1802.

17. Fabre, B.; Hauquier F. *J. Phys. Chem. B* **2006**, *110*, 6848-6855.

18. (a) Roche, J. R.; Ramonda, M.; Thibaudau, F.; Dumas, Ph.; Mathiez, Ph.; Salvan, F.; Allongue, P. *Microsc. Microanal. Microstruct.* **1994**, *5*, 291-299. (b) Ramonda, M.; Dumas, Ph.; Salvan, F. *Surf. Sci.* **1998**, *411*, L839-L843.

19. Bard, A. J.; Faulkner, L. R. *Electrochemical Methods: Fundamentals and Applications*, 2nd ed., Wiley, New York, **2001**.

20. (a) Marcus. R. A. *J. Phys. Chem.* **1963**, *67*, 853-857. (b) Marcus, R. A. *J. Chem. Phys.* **1965**, *43*, 679-701. (c) Sek, S.; Palys, B.; Bilewicz, R. *J. Phys. Chem. B* **2002**, *106*, 5907-5914.

21. Arefi, H. H.; Nolan, M.; Fagas, G. *Langmuir* **2014**, *30*, 13255-13265.

22. Paddon-Row, M. N. *Acc. Chem. Res.* **1994**, *27*, 18-25.

23. a) Muratsugu, S.; Kishida, M.-a.; Sakamoto, R.; Nishihara, H. *Chem. Eur. J.* **2013**, *19*, 17314-17327. b) Kishida, M.-a.; Muratsugu, S.; Sakamoto, R.; Kusamoto, T.; Nishihara, H. *Chem. Lett.* **2013**, *42*, 361-362.
24. Maeda, H.; Sakamoto, R.; Nishihara, H. *Chem. Eur. J.* **2014**, *20*, 2761-2764.

Chapter 3

Comparison of electron transport ability for phenylene bridege and vinylene bridge

3-1 Introduction

  As shown in Table 1-3-1 in Chapter 1, various silicon surface modification methods have been developed by many researchers. Among them, hydrosilylation reaction is one of the most important methods because the reaction using alkynes gives the vinylene bridge keeping π-conjugation from silicon electrode to the molecule. Therefore, it is expected that these molecules have the greater electron transportability. Based on this idea, the phenylene bridge which has larger π-conjugation system than vinylene bridge will show the superior charge transport ability. However, the methods which allow us to fabricate the directly-immobilized Si-aryl structure have been limited to the organometallic reagents such as R-Li and R-MgBr, and diazonium salts. In addition, organometallic reagents sometimes confine an available functional group for the SAM formation due to their high reactivity, and diazonium salts often cause the multilayer formation because of low controllability of radical reaction.

  Our group has developed the coupling reaction between iodoarenes and hydrosilnaes catalyzed by Pd(0) or Rh(I) under the coexistence of a base [1] (Figure 3-1-1(A)). This reaction allows us to synthesize the Si-aryl compounds without the protection of reactive functional group under a mild condition. Recently, our group applied this reaction to the hydrogen-terminated silicon and germanium surface modification, and reported the uniformed SAM formation and the introduction of various functional molecules on the surface by the Pd-catalyzed reaction (Figure 3-1-1(B)) [2]. We succeeded in the construction of 10-layered Fe(tpy)$_2$ complex wire based on this Si-aryl bond formation reaction. In this report, we reported the success of the directly-bonded Si-aryl SAM formation by the newly-developed method whereas the difference of its charge transport ability has not been examined yet.

  In this chapter, 4-iodophenyl-2,2':6',2''-terpyridine SAM was prepared on a hydrogen-terminated silicon(111) surface by the Pd-catalyzed reaction, and Fe(tpy)$_2$ complex was prepared using the stepwise coordination reaction. Its k_{ET} value was evaluated quantitatively by PSCA, and compared with those of Fe(tpy)$_2$ complexes confined by the traditional modification method. Especially, the difference between phenylene bridge and vinylene bridge was focused.
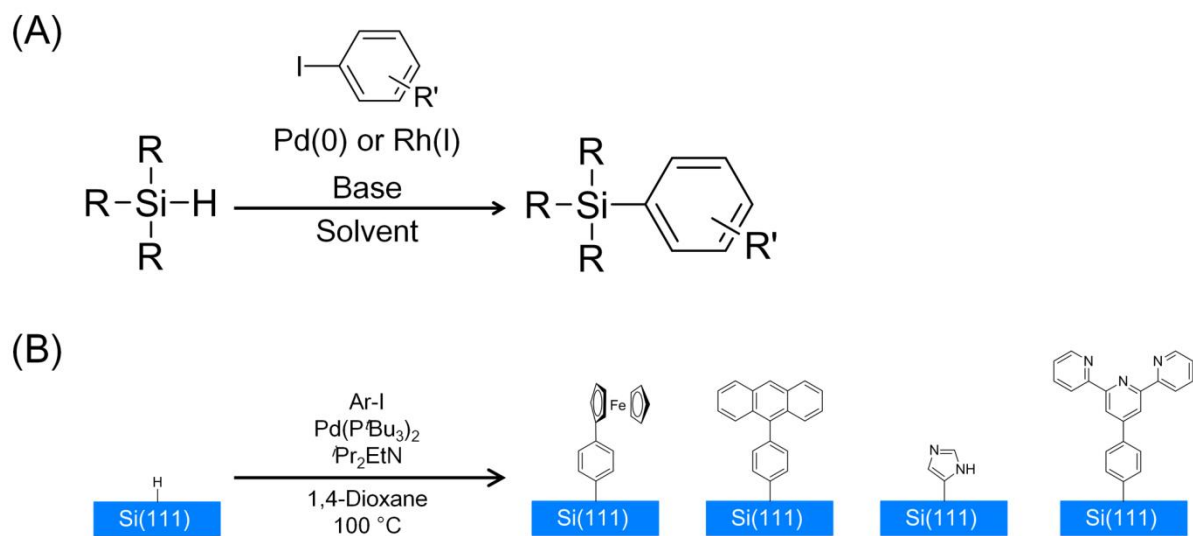
Figure 3-1-1. (A) Metal-complex-catalyzed arylation reaction for hydrosilane. (B) Direct immobilization of aryl compounds on hydrogen-terminated silicon surface by palladium-catalyzed reaction [2].

3-2 Experimental section

General

Potassium hydroxide, ammonia solution, triphenylphosphine and ethanol were purchased form Wako Chemicals. 2-Acethylpyridine was purchased from TCI. 4-Iodobenzaldehyde and Pd(P^{t}Bu$_3$)$_2$ were purchased from Aldrich. 1,4-Dioxane was purchased from Kanto Chemicals and distilled from CaH$_2$. *N*,*N*-diisopropylethylamine was purchased from TCI, distilled from CaH$_2$ and stored over KOH. Other compounds and solvents are described in the experimental section of chapter 2.

Synthesis of 4-iodophenyl-2,2':6',2-terpyridine (A^5) [3)]

A KOH aqueous solution (10 M, 0.8 mL) was added to an ethanol solution (12 mL) of 2-acetylpyridine (0.97 g, 0.9 mL, 8 mmol). After stirring at room temperature for 30 minutes, 4-iodobenzaldehyde (0.926 g, 4 mmol) was added, and the mixture was heated. Ethanol (18 mL) and NH$_3$ aq (6 mL) were sequentially added, and the mixture was refluxed for 40 hours. During the reaction, NH$_3$ aq (6mL) was added twice. After cooling to room temperature, a precipitation was collected, and washed with water and ethanol. The obtained powder was purified by the recrystallization from ethanol. 657.1 mg (38 %). ^{1}H NMR (400 MHz, CDCl$_3$) δ (ppm): 8.73 (d, J = 4.1 Hz, 2H), 8.70 (s, 2H), 8.68 (d, J = 8.0 Hz, 2H), 7.89 (td, J = 7.6 Hz, 2.0 Hz, 2H), 7.85 (d, J = 8.5Hz, 2H), 7.65(d, 8.8Hz, 2H), 7.37 (ddd, J = 7.4 Hz, 4.6 Hz, 1.2 Hz, 2H), FAB-MS m/z = 436 [M+H$^+$].

Preparation of Fe(tpy)$_2$ complex on Si electrode

A silicon(111) wafer (B-doped, P-type, ≤ 0.005 Ωcm) was dipped into a Piranha solution at 120 °C for 10 minutes to form an oxidized surface, and stored in Milli-Q water. Just before use, the silicon substrate was dried by Ar flow, and cut in ca. 1.5 cm × 1.5 cm pieces. The hydrogen-terminated surface was prepared by the immersion into a 40 % NH$_4$F solution for 10 minutes at room temperature. The hydrogen-terminated substrate was immersed in a 1,4-dioxane solution containing 8 mM A^5, 0.08 mM Pd(P^{t}Bu$_3$)$_2$ and 0.31 M ^{i}Pr$_2$EtN, and refluxed for 3 hours under inert atmosphere. After the reaction, the substrate was ultrasonically rinsed by a 1 M 1,4-dioxane solution of PPh$_3$, 1,4-dioxane, ethanol and Milli-Q water for 5 minutes for the each step, and then dried by Ar blow. The modified substrate was immersed into a 0.1 M Fe(BF$_4$)$_2$ ethanol solution for 1 hour at room temperature, washed with Milli-Q and ethanol, and then dried. Finally, the immersion into a 0.1 mM chloroform solution of L gave the silicon substrate modified with Fe(tpy)$_2$ complex. The substrate was rinsed by chloroform, and dried by N$_2$ flow (Figure 3-2-1).

Preparation of reference sample

  The reference sample (Si-A^2) was prepared by the thermal hydrosilylation reaction. The pre-oxidized silicon(111) substrate (B-doped, P-type, $\leq$ 0.005 Ωcm) was dipped into a 40 % NH_4F solution for 10 minutes at room temperature. After rinse with Milli-Q water and drying with N_2, the substrate was immersed into a 1 mM toluene solution of A^2 and refluxed for 3 hours under an inert atmosphere. Then, the modified silicon was ultrasonically washed with toluene, ethanol and Milli-Q for 5 minutes sequentially, and dried by Ar blow.

X-ray photoelectron spectroscopy

  XPS measurements were performed with PHI5000 VersaProbe (ULVAC‐PHI) and a monochromatic Al Kα (100 W or 25 W) X-ray source. For the binding energy calibration, the peak of Si 2p for Si(0) was assigned at 99.2 eV.

Electrochemical measurement

  Cyclic voltammograms and chronoamperograms were collected by an ALS650DT electrochemical analyzer using an Ag^+/Ag reference electrode, a looped Pt counter electrode and modified silicon as a working electrode. In-Ga alloy was rubbed on a silicon surface, and copper plate was attached to establish ohmic junction. All measurements were performed in a 1 M TBAP dichloromethane solution in the dark to eliminate the photo irradiation effect at room temperature.

DFT calculation

  The simplified molecule (Si-A^5**Fetpy**) shown in Figure 3-2-2 was used to reduce the calculation cost. After the structure optimization by Gaussian 09 using B3LYP/TZVP level, the analytical frequency calculation was performed to confirm the termination of optimization. The solvation of dichloromethane was included using built-in package in Gaussian 09 in the estimation of molecular orbital and energy levels.
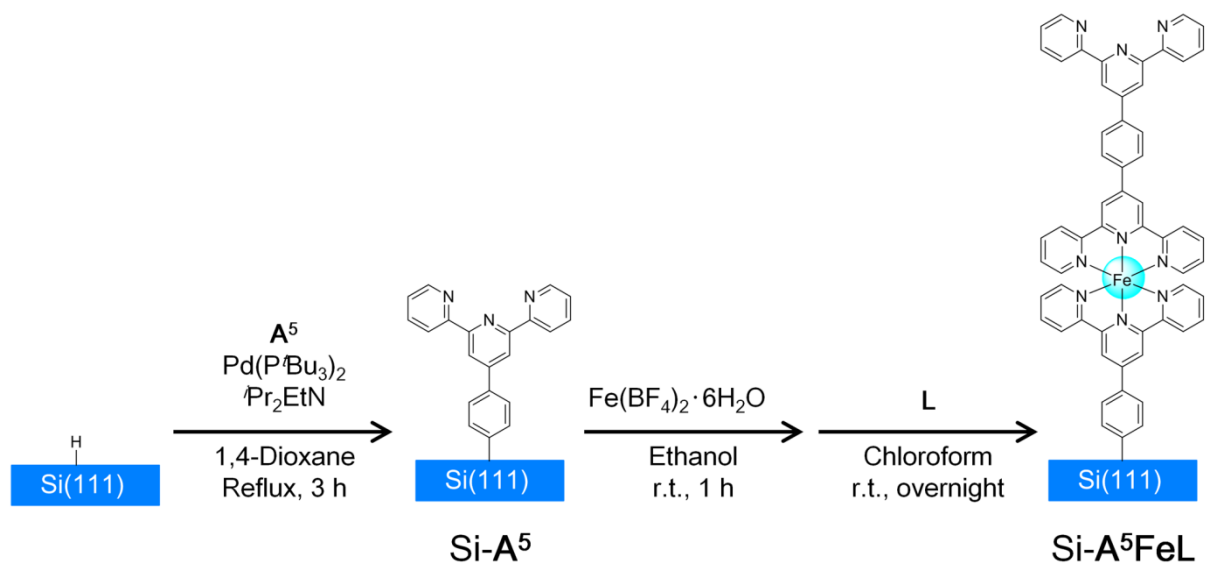
Figure 3-2-1. Stepwise fabrication process of Fe(tpy)$_2$ complex on hydrogen-terminated silicon(111) surface with anchor ligand **A^5**.
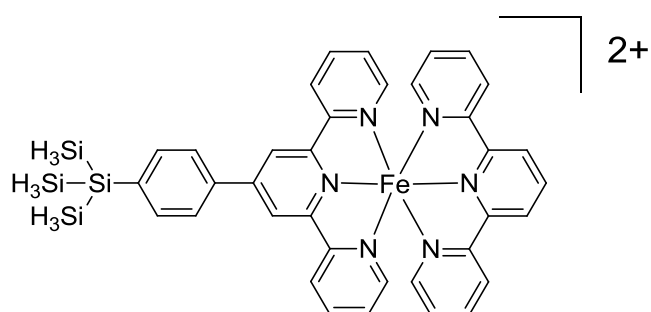

Figure 3-2-2. Simplified structure for DFT calculation (Si-**A^{5}Fetpy**).

3-3 Results

3-3-1 Surface modification of H-terminated Si(111) with 4-iodophenylterpyridine

2,2':6',2''-Terpyridine is known as a tridentate ligand having a high affinity to various metal ions [4]. During the surface modification process, the anchor ligand including terpyridine moiety ($\mathbf{A^5}$) and palladium ion coexist in a solution. Therefore, there is a possibility that a palladium ion is captured by a terpyridine moiety and the coordination of ferrous ion in the stepwise coordination process is prevented. In order to check the whether a metal-free terpyridine exists on the silicon surface, X-ray photoelectron spectra of the silicon substrate modified with $\mathbf{A^5}$ (Si-$\mathbf{A^5}$) were collected. As a reference surface, $\mathbf{A^2}$ was immobilized on silicon surface by hydrosilylation reaction without any metal catalyst (Si-$\mathbf{A^2}$).

Focusing on the N 1s region, the single peak derived from nitrogen atom in the terpyridine moiety is observed at 399.6 eV (Figure 3-3-1(A)). The binding energies for Pd^{2+}-coordinated terpyridine and metal-free terpyridine in SAM are reported as ca. 401.1 eV and ca. 399.5 eV respectively [5]. Hence, the binding energy of appeared peak suggests that terpyridine on surface is non-coordinating state. In addition, the observed peak position conforms to the N 1s peak for Si-$\mathbf{A^2}$. From these results, the terpyridine on silicon electrode connected by the Pd-catalyzed reaction exists as the metal-free state.

In P 2p region, one broad peak was observed around 134 eV (Figure 3-3-1(B)). However, the peaks derived from PPh_3 (130.6 eV) [6] and triphenylphosphine oxide (132.7 eV) [6] were not observed. Therefore, the significant amount of phosphine compound did not remain on the surface. It is considered that this broad peak is derived from the surface plasmon of single crystal silicon because the binding energy of this broad peak almost confirms the binding energy for plasmon peak of silicon [7] (Figure 3-3-1(C)).
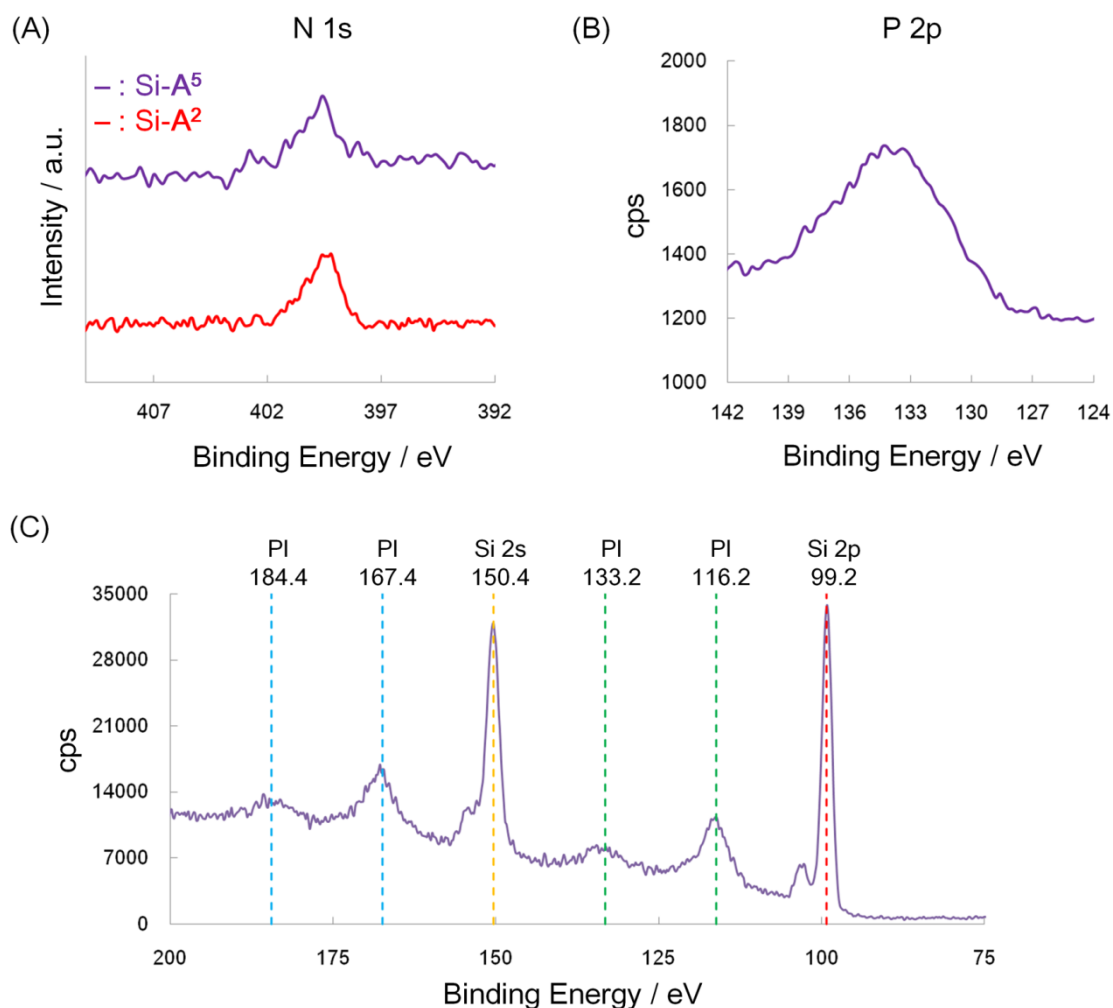
Figure 3-3-1. XP spectra of N 1s for Si-A^5 (purple solid line) and Si-A^2 (red solid line) (A), P 2p for Si-A^5 (B), and survey spectrum of Si 2p and Si 2s region of Si-A^5 **(C)**. Red dot line and orange dot line exhibit the main peak positions of Si 2p and Si 2s, respectively. The binding energies of plasmon peaks (Pl) (green dot line and blue dot line) were estimated by the following equation, $E_{Pl} = E_{main} + 17n$. Here, E_{Pl} is the binding energy of plasmon peak, E_{main} is the binding energy for main peak (Si 2p or Si 2s), and $n = 1, 2$. The small peak close to Si 2p derives from SiO_2. An XP spectrum of Si-A^2 was collected by a monochromatic Al Kα 25 W X-ray source.

3-3-2 Electrochemical evaluation of Fe(tpy)$_2$ complex on silicon

The cyclic voltammetry measurement was performed to estimate the surface coverage of Si-$\mathbf{A^5FeL}$. The reversible redox couple derived from [Fe(tpy)$_2$]$^{3+/2+}$ was shown at the 0.832 $\pm$ 0.003 V $vs.$ Ag$^+$/Ag (Figure 3-3-2(A)), and the proportional relationship between the peak current and the scan rate revealed that the redox wave comes from the surface confined species (Figure 3-3-2(B)). The estimated surface coverage values was $(4.0 \pm 1.2) \times 10^{-11}$ molcm^{-2}. This value is similar to those of Si-$\mathbf{A^xFeL}$ ($x = 1 - 4$), therefore Si-$\mathbf{A^5FeL}$ can also attend the discussion of the anchor ligand effect on the k_{ET} values.

The k_{ET} values were estimated by PSCA in accordance with the method described in Chapter 2. Both of oxidation and reduction current exhibited the dependency on the overpotential in chronoamperograms. In addition, the linear decay depending on the overpotential was observed in the ln $I - t$ plots (Figure 3-3-3). Hence, the k_{ET} values were estimated from the slope in ln $I - t$ plots. The Tafel plot (ln $k_{ET} - \eta$ plot) for Si-$\mathbf{A^xFeL}$ ($x = 1, 2, 4,$ and 5) is shown in Figure 3-3-4. The Si-$\mathbf{A^5FeL}$ gave the greater k_{ET} value that of Si-$\mathbf{A^1FeL}$. The almost same k_{ET} value as those of Si-$\mathbf{A^2FeL}$ and Si-$\mathbf{A^4FeL}$ indicates the superior electron transfer kinetics. This result suggests that a phenylene bridge directly immobilized on silicon surface has the higher electron transport ability than a vinylene bridge formed by hydrosilylation reaction. In order to investigate the contribution of phenylene unit, DFT calculation was performed.
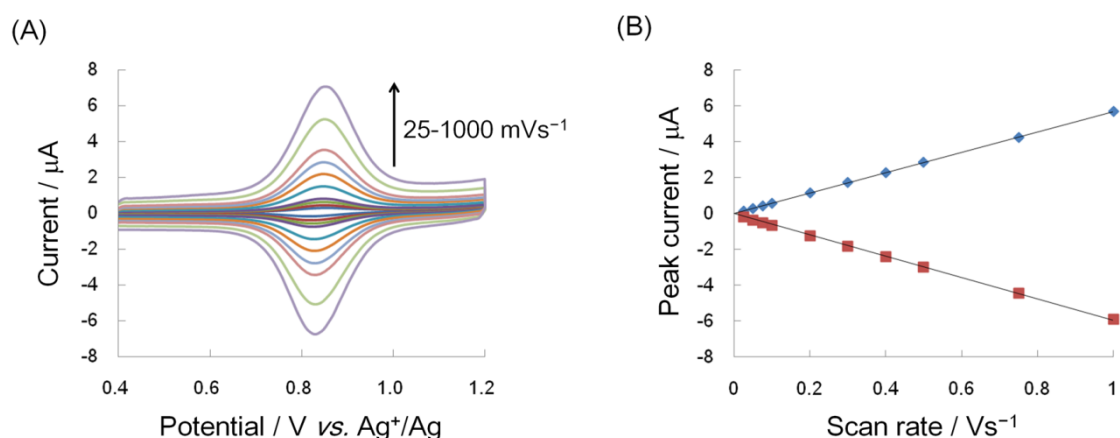
Figure 3-3-2. Cyclic voltammograms for Si-$\mathbf{A^5FeL}$ in a 1 M Bu$_4$NClO$_4$/CH$_2$Cl$_2$ solution in the dark (A), and the dependency of peak current on scan rate (B).
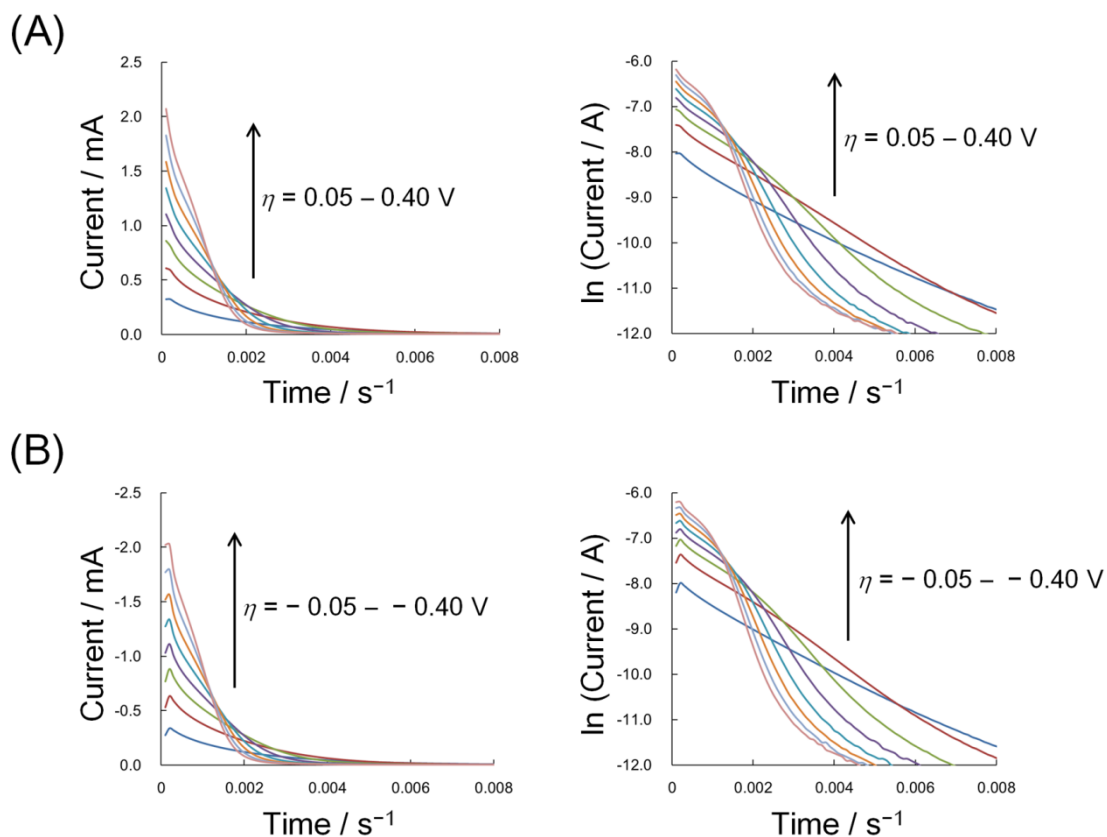
Figure 3-3-3. Chronoamperograms and ln $I - t$ plots of oxidation current (A) and reduction current (B) for Si-$\mathbf{A^5FeL}$ in a 1 M Bu$_4$NClO$_4$/CH$_2$Cl$_2$ solution in the dark.
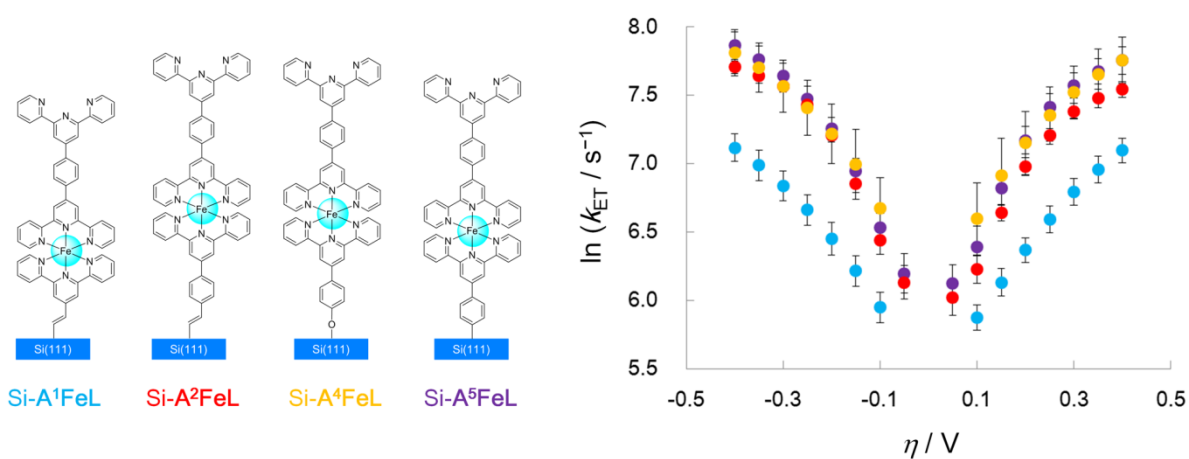
Figure 3-3-4. Tafel plots for Si-$\mathbf{A^1FeL}$ (blue circles), Si-$\mathbf{A^2FeL}$ (red circles), Si-$\mathbf{A^4FeL}$ (orange circles), and Si-$\mathbf{A^5FeL}$ (purple circles).

3-3-3 DFT calculation

The molecular orbitals of Si-A^5**Fetpy** were calculated by DFT calculation (B3LYP/TZVP level), and HOMO−3 level has the delocalized orbital spread from iron center to silicon atom (Figure 3-3-5). Hence, it is expected that this orbital also contribute to make the strong electronic coupling and promote the electron transport behavior. The estimated energy difference between HOMO and HOMO−3 (ΔE) is 0.45 eV, and its value is also close to the ΔE values for Si-A^2**Fetpy** (0.44 eV) and Si-A^4**Fetpy** (0.52 eV). The orbital energy comparison between Si-A^1**Fetpy** and Si-A^5**Fetpy** is the most important to investigate the effect of the directly bonded Si-aryl system. The orbital structures of Si-A^1**Fetpy** and Si-A^5**Fetpy** are similar, and the HOMO, HOMO−1 and HOMO−2 levels derived from t_{2g} of Fe 3d orbitals are constant. However, the energy levels of HOMO−3 derived from anchor molecules are drastically different. The HOMO−3 level of Si-A^5**Fetpy** were risen by the exchange of anchor unit structure from vinylene to phenylene which makes the expansion of π-conjugation. Therefore, the ΔE value decreased from 0.63 eV for Si-A^1**Fetpy** to 0.45 eV for Si-A^5**Fetpy** (Figure 3-3-5 and Table 3-3-1). It produces the stronger electron coupling between iron center and silicon mediating the hole superexchange. From this result, we can expect that the phenylene moiety immobilized directly on silicon is more suitable as an anchor ligand for the effective electron transport than a vinylene-bridged anchor moiety.
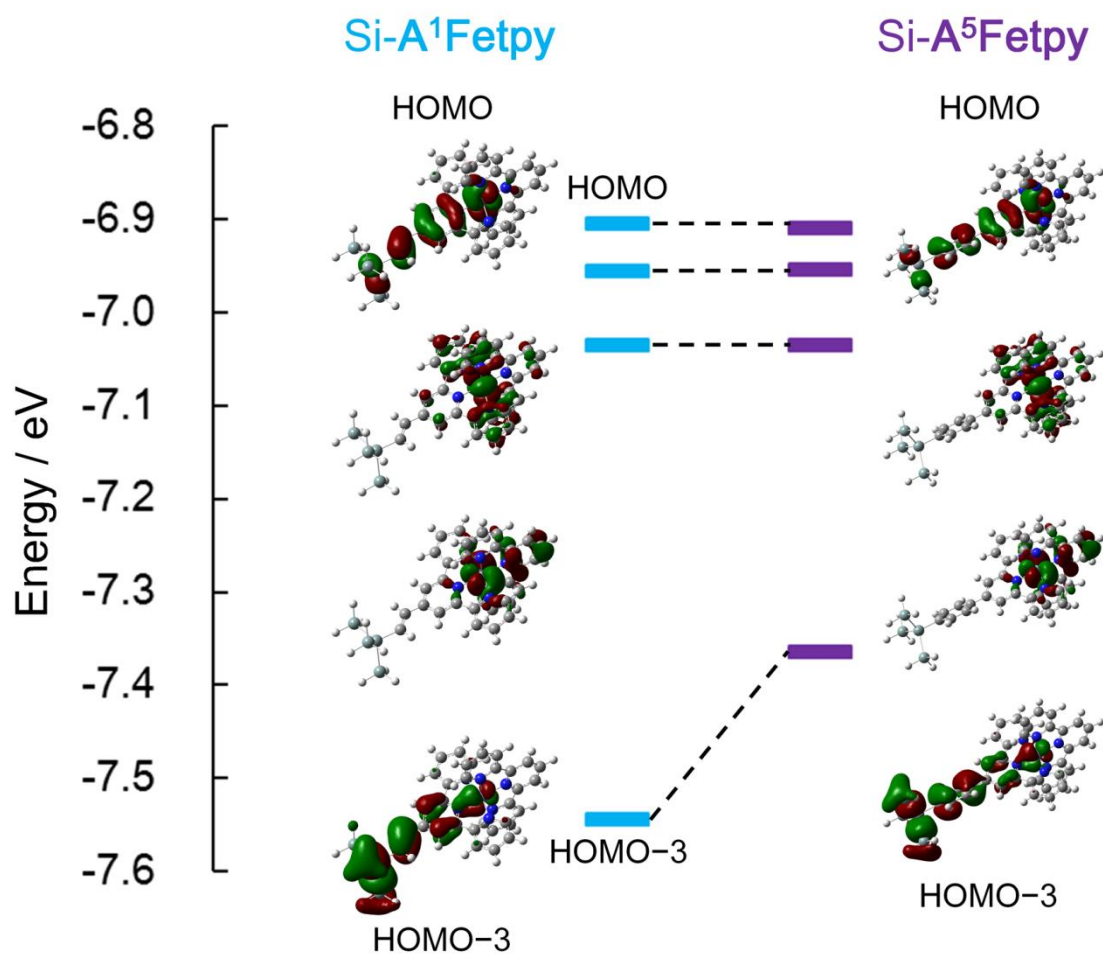
Figure 3-3-5. Energy levels and molecular orbitals for Si-**A**[1]**Fetpy** and Si-**A**[5]**Fetpy**.

Table 3-3-1. Energy levels of HOMO, HOMO−1, HOMO−2, HOMO−3 and ΔE values for Si-**A**[1]**Fetpy** and Si-**A**[5]**Fetpy**. $\Delta E = E_{HOMO} - E_{HOMO-3}$

	Si-A¹Fetpy	Si-A⁵Fetpy
HOMO	− 6.91 eV	− 6.91 eV
HOMO−1	− 6.96 eV	− 6.95 eV
HOMO−2	− 7.04 eV	− 7.04 eV
HOMO−3	− 7.54 eV	− 7.36 eV
ΔE	0.63 eV	0.45 eV

3-4 Conclusion

The Fe(tpy)$_2$ complex was constructed on a hydrogen-terminated silicon surface by the stepwise coordination method and the Pd-catalyzed Si-aryl bond formation reaction developed in our laboratory. The terpyridine-terminated surface was evaluated by XPS, and revealed that the terpyridine moiety is the metal-free state and it can work as the coordination cite for the sequential complexation process. The Si-**A^{5}FeL** showed the reversible redox couple derived from [Fe(tpy)$_2$]$^{3+/2+}$, and its k_{ET} value was greater than that of Si-**A^{1}FeL** but almost same with Si-**A^{2}FeL** and Si-**A^{4}FeL**. The energy level comparison between Si-**A^{1}FeL** and Si-**A^{5}FeL** by DFT calculation indicated that the expansion of π-conjugation by the exchange of the bridging moiety structure in anchor ligands from vinylene to phenylene raise the HOMO-3 level, and decreased the ΔE value contributing to the promotion of the greater k_{ET} value by the stronger electronic coupling. This result suggests that the directly immobilized arene moiety on silicon can work as a more suitable junction for the superior electron transport system than the vinylene bridge formed by hydrosilylation method.

3-5 References

1. a) Yamanoi, Y. *J. Org. Chem.* **2005**, *70*, 9607-9609. b) Yamanoi, Y.; Nishihara, H. *Tetrahedron Lett.* **2006**, *47*, 7157-7161. c) Yamanoi, Y.; Taira, T.; Sato, J.; Nakamula, I.; Nishihara, H. *Org. Lett.* **2007**, *9*, 4543-4546. d) Yamanoi, Y.; Nishihara, H. *J. Org. Chem.* **2008**, *73*, 6671-6678. e) Yamanoi, Y.; Nishihara, H. *J. Synth. Org. Chem. Jpn.* **2009**, *67*, 778-786. f) Yabusaki, Y.; Ohshima, N.; Kondo, H.; Kusamoto, T.; Yamanoi, Y.; Nishihara, H. *Chem. Eur. J.* **2010**, *16*, 5581-5585. g) Lesbani, A.; Kondo, H.; Yabusaki, Y.; Nakai, M.; Yamanoi, Y.; Nishihara, H. *Chem. Eur. J.* **2010**, *16*, 13519-13527. h) Lesbani, A.; Kondo, H.; Sato, J.-i.; Yamanoi, Y.; Nishihara, H.; *Chem. Commun.* **2010**, *46*, 7784-7786.

2. Yamanoi, Y.; Sendo, J.; Kobayashi, T.; Maeda, H.; Yabusaki, Y.; Miyachi, M.; Sakamoto, R.; Nishihara, H. *J. Am. Chem. Soc.* **2012**, *134*, 20433-20439.

3. Alemán, E.; Shreiner, C. D.; Rajesh, C. S.; Smith, T.; Garrison, S. A.; Modarelli, D. A. *Dalton Trans.* **2009**, 6562-6577.

4. a) Andres, P. R.; Schubert, U. S. *Adv. Mater.* **2004**, *16*, 1043-1068. b) Winter, A.; Hager, M. D.; Newkome, G. R.; Schubert, U. S. *Adv. Mater.* **2011**, *23*, 5728-5748. c) Eryazici, I.; Moorefield, C. N.; Newkome, G. R. *Chem. Rev.* **2008**, *108*, 1834-1895. d) Schubert, U. S.; Eschbaumer, C.; Andres, P.; Hofmeier, H.; Weidl, C. H.; Herdtweck, E.; Dulkeith, E.; Moreani, A.; Hecker, N. E.; Feldmann, J. *Synthetic Met.* **2001**, *121*, 1249-1252.

5. a) Traulsen, C. H.-H.; Darlatt, E.; Richter, S.; Poppenberg, J.; Hoof, S.; Unger, W. E. S.; Schalley, C. A. *Langmuir* **2012**, *28*, 10755-10763. b) Fernandes, A. E.; Devillez, S.; d'Haese, C.; Deumer, G.; Haufroid, V.; Nysten, B.; Riant, O.; Jonas, A. M. *Langmuir* **2012**, *28*, 14822-14828.

6. Pelavin, M.; Hendrickson, D. N., Hollander, J. M.; Jolly, W. L. *J. Phys. Chem.* **1970**, *74*, 1116-1121.

7. 社団法人　日本表面化学会　編, *表面分析技術選書　X 線光電子分光法*, 丸善株式会社, **1998**.

Chapter 4

Electron transport behavior of Fe(tpy)$_2$ wire on silicon electrode

4-1 Introduction

The knowledge about the electron transport mechanism in molecular wire will be required for the design of effective electron transfer system in molecular devices. Our group has constructed linear and dendritic bis(terpyridine)iron complex oligomer wires on gold electrode, and unveiled their electron transfer mechanism by the numerical analysis of the current decay in chronoamperograms [1]. The electrons are transported by the sequential hopping between the neighboring metal complex units in a wire, and this mechanism contributes to the superior long-range electron transport ability and the characteristic asymmetry current decay of terminal redox active moiety. In addition, we reported that the ferrocene moiety introduced at the dendritic metal complex wires showed the unsymmetric oxidation and reduction current decay, and clarified its behavior using the sequential electron hopping model [2] (Figure 4-1-1).

However, most of present electronic devices are composed of semiconductors. Therefore, the analysis of electron transport behavior for molecules on semiconductors has an important role of molecular electronics. Especially, silicon is the major material in the electronics field, and it has often been chosen as a substrate of SAMs to evaluate their redox behaviors and conductive properties. The redox active SAMs on silicon sometimes show the different electrochemical behaviors from those of SAMs on metallic substrate. For instance, p-type redox active species such as ferrocene, whose HOMO levels are observed in cyclic voltammetry, confined on n-type silicon is strongly affected by the specification of substrate and photoirradiation [3]. In the dark, samples on lowly-doped silicon give no redox wave or only show the cathodic wave while the light-illuminated samples exhibit the reversible redox wave with the negative shift of redox potential. On the other hand, samples on p-type silicon and highly-doped n-type silicon exhibit the similar redox behavior like SAMs on metal electrodes [4]. When an n-type species such as methyl viologen is confined on silicon electrode in order to observe their LUMO levels, the inversion phenomenon is observed. Wrighton and coworkers modified silicon surface with *N,N'*-dialkyl-4,4'-bipyridinium polymer and reported its redox behavior [5]. On n-type silicon, its reversible redox behavior was similar with that on Pt electrode. However, on p-type silicon, no cathodic peak was observed while the redox wave appeared with the positive potential shift under light illumination. However, there are some reports of n-type molecules on n-type silicon which did not exhibit the reversible redox wave [6]. At the current moment, although it is difficult to explain their redox behavior perfectly, the band gap of silicon is the key of these characteristic behaviors.

When silicon is used as an electrode for Fe(tpy)$_2$ wires, it is expected that their electron transport from the terminal redox active moiety will be affected by the band structure of

silicon. In this chapter, the multilayered $Fe(tpy)_2$ wires were constructed on hydrogen-terminated p-type silicon electrode, and two types of redox active molecules having different redox potentials were introduced at the termini of wires to investigate the electron transport behavior of $Fe(tpy)_2$ wires by cyclic voltammetry (Figure 4-1-2). From the collected voltammograms, the electron transport mechanism was elucidated.
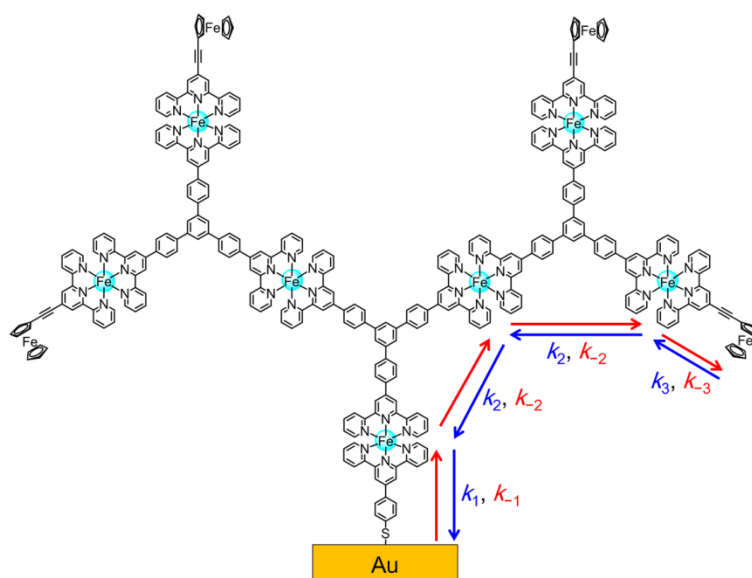

Figure 4-1-1. Sequential hopping electron transport model for $Fe(tpy)_2$ wire including terminal ferrocene. The rate constants for each step are denoted as $k_{\pm l}$ ($l = 1 - 3$). $k_{\pm 1}$: electron transfer between electrode and $Fe(tpy)_2$, $k_{\pm 2}$: second-order electron self-exchange rate constant between the neighboring $Fe(tpy)_2$ units, $k_{\pm 3}$: electron transfer between ferrocene and $Fe(tpy)_2$.
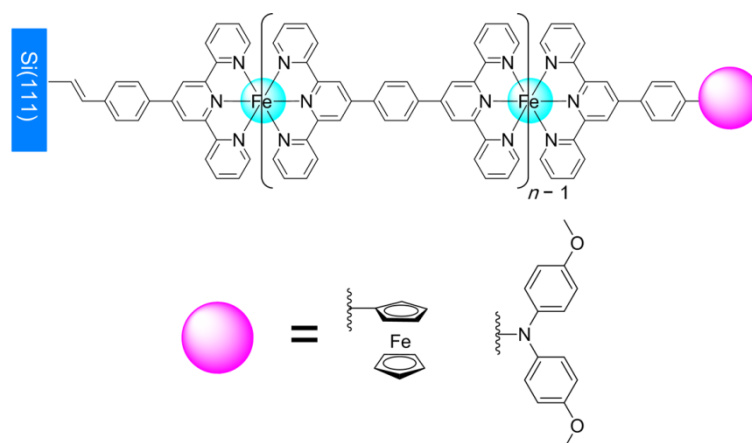
Figure 4-1-2. Structure of $Fe(tpy)_2$ wire described in this chapter.

4-2 Experimental section

General

4'-[4-(Ferrocenyl)phenyl]- 2,2':6',2''-terpyridine (T^1) [7] and 4-iodophenylferrocene [8] were synthesized in our laboratory according to the literature. Other compounds and solvents are described in the experimental section of Chapter 2.

Synthesis of T^2

4'-[4-(*N*,*N*-Di-*p*-anisylamino)phenyl]-2,2':6',2''-terpyridine (T^2) was synthesized by the modified method of reference 9. 4'-[4-Aminophenyl]- 2,2':6',2''-terpyridine was used as a reagent instead of aniline. The compound was obtained as a brown powder. 93.6 mg (35 %) ^{1}H NMR (400 M Hz, CDCl$_3$) δ (ppm): 8.72 (d, *J* = 3.9 Hz, 2H), 8.68 (s, 2H), 8.66 (d, *J* = 8.0 Hz, 2H), 7.87 (td, *J* = 7.8 Hz, 2.0 Hz, 2H), 7.74 (d, *J* = 8.8 Hz, 2H), 7.34 (ddd, *J* = 7.6 Hz, 4.6 Hz, 0.8 Hz, 2H), 7.11 (d, *J* = 8.8 Hz, 4H), 7.02 (d, *J* = 8.8 Hz, 2H), 6.87 (d, *J* = 8.8 Hz, 4H), 3.82 (s, 6H). FAB-MS *m/z* = 537 [M+H$^+$].

Synthesis of 4-ferrocenylphenol

4-Ferrocenylphenol was synthesized according to the literature [10]. The compound was obtained as an orange powder. 470 mg (17 %). ^{1}H NMR (400 MHz, CDCl$_3$) δ (ppm): 7.36 (d, *J* = 8.8 Hz, 2H), 6.77 (d, *J* = 8.8 Hz, 2H), 4.63 (s, 1H), 4.56 (t, *J* = 2.0 Hz, 2H), 4.26 (t, *J* = 1.8 Hz, 2H), 4.04 (s, 5H).

Preparation of Fe(tpy)$_2$ multilayers

A silicon(111) wafer (B-doped, P-type, ≤ 0.005 Ωcm) treated with Piranha solution was cut in ca. 1.5 cm × 1.5 cm pieces, and immersed in a 40 % NH$_4$F solution for 10 minutes at room temperature to prepare hydrogen-terminated surface. The activated Si substrates were dipped in a 1 mM toluene solution of 4'-(4-Ethynylphenyl)-2,2':6',2''-terpyridine (A^2), and refluxed for 1 h under an inert atmosphere. After the reaction, the modified substrates were ultrasonically rinsed with toluene, ethanol and Milli-Q water for 5 minutes each, and then dried by N$_2$ blow. The substrates were immersed in a 0.1 M Fe(BF$_4$)$_2$·6H$_2$O ethanol solution for 1 hour at room temperature, washed with Milli-Q and ethanol sequentially, and dried by N$_2$ blow. The iron-terminated substrates were immersed in a 0.1 mM chloroform solution of **L** at room temperature for overnight, rinsed with chloroform, and dried by N$_2$ blow. These two processes (dipping in a Fe^{2+} ion solution and an **L** solution) were repeated for *n*−1 times. After the repeat of coordination cycles, the substrates were dipped in 0.1 M Fe(BF$_4$)$_2$·6H$_2$O ethanol solution for 1 hour at room temperature. After rinsing and drying, the substrates were

immersed in a chloroform solution of a terminal ligand (T^1 or T^2) for overnight at room temperature, washed with chloroform and dried by N_2 blow (Figure 4-2-1).

Preparation of reference samples

  As reference samples, ferrocene SAMs (Si-**C_6H_4Fc** and Si-**OC_6H_4Fc**) were prepared in accordance with the following process. A pre-treated silicon(111) substrate was hydrogen-terminated by the immersion into a 40% NH_4F solution. In order to prepare Si-**C_6H_4Fc**, the substrate was washed with water and dried, then immersed in a 1,4-dioxane solution containing 8 mM 4-iodophenylferrocene, 0.08 mM Pd(P^{t}Bu$_3$)$_2$, and 0.31 M diisopropylethylamine. The substrate was refluxed for 20 hours under an inert atmosphere. The modified silicon was ultrasonically rinsed with 1,4-dioxane, ethanol and water for 5 minutes each, and then dried by N_2 blow (Figure 4-2-2(A)). For Si-**OC_6H_4Fc** preparation, the hydrogen-terminated silicon was immersed and refluxed in a 1 mM 1,4-dioxane solution of 4-ferrocenylphenol for 20 hours under an inert atmosphere. After reaction, the substrate was rinsed using the same process for Si-**C_6H_4Fc** (Figure 4-2-2(B)).

Electrochemical measurement

  Electrochemical measurement was performed by ALS electrochemical analyzers. An Ag$^+$/Ag reference electrode, a looped Pt counter electrode and a modified silicon substrate as a working electrode were used. In-Ga alloy was rubbed on a silicon substrate to make an ohmic contact between silicon and a copper plate. All data were collected in a 1 M Bu$_4$NClO$_4$/CH$_2$Cl$_2$ solution under dark condition.

  The redox potential of ferrocene was measured using a glassy carbon as a working electrode, an Ag$^+$/Ag reference electrode and a rolled Pt counter electrode with a tailor-made cell. The redox potential was defined as an average value of the oxidation peak potential and the reduction peak potential, and calculated at 0.13 V *vs.* Ag$^+$/Ag in a 1 M Bu$_4$NClO$_4$/CH$_2$Cl$_2$ solution at room temperature.
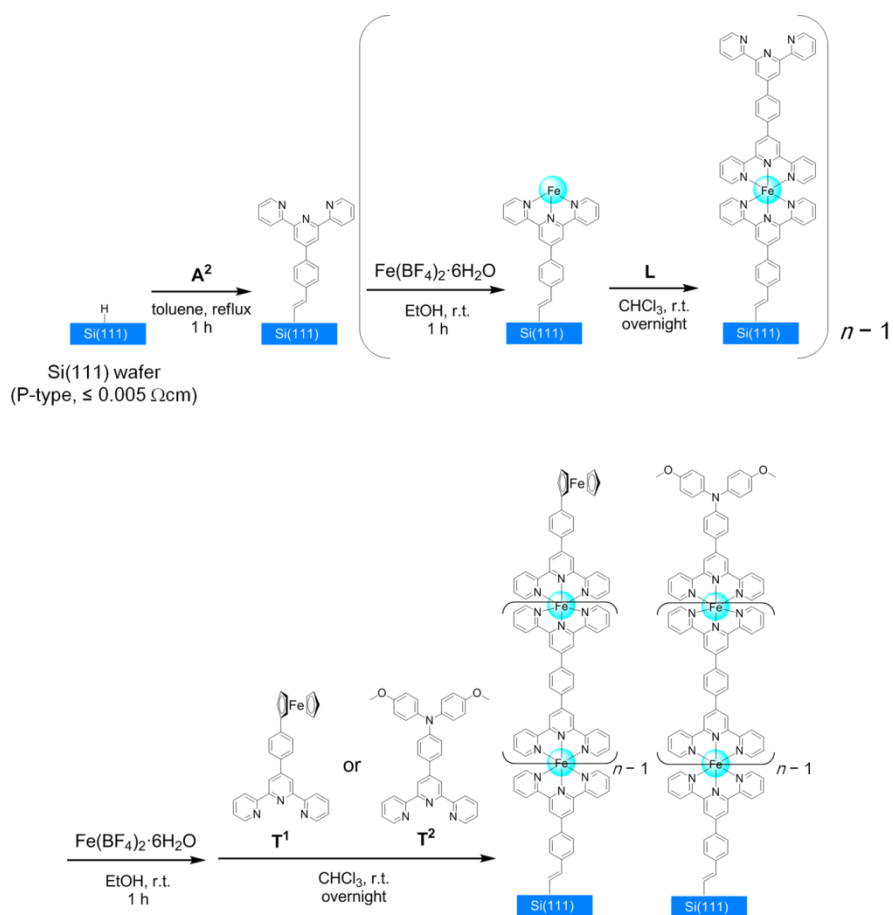
Figure 4-2-1. Preparation process of Fe(tpy)$_2$ multilayer wires on a hydrogen-terminated silicon.
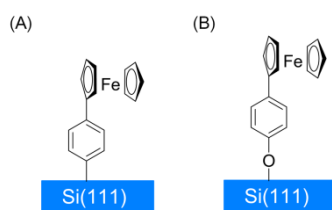
Figure 4-2-2. Structures of Si-**C$_6$H$_4$Fc** (A) and Si-**OC$_6$H$_4$Fc** (B).

4-3 Fabrication of Fe(tpy)$_2$ wires on hydrogen-terminated silicon

4-3-1 T^1-terminated wire

  The T^1-terminated wires (Si-A^2(FeL)$_{n-1}$FeT^1, $n = 1 - 3$) were prepared on H-terminated silicon(111) surfaces by the stepwise coordination method. The cyclic voltammograms (CVs) were collected to evaluate the surface coverage values and the electron transport properties of Fe(tpy)$_2$ complex wires on silicon electrodes. In CVs for Si-A^2(FeL)$_{n-1}$FeT^1, the reversible redox couples derived from [Fe(tpy)$_2$]$^{3+/2+}$ were observed, and the peak currents (I_p) were proportional to the scan rates (v). This linear relation suggests that these redox waves come from the surface-confined species (Figure 4-3-1). The estimated surface coverage values (Γ) increasing with the number of layers indicated Fe(tpy)$_2$ wire was elongated layer-by-layer (Figure 4-3-2). Focusing on the redox behavior of T^1, the large separation between the oxidation peak and reduction peak was observed with increase of the scan rate. In addition, the peak shape became broader and unclear with increasing the number of the layer. These redox behaviors suggest that the electron transport from T^1 is slow. The peak current and scan rate did not show the proportional relation, and a part of peak currents could not be estimated from the CVs collected at the high scan rates due to the unclear redox wave. Therefore, the Γ value for T^1 was estimated from the CV recorded at a scan rate of 25 mVs^{-1} because it is expected that the voltammogram collected at a slow scan rate gives the most closest value comparing with the actual Γ value. Although the immobilization of T^1 cannot be confirmed from the $I_p - v$ plot, the fabrication of target structures is advocated by two results. One is the growth of Fe(tpy)$_2$ surface coverage values. The other is the constant surface coverage values of T^1 in each layer. If T^1 was not introduced at the top of the wires, the Γ values of Fe(tpy)$_2$ cannot increase. In addition, the 1-layer samples will not exhibit the redox wave derived from Fe(tpy)$_2$ complex because they cannot form Fe(tpy)$_2$ complex without the introduction of T^1. In addition, if T^1 is taken into the wires randomly, T^1 will show various Γ values or the larger values than the expected values (1/n times of the Γ value for Fe(tpy)$_2$).

  This characteristic ferrocene redox behavior has been only observed in the Fe(tpy)$_2$ system on silicon electrode. The CV measurements for Fe(tpy)$_2$ wires on gold electrode including the same bridging ligand and terminal ligand (T^1) exhibited the reversible redox wave even at the fast scan rate and at the top of the long wires [11]. And, the ferrocenyl group immobilized on the same specification p-type silicon(111) electrode via Si-C bond (Si-C$_6$H$_4$Fc) or Si-O-C bond (Si-OC$_6$H$_4$Fc) whose electron transport occurs by the superexchange mechanism also showed the reversible redox wave and the linear relation between I_p and v (Figure 4-3-3). These results suggest that this reversible redox wave derives from the surface confined

species, and the electron transport between electrode and ferrocene moiety is significantly rapid within the measured scan rate. In addition, ferrocene moieties immobilized on p-type silicon surface via various molecular wires have exhibited the reversible redox wave [12]. From these instances, it is considered that both of the electronic property of silicon electrode and the sequential hopping electron transport contribute to the observed characteristic electrochemical response.
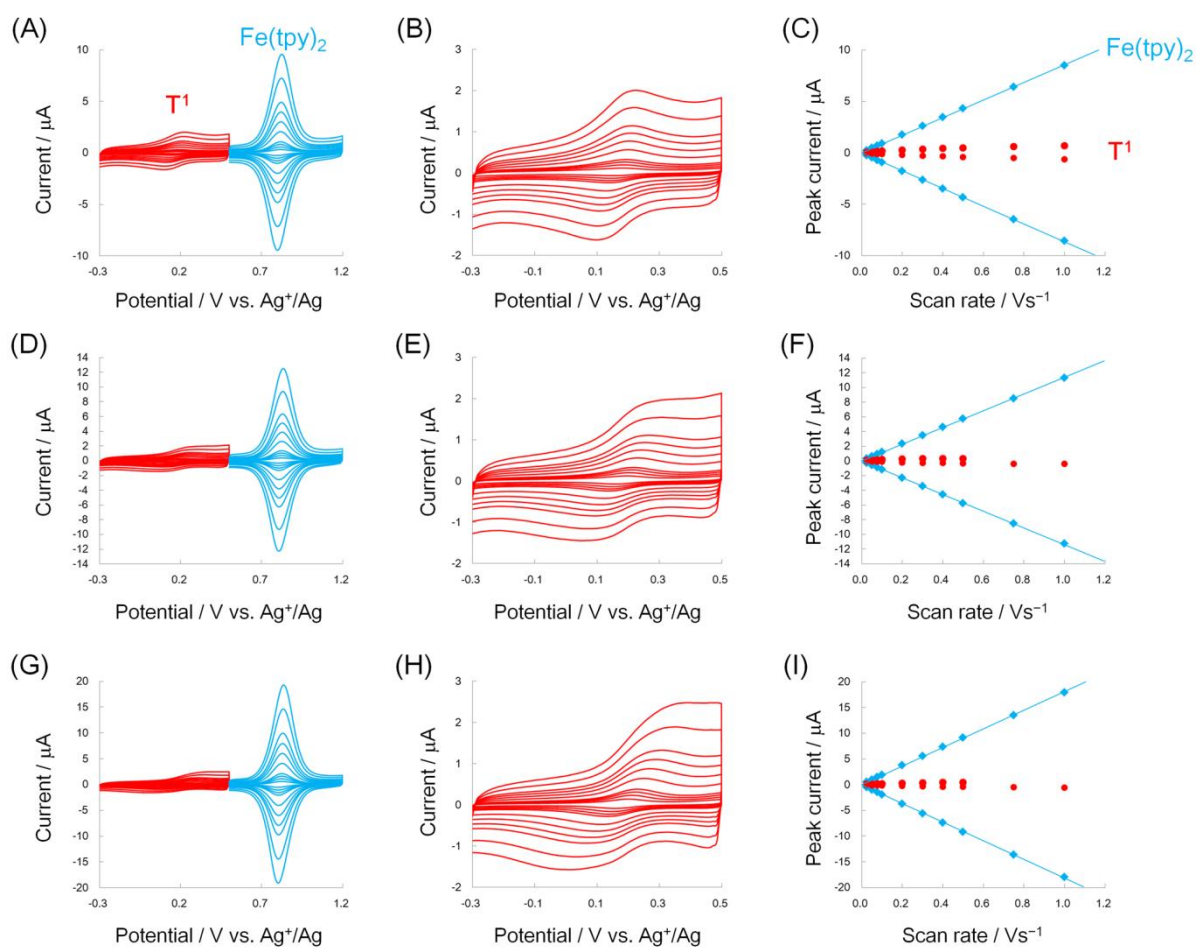

Figure 4-3-1. Cyclic voltammograms for Si-A^2FeT^1 (A), Si-$A^2(FeL)_1FeT^1$ (D), and Si-$A^2(FeL)_2FeT^1$ (G), enlarged cyclic voltammograms of T^1 in Si-A^2FeT^1 (B), Si-$A^2(FeL)_1FeT^1$ (E), and Si-$A^2(FeL)_2FeT^1$ (F), and I_p - ν plots for Si-A^2FeT^1 (C), Si-$A^2(FeL)_1FeT^1$ (F), and Si-$A^2(FeL)_2FeT^1$ (I).
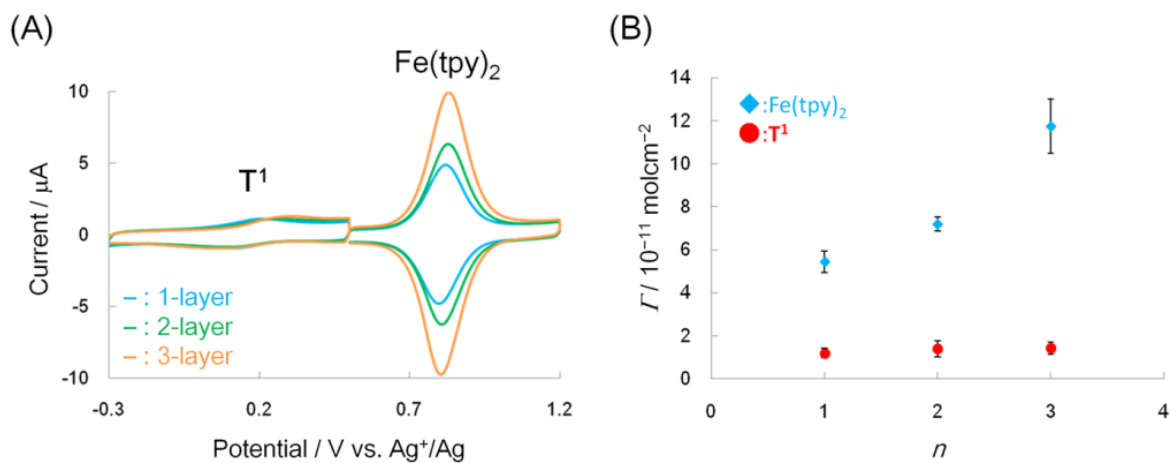
Figure 4-3-2. Cyclic voltammograms for Si-$\mathbf{A^2(FeL)_{n-1}FeT^1}$ at a scan rate of 500 mVs^{-1} (A), and the surface coverage values of Si-$\mathbf{A^2(FeL)_{n-1}FeT^1}$ (B).
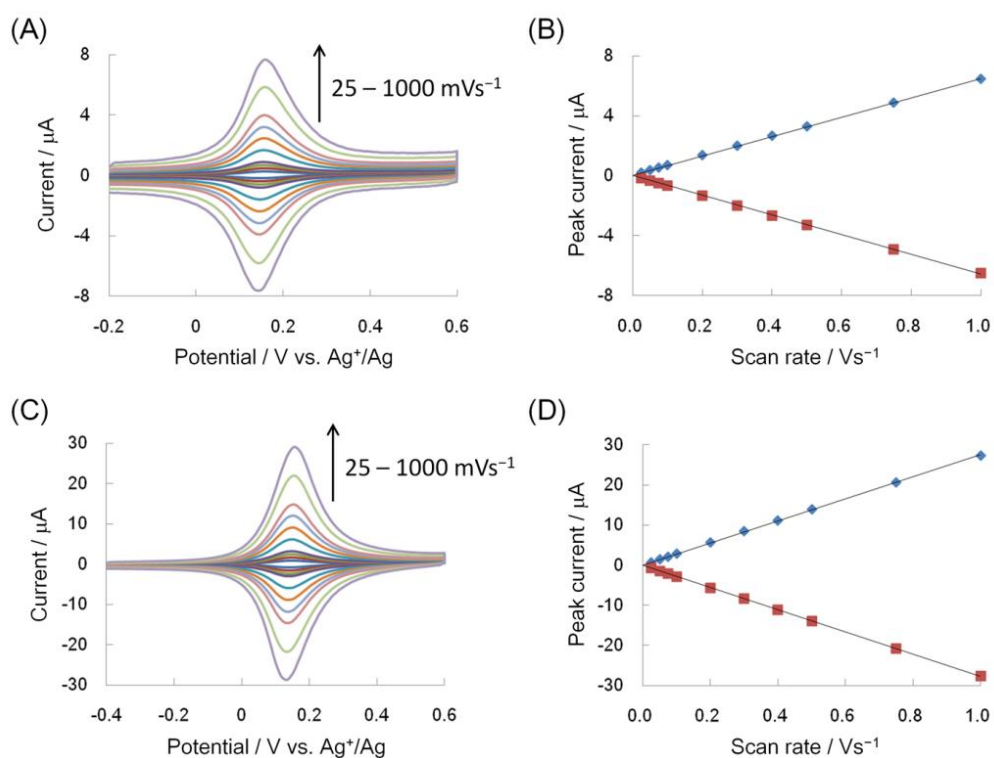
Figure 4-3-3. Representative cyclic voltammograms recorded at scan rates of 25 to 1000 mVs^{-1} for Si-$\mathbf{C_6H_4Fc}$ ($\Gamma = (4.3 \pm 0.9) \times 10^{-11}$ molcm^{-2}) (A) and Si-$\mathbf{OC_6H_4Fc}$ ($\Gamma = (2.0 \pm 0.4) \times 10^{-10}$ molcm^{-2}) (C), and the relation between peak current and scan rate for Si-$\mathbf{C_6H_4Fc}$ (B) and Si-$\mathbf{OC_6H_4Fc}$ (D).

4-3-2 T^2-terminated wire

The T^2-terminated wires (Si-A^2(FeL)$_{n-1}$FeT^2, $n = 1 - 4$) were fabricated on the silicon substrates by the sequential complexation process. In order to estimate surface coverage values and evaluate electron transport behavior, CV measurements were performed. Up to $n = 3$, both of Fe(tpy)$_2$ complex and T^2 showed the reversible redox waves, and the linear relationships of the peak currents and the scan rates for Fe(tpy)$_2$ and T^2 suggest the T^2-terminated wires were confined on H-terminated silicon substrates. The 4-layered sample showed the linear dependency of peak current on scan rate for [Fe(tpy)$_2$]$^{3+/2+}$ redox couple and the oxidation peak of T^2 while the cathodic peak of T^2 strayed from the linear relation in the high scan rate region (Figure 4-3-4). Focusing on the redox peak of T^2 in Si-A^2(FeL)$_3$FeT^2, the anodic peak and cathodic peak showed the asymmetric shape and its peak current ratio (I_{pa}/I_{pc}) of anodic peak current (I_{pa}) and cathodic peak current (I_{pc}) is 1.4 at a scan rate of 1000 mVs^{-1}. Ideally, a surface-confined reversible redox moiety gives the symmetric redox wave and the $I_{pa}/I_{pc} = 1$. In the cyclic voltammograms for Si-A^2(FeL)$_{n-1}$FeT^2 collected at a scan rate of 1000 mVs^{-1}, the symmetric redox waves were observed up to $n = 3$. In addition, the I_{pa}/I_{pc} values were 1.1 for $n = 1$ and 2, and 1.2 for $n = 3$ (Figure 4-3-5). It is considered that this decrease of reversibility for the 4-layered wire occurred by the charge trapping phenomenon [13]. This result suggests that T^2 was introduced at the top of multilayered Fe(tpy)$_2$ wire and the electron from T^2 is transported via the metal complex wire. However, the effect of the charge trapping is not significant strong in the case of Si-A^2(FeL)$_3$FeT^2 because the cyclic voltammograms at a scan rate of 1000 mVs^{-1} collected by the consecutive potential scan did not show a significant change (Figure 4-3-6). It means that all of the oxidized species were reduced within the scanned potential range.

The surface coverage values of Fe(tpy)$_2$ complex increased linearly while those of T^2 give the almost constant values (Figure 4-3-7). This series of results suggests that the linear growth of Fe(tpy)$_2$ complex wires and the introduction of T^2 at the tip of the wires. From the above results, the construction of target T^2-terminated Fe(tpy)$_2$ wires was confirmed.
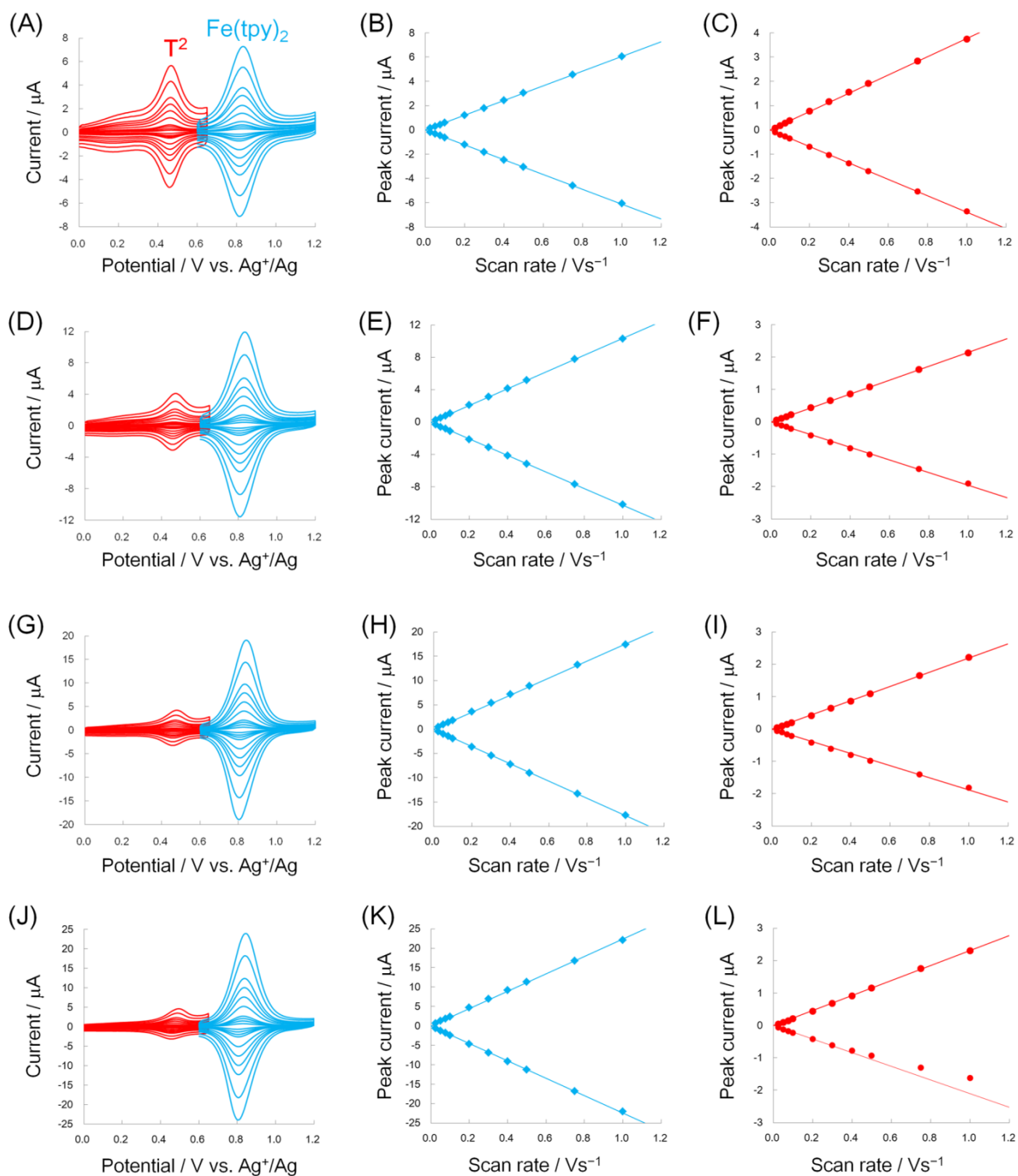
Figure 4-3-4. Cyclic voltammograms for Si-$\mathbf{A^2FeT^2}$ (A), Si-$\mathbf{A^2(FeL)_1FeT^2}$ (D), Si-$\mathbf{A^2(FeL)_2FeT^2}$ (G), and Si-$\mathbf{A^2(FeL)_3FeT^2}$ (J), $I_\mathrm{p} - v$ plots of [Fe(tpy)$_2$]$^{3+/2+}$ redox couple for Si-$\mathbf{A^2FeT^2}$ (B), Si-$\mathbf{A^2(FeL)_1FeT^2}$ (E), Si-$\mathbf{A^2(FeL)_2FeT^2}$ (H), and Si-$\mathbf{A^2(FeL)_3FeT^2}$ (K), and $I_\mathrm{p} - v$ plots of $\mathbf{T^2}$ for Si-$\mathbf{A^2FeT^2}$ (C), Si-$\mathbf{A^2(FeL)_1FeT^2}$ (F), Si-$\mathbf{A^2(FeL)_2FeT^2}$ (I), and Si-$\mathbf{A^2(FeL)_3FeT^2}$ (L).
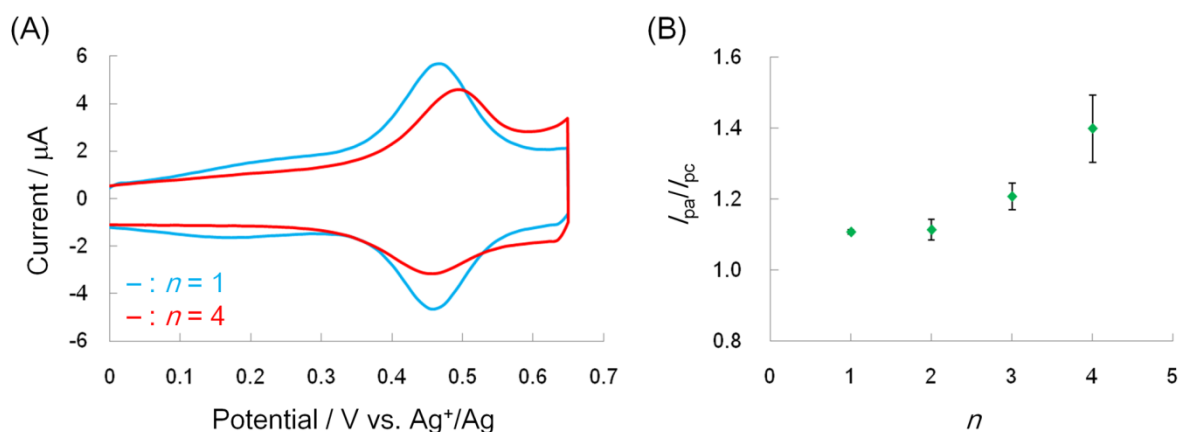
Figure 4-3-5. (A) Cyclic voltammograms for $\mathbf{T^2}$ in Si-$\mathbf{A^2FeT^2}$ (blue solid line) and in Si-$\mathbf{A^2(FeL)_3FeT^2}$ (red solid line) at a scan rate of 1000 mVs^{-1}, and (B) dependency of I_{pa}/I_{pc} ratio on the number of layer, n.
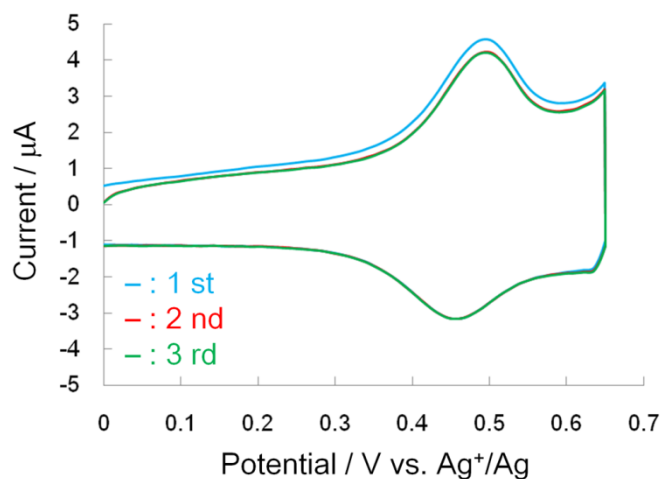
Figure 4-3-6. (A) The dependency of cyclic voltammograms for $\mathbf{T^2}$ in Si-$\mathbf{A^2(FeL)_3FeT^2}$ at a scan rate of 1000 mVs^{-1} on the scan cycles, 1st cysle (blue solid line), 2nd cycle (red solid line) and 3rd cycle (green solid line). The 2nd cycle and the 3rd cycle are almost overlapped.
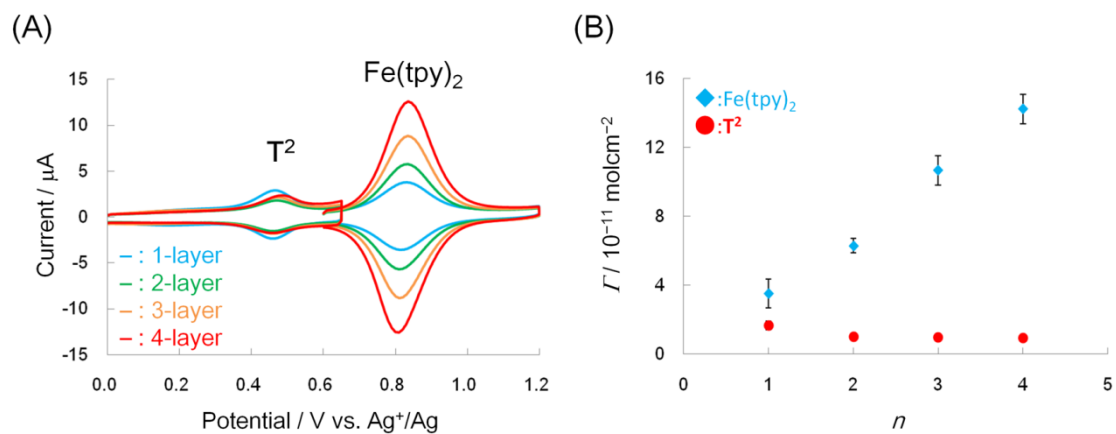
Figure 4-3-7. Cyclic voltammograms for Si-$\mathbf{A^2(FeL)_{n-1}FeT^2}$ at a scan rate of 500 mVs^{-1} (A), and the surface coverage values of Si-$\mathbf{A^2(FeL)_{n-1}FeT^2}$ (B).

4-4 Comparison of electron transport behavior

 The electron transport behavior from T^2 is drastically different from the case of T^1. The cyclic voltammograms of the terminal ligands in a 1-layered T^1-terminated wire (Si-A^2FeT^1) and a 3-layered T^2-terminated wire (Si-$A^2(FeL)_2FeT^2$) collected at scan rates of 25 mVs^{-1} and 1000 mV s^{-1}, are shown in Figure 4-4-1. Although T^1 shows a reversible redox couple at 25 mVs^{-1} potential sweep, large peak separation ($\Delta E_p = 0.13 \pm 0.01$ V) is observed at 1000 mVs^{-1}. On the other hand, the ΔE_p value of T^2 is only 0.021 ± 0.002 V at 1000 mVs^{-1} in spite of its longer distance from the electrode. This result means that the electron transport between T^2 and silicon is superior to that of T^1-terminated wire.
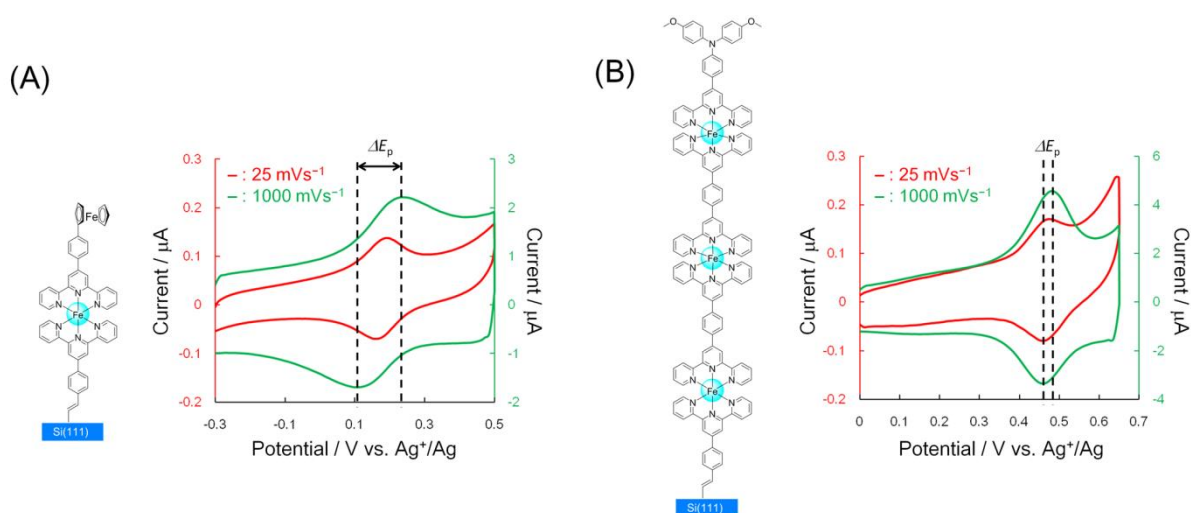
Figure 4-4-1. Cyclic voltammograms for Si-A^2FeT^1 (A) for Si-$A^2(FeL)_2FeT^2$ (B) at scan rates of 25 mVs^{-1} (red solid line) and 1000 mVs^{-1} (green solid line).

4-5 Electron transport mechanism of Fe(tpy)$_2$ wire on silicon electrode

The electron transport in Fe(tpy)$_2$ wire is composed of the three electron transport steps. The first one is the electron transfer between an electrode and the closest Fe(tpy)$_2$ unit from an electrode (ET1). The others are the electron transfer between the neighboring Fe complexes (ET2), and that between the Fe complex and a terminal ligand (ET3) (Figure 4-5-1). Among them, ET2 and ET3 should exhibit the same behavior with that observed in Fe(tpy)$_2$ wires on gold electrode because these structures are not changed. It is considered that ET1 is strongly affected by the change of electrode from gold to silicon. Therefore, the ET1 process is mainly focused in the following elucidation of electron transport mechanism.
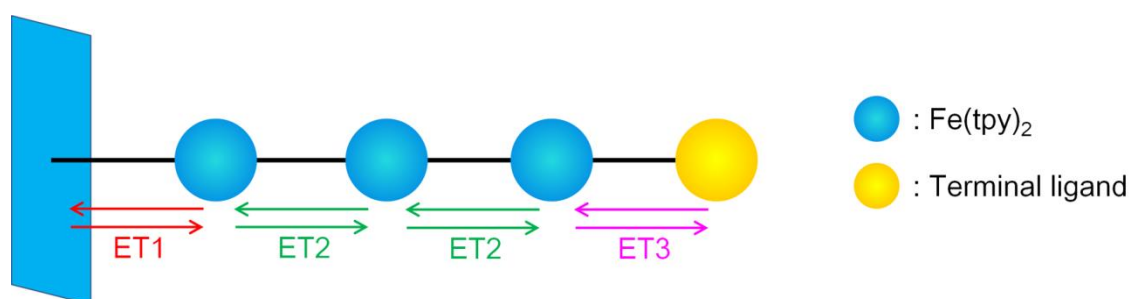
Figure 4-5-1. Electron transport model for Fe(tpy)$_2$ wire.

The observed different redox behavior of the terminal redox species at the top of Fe(tpy)$_2$ wire can be elucidated from the energy levels of the wire components and the band structure of silicon electrode. The energy levels of silicon conduction band edge and valence band edge are -4.05 eV and -5.17 eV from the vacuum level respectively [4b]. For the connection of the vacuum energy level and the redox potentials, the vacuum level of ferrocene HOMO level, -4.8 eV is useful [14]. The redox potentials of wire components, T^1, T^2 and Fe(tpy)$_2$ are 0.04 V, 0.33 V, and 0.68 V *vs.* ferrocenium/ferrocene respectively. Therefore, their approximate vacuum energy levels can be estimated as -4.8 eV, -5.1 eV and -5.5 eV, respectively. From these values, the energy diagram can be drawn (Figure 4-5-2).

Before the modified p-type silicon electrode contacts the electrolyte solution, the Fermi energy level (E_F) exists close to the valence band edge (Figure 4-5-3(A)). After contact with the electrolyte solution, the Fermi energy of silicon is aligned with the Fermi energy level of the solution (Figure 4-5-3(B)). In the case of metal electrode, the Fermi energy level can move freely. However, the Fermi energy of silicon cannot move like metal does because no levels in the forbidden band. Therefore, the energy level near the interface of silicon and the electrolyte solution is pinned, and the deformation of band structure occurs to make the same

Fermi energy with that of the solution. In the cyclic voltammetry measurement, the applied potential (E_{app}) is equal to the Fermi energy level of electrode. It means that the Fermi energy level of silicon is moved by the potential sweep and the degree of the band deformation state is also changed.

The estimated band structures of silicon when the CV measurements of $\mathbf{T^x}$ are performed as shown in Figure 3-5-4. At first, the case of the electron transport from $\mathbf{T^1}$ is considered. The HOMO level of $\mathbf{T^1}$ exists in the middle of the band gap and far from the valence band edge. In this situation, it is considered that the band structure is largely bended to realize the alignment of the Fermi energy with the HOMO level of $\mathbf{T^1}$. As a result, the large potential barrier is formed. In addition, the valence band and $Fe(tpy)_2$ units are occupied by electrons. These factors prevent the electron transport from $\mathbf{T^1}$, and give the large ΔE_p value indicating the slow electron transport. On the other hand, the redox potential of $\mathbf{T^2}$ is close to the valence band edge. This potential position is close to the initial state of silicon band structure before the contact with the electrolyte solution, and the much more relaxed deformation of the band than the case of $\mathbf{T_1}$. In addition, the applied potential is also close to the energy levels of $Fe(tpy)_2$ complexes, and a part of them can be oxidized and make the electron pathway. It is expected that they can contribute to produce the superior electron transport from $\mathbf{T^2}$.
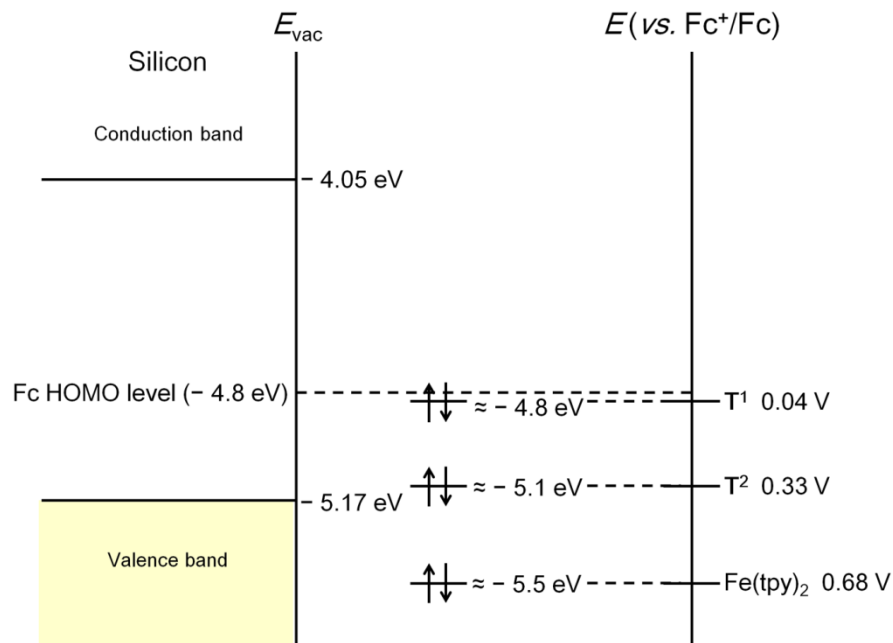
Figure 4-5-2. Vacuum level energies of the band edge of silicon and the wire components.
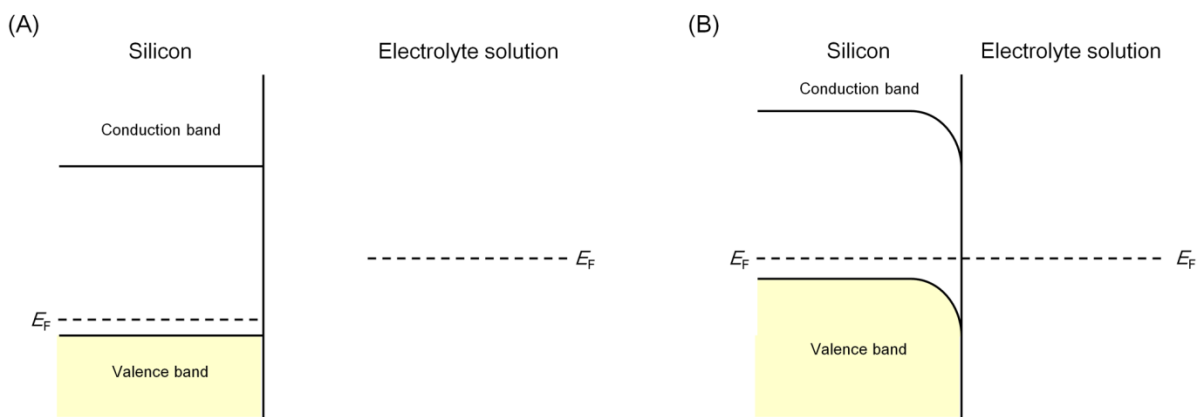
Figure 4-5-3. P-type silicon band structure before contact with an electrolyte solution (a) and after making connection (b).
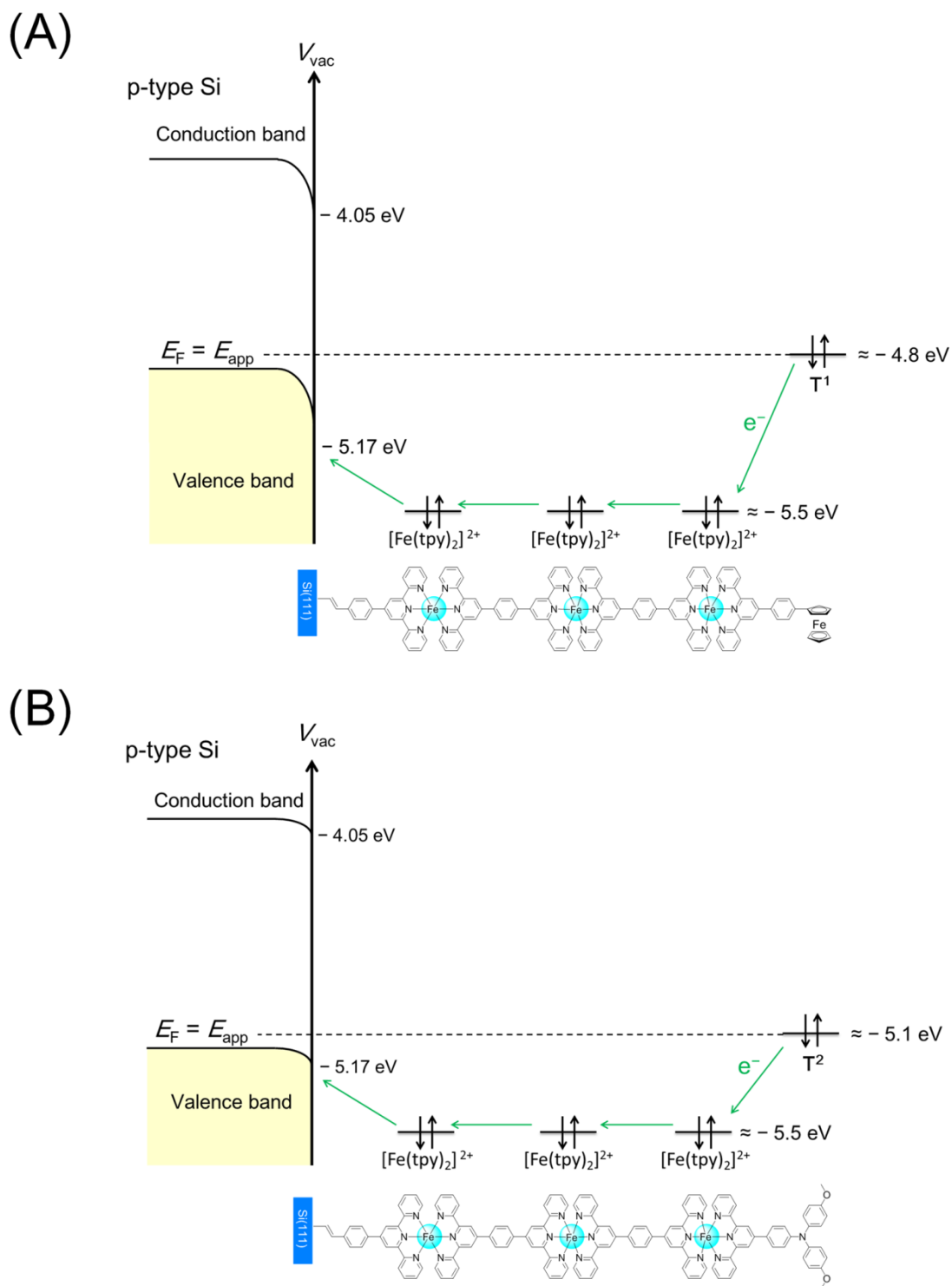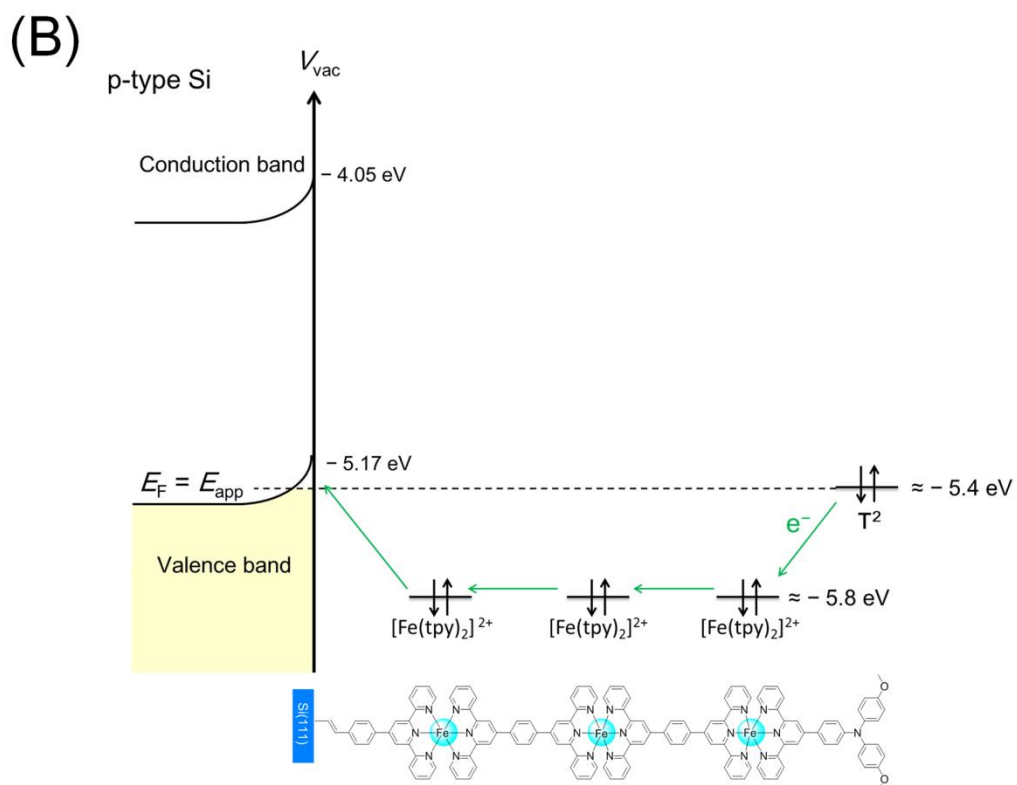
Figure 4-5-4. Energy diagrams for Si-$\mathbf{A^2(FeL)}_{n-1}\mathbf{FeT^1}$ (a) and Si-$\mathbf{A^2(FeL)}_{n-1}\mathbf{FeT^2}$ (b), and mechanisms of electron transport from $\mathbf{T^x}$.

In the above description, the vacuum level of ferrocene HOMO level is set at −4.8 eV. However, the various values have been reported such as −4.6 eV, −5.1 eV, −5.39 eV and −5.4 eV [4b, 15]. Here, the elucidation of the energy diagram is performed using −5.1 eV as a ferrocene HOMO level as an example. The vacuum energy levels of T^1, T^2 and $Fe(tpy)_2$ are calculated ats −5.1 eV, −5.4 eV and −5.8 eV, respectively (Figure 4-5-5). In this situation, the HOMO level of T^1 is very close to the valence band edge. Therefore, when the redox reaction of T^1 takes place, the silicon band structure is almost flat. However, the valence band is occupied by electrons and prevents the electron transport from T^1 via $Fe(tpy)_2$ units because the large energy barrier is formed between silicon and $Fe(tpy)_2$ complex. In the case of T^2, both of T^2 and $Fe(tpy)_2$ HOMO levels exist in the valence band. It means that the Fermi energy level also exists within the valence band. Therefore, the valence band is unoccupied state, and the easy injection of the electron transported from T^2 to electrode contributes the superior electron transport (Figure 4-5-6).
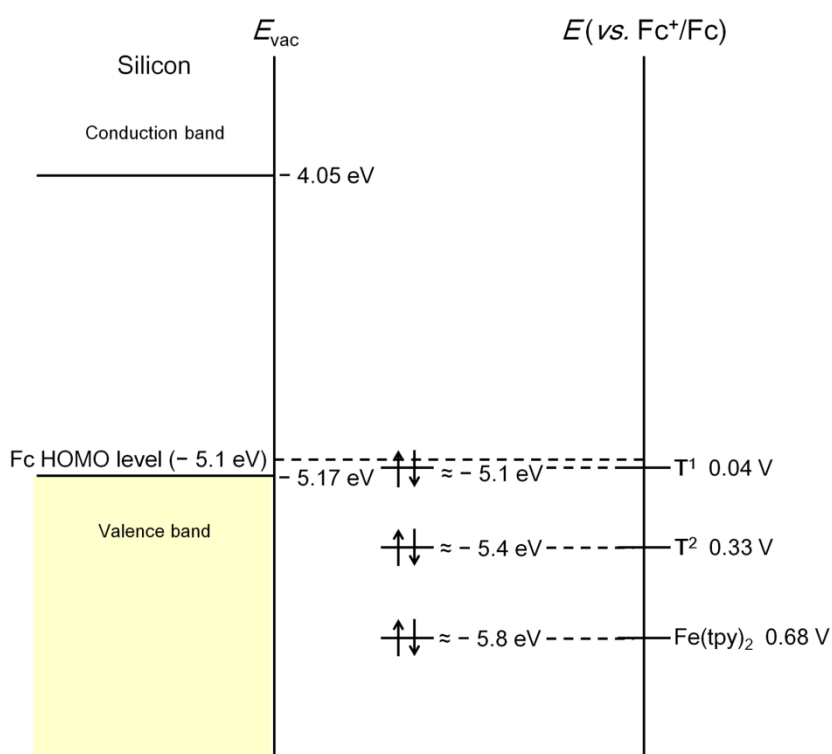
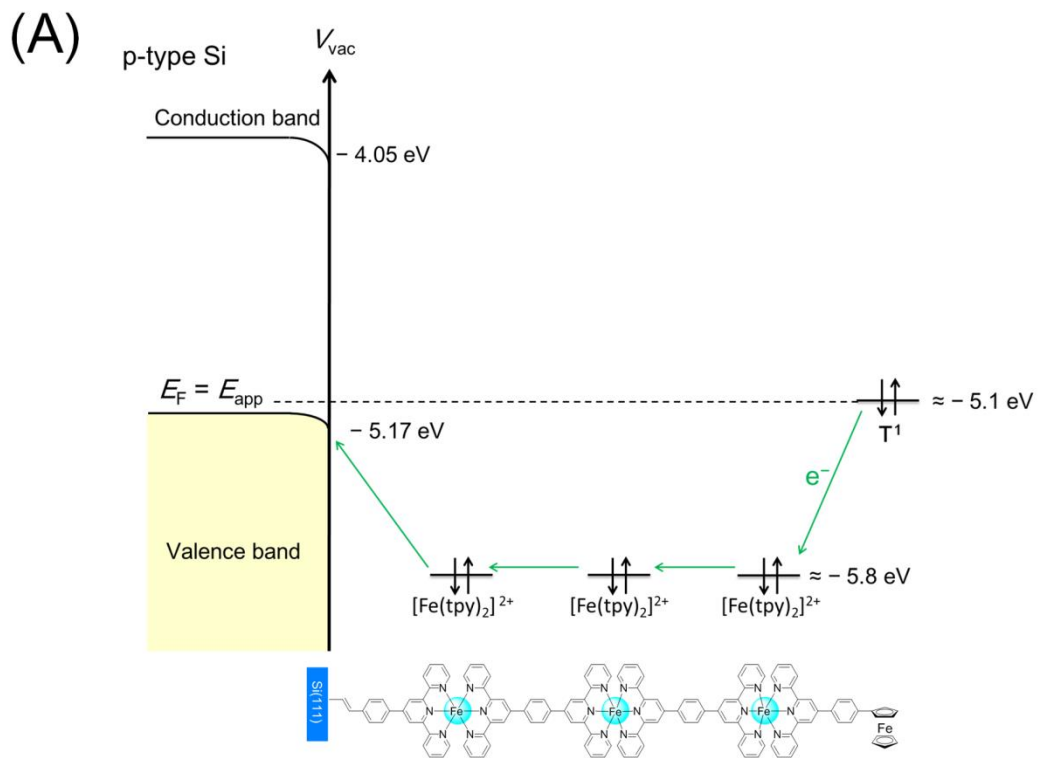**Figure 4-5-5.** Vacuum level energies of the band edge of silicon and the wire components.

Figure 4-5-6. Energy diagrams for Si-$\mathbf{A^2(FeL)_{n-1}FeT^1}$ (A) and Si-$\mathbf{A^2(FeL)_{n-1}FeT^2}$ (B), and electron transport mechanisms from $\mathbf{T^x}$.

4-6 Conclusion

In Chapter 4, the stepwise preparation of bis(terpyridine)iron complex wires including $\mathbf{T^1}$ or $\mathbf{T^2}$ at the termini, the qualitative comparison of electron transfer rate and the elucidation of electron transport mechanism were described.

The fabricated wires were evaluated by cyclic voltammetry, and the increase of surface coverage values for $Fe(tpy)_2$ complex and the constant value of $\mathbf{T^x}$ in accordance with the number of the layers revealed that the desired structures were obtained. The $\mathbf{T^1}$-terminated wires gave the reversible redox couple derived from $Fe(tpy)_2$ and the largely-separated redox peaks for $\mathbf{T^1}$ suggesting the slow electron transport. The reversible redox waves for $Fe(tpy)_2$ and $\mathbf{T^2}$ were observed in $\mathbf{T^2}$-terminated wires, indicating the rapid electron transport. This difference of electron transport behavior was explained based on the energy levels of silicon band structure, $\mathbf{T^x}$ and $Fe(tpy)_2$. In the case of $\mathbf{T^1}$-terminated wires, the slow electron transport occurs by the potential barrier due to the band edge deformation and the valence band and $Fe(tpy)_2$ units occupied by electrons. The reason of superior electron transport in $\mathbf{T^2}$-terminated wires is the small potential barrier and the electron pathway produced by the partially oxidized $Fe(tpy)_2$ units. In addition to the above reasons, the sequential hopping mechanism is also related to the characteristic electron transport behavior observed in $\mathbf{T^1}$-terminated wires.

4-7 References

1. Nishimori, Y.; Kanaizuka, K.; Murata, M.; Nishihara, H. *Chem. Asian J.* **2007**, *2*, 367-376.

2. Sakamoto, R.; Katagiri, S.; Maeda, H.; Nishimori, Y.; Miyashita, S.; Nishihara, H. *J. Am. Chem. Soc.* **2015**, *137*, 734-741.

3. a) Gowda, S.; Mathur, G.; Misra, V. *Appl. Phys. Lett.* **2007**, *90*, 142113. b) Haquier, F.; Ghilane, J.; Fabre, B.; Hapiot, P. *J. Am. Chem. Soc.* **2008**, *130*, 2748-2749. c) Lattimer, J. R. C.; Brunschwig, B. S.; Lewis, N. S.; Gray, H. B. *J. Phys. Chem. C* **2013**, *117*, 27012-27022.

4. a) Tajimi, N.; Sano, H.; Murase, K.; Lee, K.-H.; Sugimura, H. *Langmuir* **2007**, *23*, 3193-3198. b) Sano, H.; Zhao, M.; Kasahara, D.; Murase, K.; Ichii, T.; Sugimura, H. *J. Colloid Interf. Sci.* **2011**, *361*, 259-269. Yzambart, G.; Fabre, B.; Lorcy, D. *Langmuir* **2012**, *28*, 3453-3459. d) Roth, K. M.; Yasseri, A. A.; Liu, Z.; Dabke, R. B.; Malinovskii, V.; Scweikart, K.-H.; Yu, L.; Tiznado, H.; Zaera, F.; Lidsey, J. S.; Kuhr, W. G.; Bocian, D. F. *J. Am. Chem. Soc.* **2003**, *125*, 505-517.

5. a) Bookbinder, D. C.; Wrighton, M. S. *J. Am. Chem. Soc.* **1980**, *102*, 5125-5127. b) Bookbinder, D. C.; Bruce, J. A.; Dominey, R. N.; Lewis, N. S.; Wrighton, M. S. *Proc. Natl. Acad. Sci. USA* **1980**, *77*, 6280-6284.

6. a) Fabre, B.; Bassani, D. M.; Liang, C.-K.; Ray, D.; Hui, F.; Hapiot, P. *J. Phys. Chem. C* **2011**, *115*, 14786-14796. b) Feng, W.; Miller, B. *Langmuir*, **1999**, *15*, 3152-3156. c) Masuda, T.; Irie, M.; Uosaki, K. *Thin Solid Films*, **2009**, *518*, 591-595.

7. Claude, C. J.; Christophe, C.; Pierre, S. J. *New J. Chem.* **1992**, *16*, 361-367.

8. Winters, M. U.; Dahlstedt, E.; Blades, H. E.; Wilson, C. J.; Frampton, M. J.; Anderson, H. L.; Albinsson, B. *J. Am. Chem. Soc.* **2007**, *129*, 4291−4297.

9. He, Z.; Kan, C.-W.; Ho, C.-L.; Wong, W.-Y.; Chui, C.-H.; Tong, K.-L.; So, S.-K.; Lee, T.-H.; Leung, L. M.; Lin, Z. *Dyes Pigments* **2010**, *88*, 333-343.

10. Cârlescu, I.; Scutaru, A. M.; Apreutesei, D.; Alupei, V.; Scutaru, D. *Appl. Organometal. Chem.* **2007**, *21*, 661-669.

11. Katagiri, S.; Sakamoto, R.; Maeda, H.; Nishimori, Y.; Kurita, T.; Nishihara, H. *Chem. Eur. J.* **2013**, *19*, 5088-5096.

12. a) Gowda, S.; Mathur, G.; Misra, V. *Appl. Phys. Lett.* **2007**, *90*, 142113. b) Marrani, A. G.; Dalchiele, E. A.; Zanoni, R.; Decker, F.; Cattaruzza, F.; Bonifazi, D.; Prato, M. *Electrochemica Acta* **2008**, *53*, 3903-3909. c) Ciampi, S.; Eggers, P. K.; Saux, G. L.; James, M.; Harper, J. B.; Gooding, J. J. *Langmuir* **2009**, *25*, 2530-2539. d) Decker, F.; Cattaruzza, F.; Coluzza, C.; Flamini, A.; Marrani, A. G.; Zanoni, R.; Dalchiele, E. A. *J.*

Phys. Chem. B **2006**, *110*, 7374-7379.

13. a) Kanaizuka, K.; Murata, M.; Nishimori, Y.; Mori, I.; Nishio, K.; Masuda, H.; Nishihara, H. *Chem. Lett.* **2005**, *34*, 534-535. b) de Ruiter, G.; Lahav, M.; Keisar, H.; van der Boom, M. E. *Angew. Chem. Int. Ed.* **2013**, *52*, 704-709.

14. a) Pang, J.; Tao, Y.; Freiberg, S.; Yang, X. P.; D'Iorio, M.; Wang, S. *J. Mater. Chem.* **2002**, *12*, 206-212. b) Pommerehne, J.; Vestweber, H.; Guess, W.; Mahrt, R. F.; Bässler, H.; Porsch, M.; Daub, J. *Adv. Mater.* **1995**, *7*, 551-554. c) Lee, S. H.; Jang, B.-B.; Kafafi, Z. H. *J. Am. Chem. Soc.* **2005**, *127*, 9071-9078.

15. Cardona, C. M.; Li, W.; Kaifer, A. E.; Stockdale, D.; Bazan, G. C. *Adv. Mater.* **2011**, *23*, 2367-2371.

Chapter 5

Concluding remarks

5 Concluding remarks

  In this thesis, the sequential construction of bis(terpyridine)iron (Fe(tpy)$_2$) complex wire on hydrogen-terminated silicon(111) surface and their electrochemical property were described.

  In Chapter 2, the Fe(tpy)$_2$ complexes linked via the four types of anchor ligands (Si-**A^{x}FeL**, $x = 1 - 4$) were prepared on p-type hydrogen-terminated silicon electrodes by the stepwise coordination reaction. The obtained results from cyclic voltammetry, X-ray photoelectron spectroscopy and atomic force microscope confirmed the construction of Fe(tpy)$_2$ on silicon surface. The quantitative evaluation of the electron transfer rate constant (k_{ET}) between an electrode and a Fe(tpy)$_2$ complex was achieved by potential step chronoamperometry (PSCA). The estimated k_{ET} values exhibited that the anchor ligands including a phenylene bridge in their structure (Si-**A^{2}FeL** and Si-**A^{4}FeL**) have the superior electron transfer ability in spite of their longer distance between the iron center and silicon electrode. This phenomenon was explained by the small energy difference between HOMO level and HOMO−3 level by the DFT calculation for the simplified structures.

  In Chapter 3, the Fe(tpy)$_2$ complex (Si-**A^{5}FeL**) was prepared on silicon substrate via the direct Si-arene bond formed by the Pd-catalyzed coupling reaction. The construction of Fe(tpy)$_2$ complex was confirmed by the reversible redox wave derived from [Fe(tpy)$_2$]$^{3+/2+}$ in the cyclic voltammogram and the proportional dependency of peak current on scan rate. The k_{ET} values for Si-**A^{5}FeL** obtained by PSCA was greater than that of Si-**A^{1}FeL** which has the Fe(tpy)$_2$ unit linked with the electrode via vinylene bridge. This promotion of electron transfer came from the energy rise of HOMO−3 level in Si-**A^{5}Fetpy** due to the expansion of π-conjugation making the small energy difference between HOMO and HOMO−3 levels.

  In Chapter 4, the redox active terminal ligands were introduced at the top of Fe(tpy)$_2$ wires on silicon electrode. From the redox behavior of the terminal redox site, the electron transport behavior of Fe(tpy)$_2$ wires were elucidated. The sequential elongation of the wires were confirmed by the increase of coverage values of Fe(tpy)$_2$ estimated from the integration of the redox wave with the number of coordination cycles. The large separation of oxidation peak and reduction peak of **T^1** in Si-**A^2(FeL)$_{n-1}$FeT^1** suggested that the slow electron transport between **T^1** and electrode. The **T^2** in Si-**A^2(FeL)$_{n-1}$FeT^2** showed the reversible redox wave with the small peak separation even in the elongated wires and indicated the superior electron transport. This difference of electron transport behavior was elucidated from the energy levels of silicon band structure and HOMO levels for Fe(tpy)$_2$ and the terminal ligands.

These results show that the electron transport behavior of molecular systems on semiconducting electrode are affected by their molecular structure, the junction structure, the energy levels of wire components and the electronic state of electrode. These insights will show the way to design molecular wires on semiconductor and contribute to the achievement of molecular electric devices transporting electron effectively.

List of publications

【Publication related to the thesis】
1. "Surface Junction Effects on Interfacial Electron Transfer Between Bis(terpyridine)iron(II) and Hydrogen-Terminated Silicon(111) Electrode"
Hiroaki Maeda, Ryota Sakamoto, Hiroshi Nishihara, *Chem. Eur. J.* **2014**, *20*, 2761-2764.

【Publications not related to the thesis】
1. "Electron Transport Dynamics in Molecular Circuits: Redox-terminated Branched Oligomer Wires on Au(111)"
Ryota Sakamoto, Shunsuke Katagiri, Hiroaki Maeda, Yoshihiko Nishimori, Seiji Miyashita, Hiroshi Nishihara, *J. Am. Chem. Soc.* **2015**, *137*, 734-741.
2. "Equatorenes: Synthesis and Properties of Chiral Naphthalene, Phenanthrene, Chrysene, and Pyrene Possessing Bis(1-adamantyl) Groups at the Peri-Position"
Koji Yamamoto, Naohiro Oyamada, Sheng Xia, Yuta Kobayashi, Masahiko Yamaguchi, Hiroaki Maeda, Hiroshi Nishihara, Tadafumi Uchimaru, Eunsang Kwon, *J. Am. Chem. Soc.* **2013**, *135*, 16526-16532.
3. "A bis(terpyridine)iron network polymer on carbon for a potential energy storage material"
Kuo-Hui Wu, Hiroaki Maeda, Tetsuya Kambe, Ken Hoshiko, Eunice Jia Han Phua, Ryota Sakamoto, Hiroshi Nishihara, *Dalton Trans.* **2013**, *42*, 15877-15880. (Selected as the cover)
4. "Orthogonal bis(terpyridine)-Fe(II) metal complex wires on a tripod scaffold: Rapid electron transport"
Ryota Sakamoto, Yuuki Ohirabaru, Ryota Matsuoka, Hiroaki Maeda, Shunsuke Katagiri, Hiroshi Nishihara, *Chem. Commun.* **2013**, *49*, 7108-7110.
5. "Metal Complex Oligomer and Polymer Wires on Electrodes: Tactical Constructions and Versatile Functionalities"
Hiroaki Maeda, Ryota Sakamoto, Hiroshi Nishihara, *Polymer* **2013**, *54*, 4383-4403.
6. "Triarylamine-Conjugated Bis(terpyridine)-Fe(II) Complex Wires: Rapid and Long-Range Electron Transport Ability"
Ryota Sakamoto, Shunsuke Katagiri, Hiroaki Maeda, and Hiroshi Nishihara, *Chem. Lett.* **2013**, *42*, 553-555.
7. "Terminal Redox Site Effect on the Long-Range Electron Conduction of $Fe(tpy)_2$ Oligomer Wires on Gold Electrode"
Shunsuke Katagiri, Ryota Sakamoto, Hiroaki Maeda, Yoshihiko Nishimori, Tomochika Kurita, Hiroshi Nishihara, *Chem. Eur. J.* **2013**, *19*, 5088-5096.

8. "Bis(terpyridine) metal complex wires: Excellent long-range electron transfer ability and controllable intrawire redox conduction on silicon electrode"

Ryota Sakamoto, Shunsuke Katagiri, Hiroaki Maeda, Hiroshi Nishihara, *Coord. Chem. Rev.* **2013**, *257*, 1493-1506.

9. "A New Method to Generate Arene-Terminated Si(111) & Ge(111) Surfaces via a Palladium-Catalyzed Arylation Reaction"

Yoshinori Yamanoi, Junya Sendo, Tetsuhiro Kobayashi, Hiroaki Maeda, Yusuke Yabusaki, Mariko Miyachi, Ryota Sakamoto, Hiroshi Nishihara, *J. Am. Chem. Soc.* **2012**, *134*, 20433-20439.

10. "Synthesis and Electron Transfer Properties of Metal Complex Oligomer Wires with an Inherent Potential Gradient on Gold Electrode"

Yoshihiko Nishimori, Hiroaki Maeda, Shunsuke Katagiri, Junya Sendo, Mariko Miyachi, Ryota Sakamoto, Yoshinori Yamanoi, Hiroshi Nishihara, *Macromol. Symp.*, **2012**, *317-318*, 276-285.

11. 「錯体化学選書９　金属錯体の電子移動と電気化学」三共出版　2013 年
編著：西原　寛、市村彰男、田中晃二　共著：伊藤　翼、菊池　貴、小林克彰、坂本良太、佐々木陽一、谷口　功、西山勝彦、芳賀正明、濱口智彦、福住俊一、前田啓明、Brian K. Breedlove、山口　正

6 Acknowledgements